UNIVERSITÉ DU QUÉBEC

MÉMOIRE

PRÉSENTÉ À

L'UNIVERSITÉ DU QUÉBEC À CHICOUTIMI

COMME EXIGENCE PARTIELLE

DE LA MAÎTRISE EN RESSOURCES ET SYSTÈMES

PAR

ANDRÁS HAIDEKKER

RADIATION MODELLING IN COMPLEX THREE DIMENSIONAL ENCLOSURES

August 1991

Bibliothèque
Paul-Émile-Boulet

UQAC
Université du Québec
à Chicoutimi

Mise en garde/Advice

Afin de rendre accessible au plus grand nombre le résultat des travaux de recherche menés par ses étudiants gradués et dans l'esprit des règles qui régissent le dépôt et la diffusion des mémoires et thèses produits dans cette Institution, **l'Université du Québec à Chicoutimi (UQAC)** est fière de rendre accessible une version complète et gratuite de cette œuvre.

Motivated by a desire to make the results of its graduate students' research accessible to all, and in accordance with the rules governing the acceptation and diffusion of dissertations and theses in this Institution, the **Université du Québec à Chicoutimi (UQAC)** is proud to make a complete version of this work available at no cost to the reader.

L'auteur conserve néanmoins la propriété du droit d'auteur qui protège ce mémoire ou cette thèse. Ni le mémoire ou la thèse ni des extraits substantiels de ceux-ci ne peuvent être imprimés ou autrement reproduits sans son autorisation.

The author retains ownership of the copyright of this dissertation or thesis. Neither the dissertation or thesis, nor substantial extracts from it, may be printed or otherwise reproduced without the author's permission.

To Andi, Isti and Balázs with love

Résumé

Les méthodes de zones, des plans imaginaires et les transferts discrets ont été adaptées à la modélisation du transfert de chaleur radiatif dans les enceintes complexes en trois dimensions. Puisque l'accent a été mis sur les aspects géométriques du rayonnement, le millieu gazeux a été considéré gris pour ne pas alourdir indûment la présentation. Des techniques de dépistage de rayons ont été adaptées spécifiquement à chacune des méthodes, ouvrant ainsi la voie à l'utilisation des coordonnées cylindriques et curvilignes. Des comparaisons sont données pour évaluer la justesse et le temps de calcul des méthodes des plans imaginaires et des transferts discrets par rapport à la méthode de zones. Ces comparaisons ont été réalisées pour des enceintes rectangulaire et cylindrique en faisant varier l'émissivité de surface et le coefficient d'absorption du gaz. Quatre cas complexes simulant de près des problèmes industriels ont été traités par les differentes méthodes, de façon à mettre en lumière les possibilités des techniques utilisées.

Abstract

The zone, the imaginary planes and the discrete transfer methods have been adapted for modelling thermal radiation in complex 3D enclosures. Since emphasis is laid on the geometrical aspects of radiation, for the sake of simplicity, radiation was modelled in gray systems. All three methods have been fitted with ray tracing techniques which have been tailored to the specific requirements of the methods, enabling the treatment of cylindrical and curvilinear systems as well. Comparisons are reported to evaluate accuracy and computational performance of the imaginary planes and the discrete transfer methods relative to the zone method in a rectangular and in a cylindrical enclosure at variable surface emissivities and gas absorption coefficients. Four difficult 3D cases close to industrial problems have been worked out by the different methods to show the geometrical capabilities of the different models.

Acknowledgments

I wish to acknowledge gratefully the contribution of my thesis supervisor Prof. André Charette for his support and encouragement throughout this work.

I am also greatly indepted to Yasar Kocaefe, my co-supervisor, for our fruitful discussions about the zone method.

I wish to thank all the members of the research group GRIPS (Groupe de Recherche en Ingénierie des Procédés et Systèmes) for providing an inspiring working environment, and especially to André Arsenault, Steve Brisson, Réjean Ouellet and Yong Ke Wu for their precious assistance in some parts of my thesis.

My recognition goes also to Prof. László Kiss for his pertinent suggestions.

This work would not have been possible without the financial contributions of the Université du Québec à Chicoutimi and the PAIR program.

Finally I deeply express my gratitude for the support and understanding of my wife and my children from the beginning to the end of this work.

Contents

List of Figures

List of Tables

Nomenclature

A	surface area	m^2
a, b, c	lines used to determine the emission point from a volume zone	
A, B, C, D	coefficients of the equation of a plane	
B_{kj}	term containing reception factors	
BM	matrix containing the coefficients of the imaginary fluxes (equation 2.20)	
CM	vector formed from the right hand side of eq. (2.20)	
D_j	term containing emissive powers and net heat flows	
$\mathbf{d}$	directional vector of the path of a ray from the emitting surface	
$\mathbf{d}^*$	directional vector of the path of a ray from the *x, y* plane, or in the local coordinate system for the cylindrical case	
dim	dimension of the set of equations (2.20)	
E	black emissive power σT^4	kW/m^2
f_{jk}	reception factor between surface *j* and surface *k*	
f_{ig}	reception factor between surface *i* and the gas volume *g*	
$\overline{gs_k}$	direct interchange area between the gas volume and an enclosing surface area *k*	m^2
$\overline{G_iS_j}$	total interchange area between gas zone *i* and surface zone *j*	m^2
$\overline{G_iG_j}$	total interchange area between gas zone *i* and gas zone *j*	m^2
ΔH_{gas}	sensible enthalpy change through a gas volume	kW

I	intensity of a pencil of ray	kW/m^2.sr
I_b	black-body intensity	kW/m^2.sr
I_n	intensity of the n-th zone	kW/m^2.sr
I_o	intensity leaving a surface zone	kW/m^2.sr
K	gray gas absorption coefficient	1/m
KB	optical thickness	
L	length of travel of a bundle	m
m	tangent of a line	
$\mathbf{M}_\gamma$	matrix of rotation relative to γ	
$\mathbf{M}_\delta$	matrix of rotation relative to δ	
$\mathbf{n}$	normal vector of a surface zone	
nz	number of surface zones of an enclosure	
nv	number of volume zones of an enclosure	
P	point in 3D cartesian space	
q_k	net heat flux on the real surface k	kW/m^2
q_{k_o}	heat flux leaving a surface zone k	kW/m^2
q_{k_i}	heat flux incident on the surface zone k	kW/m^2
q_i	heat flux incident on a surface	kW/m^2
q_{net}	net heat flux on a surface	kW/m^2
q_o	heat flux leaving a surface	kW/m^2
$\mathbf{Q}$	vector containing the net radiative heat rates through the imaginary planes	kW
Q_k	net radiative heat rate through an imaginary plane	kW
$Q_{i,net}$	net heat rate transferred to a zone	kW
$Q_{i \rightleftharpoons j}$	net radiative interchange between a pair of zones	kW
Q_{rad}	radiative heat rate transferred to a zone	kW
Q_{conv}	convective heat rate transferred to a zone	kW
Q_{cond}	conduction heat rate transferred to a zone	kW

Q_{comb}	heating rate of combustion	kW
R	random number used in the Monte Carlo process	
$\mathbf{r}$	vector pointing from the origin to a point in 3D cartesian space	
r, s, t	parameters of the equation of a line crossing two points in 3D cartesian space	
r, ϕ, z	coordinates in the cylindrical coordinate system	
s_i	distance traveled by a ray in a zone	m
S	radiative source term	kW
$\overline{S_iS_j}$	total interchange area between surface zone *i* and surface zone *j*	m^2
$\overline{s_is_j}$	direct interchange area between surface zone *i* and surface zone *j*	m^2
$\overline{S_iG_j}$	total interchange area between surface zone *i* and gas zone *j*	m^2
t	parameter of the line equation describing the path of a ray	
T_g	gas temperature	K
T_s	surface temperature	K
V	volume of a gas zone	m^3
x, y, z	coordinates in 3D cartesian space	
x_e, y_e, z_e	coordinates of the emission point (P_e) of a ray in the cartesian space	
x_i, y_i, z_i	coordinates of the intersection point (P_i) of the path of a ray with a surface	

Greek symbols

β	cone angle of emission of a bundle in the Monte Carlo process	
γ	angle of rotation of surface normal vector around the z axis	
δ	angle of rotation of surface normal vector around the y axis , or Kronecker delta	
ϵ	emissivity	
θ	circumferential angle of emission of a bundle in the Monte Carlo process	
$\xi,\ \eta,\ \zeta$	curvilinear coordinates	
σ	Stefan-Boltzmann constant	$kW/m^2.K^4$
τ	transmissivity	
ϕ	coordinate in the cylindrical coordinate system	
φ_{ij}	total reception factor	
$d\Omega$	differential solid angle	sr

Subscripts

$a,\ b$	identification of points
g	gas zone
i	incident
$i,\ j,\ k,\ n$	identification of a gas or of a surface zone
o	leaving
s	surface zone
$x,\ y,\ z$	according to directions x, y and z

I, II, III, IV, V	numbering used for surface area or volume calculation
$1, 2, ..., 6$	identification of the surfaces enclosing a volume zone
$1, 2, ..., 8$	identification of corner points (vertices) of volumes in 3D cartesian space

Superscripts

C, N, S, E, W, NE, HE	position relative to a zone : central, north, south, east, west, north-east, high-east

Abreviations

ARD	average relative difference between the surface heat flux obtained with the IPM or DT method and that obtained with the zone method
DIA	direct interchange area
DT	discrete transfer method
$DT36$, $DT100$...	discrete transfer method with different number of hemispherical divisions
IPM	imaginary planes method
MRD	maximum relative difference between the surface heat flux obtained with the IPM or DT method and that obtained with the zone method
TIA	total interchange area
VRD	average relative difference between the radiative volumetric source term obtained with the IPM or DT method and that obtained with the zone method

1

Introduction

Nowadays the utilization of natural resources and the environment protection are emerging as critical issues. The industrial furnaces and combustion chambers, being main fuel consumers and also pollution sources, are strongly linked with these questions. There is a constant need to lower the fuel consumption and pollutant emissions. Slight increase in furnace efficiency can result in large savings in operating costs considering today's fuel prices. A better understanding of the physical phenomena in the combustion chambers and industrial boilers helps to improve their performance, which has positive effects in both economic and environmental points of view.

Mathematical modelling of furnaces and industrial boilers is a powerful tool which can be used to design new efficient installations, or to improve and optimize the operation of the existing ones. A complete furnace simulation includes the solution of the momentum, heat and mass transfer equations. In most cases radiation is the predominant heat transfer mechanism.

In the past thirty years several numerical methods have been worked out to model the radiation phenomenon. Among the most important and well known methods are the *zone* method (Hottel et al. 1967), the Monte Carlo method (Siegel and Howell 1972), the

six-flux method (de Marco and Lockwood 1975), the *discrete ordinates* method (Fiveland 1987) and the *discrete transfer* method (Shah 1979). These methods have been improved constantly and adapted to increasingly difficult problems, including real gas, particle scattering and special surface behavior.

Some of the latest contributions to radiation modelling are given below. Charette et al. (1990) worked out a modified zone method called the *imaginary planes method.* The method has proven to be attractive and accurate since it retains the essential features of the zone method while reducing the computing time significantly. Raithby and Chui (1990) report a new finite volume method that can be implemented on non-orthogonal grids used for fluid flow problems. Bhattacharjee and Grosshandler (1990) propose a model based on a two-flux scheme for rectangular and cylindrical enclosures. The method is applied in a two-dimensional geometry for gray and real gases. Kumar et al. (1990) report their work on the differential-discrete-ordinate method. They compare several quadrature schemes to reduce the radiative transfer equation to a set of ordinary differential equations which can be readily solved. Kobiyama (1990) describes a modified Monte Carlo method which is aimed at reducing the computing time.

1.1 Scope of the present work

Radiation heat transfer is strongly dependent on the geometrical configuration of the enclosure. Most of the methods are worked out for 2D or for simple 3D cases like rectangular parallelepipeds and cylinders. However, radiation modelling is often desired in case of complex and irregular geometrical configurations.

In this work, three methods have been adapted for modelling radiation in 3D enclosures. These are the *zone*, the *imaginary planes* and the *discrete transfer* methods.

Details of the methods will be given in chapter 2. All three methods can handle problems in 3D rectangular, cylindrical and irregularly shaped enclosures. In each method the radiation space is subdivided into finite volumes, or zones, with the help of a grid. For rectangular parallelepipeds the grid is cartesian, for cylinders it is cylindrical and for enclosures with irregular geometries the space should be subdivided into hexahedral zones with a curvilinear grid. Also any number of zones can be blocked within the domain for a better representation of the geometry if it becomes necessary.

Since emphasis is laid on the geometrical aspects of radiation, for the sake of simplicity, radiation is modelled in gray systems i.e. walls are considered as gray lambertian surfaces where the cosine law is assumed and enclosures are filled with gray gases. However, the gray system restriction can be removed easily with already existing procedures.

All three methods have been fitted with ray tracing techniques which have been tailored to the specific requirements of the methods. The imaginary planes method requires ray tracing only within the individual cells while zone and discrete transfer methods require ray tracing through the entire radiation space. Ray tracing is generally considered to be computationally expensive, but the rapidly increasing computational power of engineering workstations justifies their extended use in radiation models. Two separate codes have been worked out for ray tracing, one for cylindrical and one for irregular systems with hexahedral volume zones. The rectangular system can be considered as a special case of the latter, and it uses the same algorithm.

The zone method is regarded as one of the most accurate radiation modelling method. In the case of complex 3D systems for which exact solutions are not available,

the zone method can serve as the "accurate solution" for radiation problems. This method was used as a reference throughout the present work. Comparisons were made to evaluate the accuracy and the computational performance of the imaginary planes method (IPM) and the discrete transfer method (DT). Also, some difficult 3D radiation problems were solved by some of the methods. These complex 3D geometries all originate from practical combustion systems.

2

Radiation modelling methods

The present discussion concerns only gray systems without any reference to selective gas absorption or scattering effects. This follows from the objective of this study which is to compare the performance of the three methods and to apply them to complex geometrical configurations without further complications.

In the following, a summary of the *zone*, the *imaginary planes* and the *discrete transfer* methods is given in order to have a clear reference for further developments.

2.1 The zone method

The radiation space and the boundaries are discretized by a grid into a number of finite volumes and finite surfaces, which are called volume and surface zones, respectively. Temperatures and radiative properties are assumed to be uniform in the finite volumes and over the finite surfaces.

If the temperature distribution is available, a radiative energy balance can be written for each zone. The radiative balance includes the radiative exchange between a given zone and every other zone of the system, with the help of the *total-interchange* areas.

The net radiative interchange using the total interchange areas for a pair of surface zones of the enclosure is expressed as:

$$Q_{i \rightleftharpoons j} = \overline{S_i S_j}(E_{s,i} - E_{s,j}) \tag{2.1}$$

Analogous expressions are written for an exchange between a gas and a surface zone:

$$Q_{i \rightleftharpoons j} = \overline{G_i S_j}(E_{g,i} - E_{s,j}) \tag{2.2}$$

and between the two gas zones:

$$Q_{i \rightleftharpoons j} = \overline{G_i G_j}(E_{g,i} - E_{g,j}) \tag{2.3}$$

In the above equations, Q is the radiative heat transfer [W], $\overline{S_i S_j}$, $\overline{G_i S_j}$, $\overline{G_i G_j}$ are the total exchange areas [m^2] and E is the emissive power [W/m^2].

Considering the interactions between a surface zone i and all the other zones j of the enclosure, the net radiative flow on the i-th surface zone can be expressed as:

$$Q_{i,net} = \sum_j \overline{S_j S_i}\,(E_{s,j} - E_{s,i}) + \sum_j \overline{G_j S_i}\,(E_{g,j} - E_{s,i}) \tag{2.4}$$

The energy balance can be further simplified by isolating $E_{s,i}$ which gives:

$$\begin{aligned} Q_{i,net} &= \sum_j \overline{S_j S_i}\,E_{s,j} + \sum_j \overline{G_j S_i}\,E_{g,j} - E_{s,i}\left(\sum_j \overline{S_j S_i} + \sum_j \overline{G_j S_i}\right) \\ &= \sum_j \overline{S_j S_i}\,E_{s,j} + \sum_j \overline{G_j S_i}\,E_{g,j} - \epsilon_i A_i E_{s,i} \end{aligned} \tag{2.5}$$

The radiative balance for a gas zone i considering all the interactions with the other zones of the enclosure, including itself is given by:

$$\begin{aligned} Q_{i,net} &= \sum_j \overline{S_j G_i}\,E_{s,j} + \sum_j \overline{G_j G_i}\,E_{g,j} - E_{g,i}\left(\sum_j \overline{S_j G_i} + \sum_j \overline{G_j G_i}\right) \\ &= \sum_j \overline{S_j G_i}\,E_{s,j} + \sum_j \overline{G_j G_i}\,E_{g,j} - 4K_i V_i E_{g,i} \end{aligned} \tag{2.6}$$

Equation (2.6) is the mathematical expression for the so-called volumetric radiative source term for gas zone *i*.

The above equations yield directly the radiative heat flows if the temperatures of all the zones (surface and gas) are known. In the absence of a known temperature distribution, complete or partial, an overall heat balance is written for each zone of unknown temperature. This results in a set of non-linear algebraic equations which has to be solved iteratively. For this purpose, the flow and combustion patterns as well as the convection and conduction coefficients at the zones must be available. The overall energy conservation equation can be written for a surface zone as

$$Q_{rad} + Q_{conv} + Q_{cond} = 0 \tag{2.7}$$

and for a gas zone

$$Q_{rad} + Q_{conv} + Q_{cond} + Q_{comb} + \Delta H_{gas} = 0 \tag{2.8}$$

The method can easily be extended to enable the treatment of real gas cases by the use of weighting factors associated to a number of gray gases according to Hottel (1967).

Obviously it is the calculation of the total interchange areas which represents the greatest challenge in the zone method. The geometrical difficulties to overcome are all included in these terms. Closed formulas are given only for a very limited number of cases. The Monte-Carlo technique is well adapted for such calculations, and it can be applied to the most complex radiation problems. A brief description of the Monte-Carlo technique and a detailed discussion of its use in different geometries will be given in the following chapter.

The zone method is a precise radiation calculation technique but its high computation time and memory requirements makes it rather inefficient in many cases, especially those where a complete simulation (coupling with energy and motion equations) is required or where a transient situation is studied.

2.2 Imaginary planes method

The imaginary planes method (IPM) was developed in 2D by Erchiqui (1987) based on the paper of Ström (1980). The method was further developed by Larouche (1988) for 3D rectangular enclosures.

The imaginary planes method is essentially a simplified zone method. The radiation space is divided into zones in the same manner. The volume zones are filled with gas (gray in the present study) of uniform temperature and absorption coefficient, and the walls of the enclosure are considered as diffuse gray of uniform emissivity. The volume zones are bounded by real surfaces along the walls of the enclosure and by "imaginary planes" (surfaces) in the radiation field. Each volume zone has a direct view only of its boundaries, i.e. direct radiation exchange takes place only inside the volume zones. The adjacent volume zones are linked through radiative fluxes crossing the imaginary planes.

2.2.1 Radiation principles inside a single zone

A rectangular enclosure divided into zones is shown on Figure 2.1.

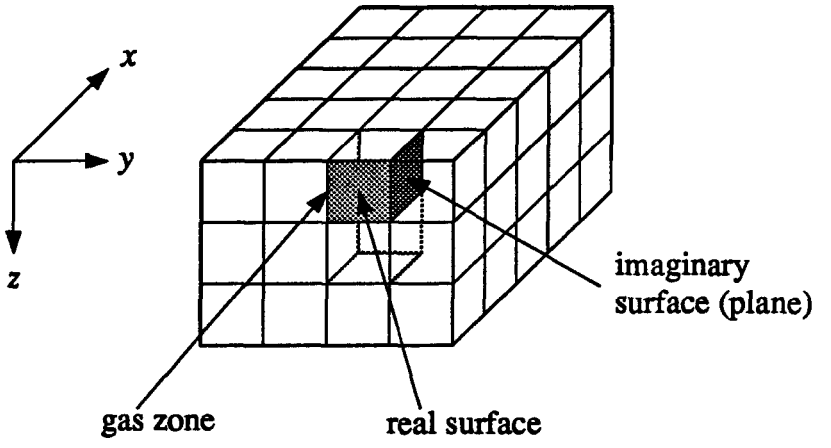

Figure 2.1 Division of an enclosure into zones

The net radiation to real surface k can be written as:

$$A_k q_k = A_k(q_{k_o} - q_{k_i}) \tag{2.9}$$

with the radiation leaving the surface:

$$A_k q_{k_o} = A_k(\epsilon_k E_k + (1 - \epsilon_k) q_{k_i}) \tag{2.10}$$

and the irradiation due to the radiation received from the other surfaces of the zone and from the gas:

$$A_k q_{k_i} = \sum_{j=1}^{6} A_j f_{jk} q_{j_o} + E_g \overline{gs_k} \tag{2.11}$$

The meaning and the calculation procedure of the reception factor f_{jk}, and the gas-surface direct interchange area $\overline{gs_k}$ will be discussed in detail in the following chapter. Combining (2.9), (2.10) and (2.11) results in an equation in which the incident flux is absent:

$$q_{k_o} - (1 - \epsilon_k) \sum_{j=1}^{6} f_{kj} q_{j_o} = \epsilon_k E_k + (1 - \epsilon_k) \frac{E_g \overline{gs_k}}{A_k} \tag{2.12}$$

On the other hand a heat balance performed on an imaginary plane gives :

$$Q_k = (q_{k_o} - q_{k_i})A_k \tag{2.13}$$

Using (2.11) and (2.13) the following equation can be obtained for the imaginary plane:

$$q_{k_o} - \sum_{j=1}^{6} f_{kj} q_{j_o} = \frac{Q_k}{A_k} + \frac{E_g \overline{gs_k}}{A_k} \tag{2.14}$$

The similarity of equations (2.12) and (2.14) can be exploited to obtain a relation which is valid for both cases

$$\sum_{j=1}^{6} b_{kj} q_{j_0} = D_k \qquad k = 1...6$$

where

$$b_{kj} = \begin{cases} \delta_{kj} - (1-\epsilon_k) f_{kj} & real\ surface \\ \delta_{kj} - f_{kj} & imaginary\ surface \end{cases} \tag{2.15}$$

$$D_k = \begin{cases} \epsilon_k E_k + (1-\epsilon_k) E_g \frac{\overline{gs_k}}{A_k} & real\ surface \\ \frac{Q_k}{A_k} + E_g \frac{\overline{gs_k}}{A_k} & imaginary\ surface \end{cases}$$

where δ is the Kronecker delta. The set of equations can be arranged in a matrix form. To find q_{j_o} the system should be inverted:

$$q_{k_o} = \sum_{j=1}^{6} B_{kj} D_j \qquad k = 1...6 \tag{2.16}$$

where $B = b^{-1}$. As it can be seen from (2.15), D_k contains the imaginary flow term Q_k. Other relations have to be introduced in order to be able to solve for the net heat flows on the real surfaces. This is explained in the next section.

2.2.2 Linking procedure between the zones by the imaginary fluxes

The above equations apply within one single zone. From now on, this zone is marked by a superscript *C* (for "central") and the surrounding zones are referred to, according to Figure 2.2, by *E, W, N, S, H, L* (for "east, west, north, south, high, low"

respectively). The linking procedure between the adjacent zones is demonstrated also on Figure 2.2. The imaginary plane chosen for the explanations is the back plane of block *C* identified as 6.

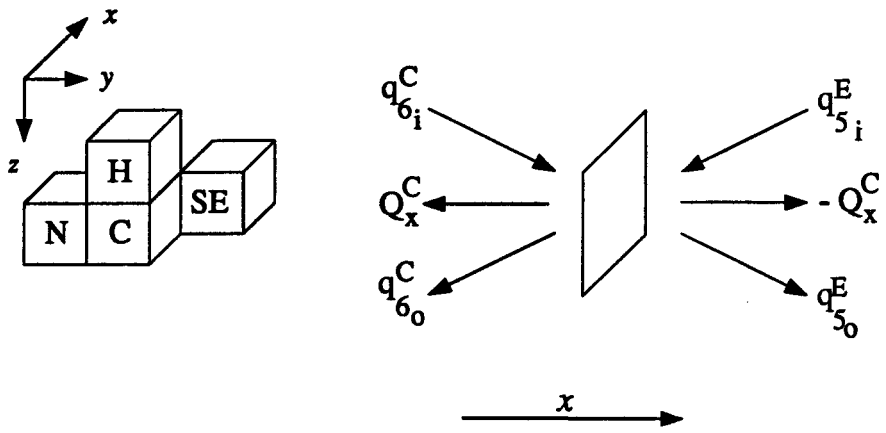

Figure 2.2 Relative positions of zones and the linking procedure for the *x* direction

The basic linking assumption for this plane is:

$$q^C_{6_i} = q^E_{5_o}$$
$$q^E_{5_i} = q^C_{6_o} \tag{2.17}$$

Of course, equation (2.13) can be applied to the given plane:

$$\frac{Q^C_x}{A^C_x} = q^C_{6_o} - q^C_{6_i} \tag{2.18}$$

According to the linking principle expressed by (2.17), the incident flux $q^C_{6_i}$ on surface *6* can be replaced with the leaving flux to the adjacent volume zone $q^E_{5_o}$:

$$\frac{Q^C_x}{A^C_x} = q^C_{6_o} - q^E_{5_o} \tag{2.19}$$

Introducing (2.16) into (2.19) and rearranging the terms result in the following equation for the x direction:

$$\begin{aligned}
&\left[\frac{Q_x^W}{A_x^W}B_{65}^C + \frac{Q_x^C}{A_x^C}\left(1 - B_{66}^C - B_{55}^E\right) + \frac{Q_x^E}{A_x^E}B_{56}^E\right] \\
&+ \left[\frac{Q_y^N}{A_y^N}B_{63}^C - \frac{Q_y^C}{A_y^C}B_{61}^C - \frac{Q_y^{NE}}{A_y^{NE}}B_{53}^E + \frac{Q_y^{NE}}{A_y^{NE}}B_{51}^E\right] \\
&+ \left[\frac{Q_z^H}{A_z^H}B_{62}^C - \frac{Q_z^C}{A_z^C}B_{64}^C - \frac{Q_z^{HE}}{A_z^{HE}}B_{52}^E + \frac{Q_z^E}{A_z^E}B_{54}^E\right] \\
&= \sum_{j=1}^{6} B_{6j}^C\left(\epsilon_j^C E_j^C + \frac{\left(1-\epsilon_j^C\right)E_g^C \overline{gs}_j^C}{A_j^C}\right) \\
&- \sum_{j=1}^{6} B_{5j}^E\left(\epsilon_j^E E_j^E + \frac{\left(1-\epsilon_j^E\right)E_g^E \overline{gs}_j^E}{A_j^E}\right)
\end{aligned} \tag{2.20}$$

The energy balance in zone C can be similarly written for the imaginary fluxes in the y and z directions.

Equation (2.20) with the corresponding equations in the y and z directions can be expressed in a matrix form to facilitate computation:

$$[BM]\{\mathbf{Q}\} = \{\mathbf{CM}\} \tag{2.21}$$

The solution for $\mathbf{Q}$ gives the unknown imaginary fluxes

$$\{\mathbf{Q}\} = [BM]^{-1}\{\mathbf{CM}\} \tag{2.22}$$

and equation (2.16) can now be solved for the radiative fluxes on the real surfaces of an enclosure.

In the case of high spatial divisions, the set of equations cannot be solved economically with direct methods (for example the Gaussian elimination), or the solution is hindered by excessive storage requirement. An economical way of storage of matrix BM and an iterative solution for the set of equations (2.21) is proposed in Appendix A.

The radiative source term in a gas zone is given by summing all the net radiative heat rates on the imaginary planes and on the real walls (if any) of the zone.

$$S_k = \sum_{i=1}^{m} Q_i + \sum_{i=m+1}^{6} q_i A_i \tag{2.23}$$

where m is the number of imaginary planes in the zone.

Generally radiation problems also involve conduction, convection and fluid flow. In order to determine the unknown zone temperatures, an overall energy balance must be written including the radiative heat fluxes. This results in a set of nonlinear equations which can be solved iteratively.

More details on the IPM can be found in Larouche (1988) .

2.3 Discrete transfer method

The discrete transfer method was developed by Shah (1979). The method is a combination of the zone, the flux and the Monte Carlo methods. Similar to the zone method, the radiation space is divided into finite volumes, or zones, in which the temperatures and radiative properties are assumed to be uniform.

For a pencil of ray with intensity I and solid angle $d\Omega$ around the directional vector s crossing a layer of gray gas with an absorption coefficient of K and a black-body intensity of I_b, the equation of radiative transfer can be written as :

$$\frac{dI}{ds} = -KI + KI_b \tag{2.24}$$

The change of intensity over the path length ds expressed by the left hand side of the equation is due to the loss by absorption and the gain by spontaneous emission of the medium in the given direction, supposing constant temperature along the path.

This equation can be analytically integrated and discretized along the path of the ray, yielding

$$I_{n+1} = I_n e^{-Ks} + \left(1 - e^{-Ks}\right)\frac{\sigma T_g^4}{\pi} \tag{2.25}$$

where I_n is the intensity entering the zone, I_{n+1} is the intensity leaving the zone , s is the distance the ray travelled in the zone. The resulting recurrence relation can be applied repeatedly along the path of the rays in the enclosure. Figure 2.3 illustrates the path of a ray through non—uniform zones.

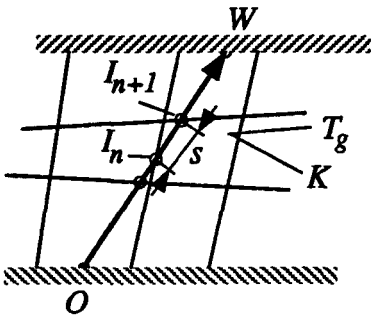

Figure 2.3 Path of a ray emitted from point O

Since the discussion concerns gray lambertian surfaces, the intensity leaving a boundary surface zone of the enclosure can be written:

$$I_o = \frac{q_o}{\pi} = (1-\epsilon)\frac{q_i}{\pi} + \frac{\epsilon\sigma T_s^4}{\pi} \tag{2.26}$$

On the other hand, the net flux on a wall is:

$$q_{net} = q_o - q_i \tag{2.27}$$

The incident flux turns out to be unknown in both the boundary condition equation (2.26) and the energy balance equation (2.27). However, it can be calculated by integrating the incoming intensities over the hemisphere:

$$q_i = \int_{2\pi} I \cos\beta \, d\Omega \tag{2.28}$$

where β is the angle between the incident intensity and the surface normal. For the calculation of the incident fluxes, the hemisphere over the surface zone has to be discretized into a number of small solid angles. The center of each solid angle fixes the direction of the rays impinging onto the middle of the wall zone. The incident intensities are summed over the whole hemisphere seen by the given surface zone. The intensities of the rays just before hitting the wall zone can be calculated using the equation of emission (2.26) and the recurrence relation (2.25).

In black enclosures (ϵ=1), the outgoing flux q_o is independent of the incident flux q_i, so that the net heat flux to a surface zone can be obtained in one step by calculating q_i. In the case of emissivities less than one, the outgoing flux q_o is dependent on the incident flux q_i, thus the net heat flux has to be calculated iteratively. An initial q_i distribution is assumed which determines the boundary intensity distribution (equation 2.26). The incident fluxes are calculated on the surfaces as explained previously. If the resulting and the initial incident flux distributions do not agree within a given tolerance, the above calculation is repeated until convergence is reached. The lower the surface emissivity is, the higher the number of iterations is.

The volumetric source term can be obtained by adding the energy "left" behind by a pencil of rays as they cross the volume zones. The energy accumulation in volume zone n when a pencil of ray passes through it can be written as:

$$S_n = (I_{n+1} - I_n) dA \cos\beta \, d\Omega \tag{2.29}$$

The pencil of ray emitted from the surface element dA in the solid angle $d\Omega$ is assumed to cross the zone with all the energy concentrated in the center of the pencil. In fact on the right hand side of equation (2.29) dA should be considered as the area on the surface

of the volume zone that the ray covers on impinging. The determination of this area would cause difficulties in the calculation since it can be only a fraction of the surface. Therefore, the area on the surface that is emitting the pencil of rays is selected for this calculation, as suggested by Shah (1979). This simplification can lead to inaccurate results if a low number of divisions are used in the discretization of the hemisphere over the emitting surface element. Problems are also encountered when curvilinear grids are used, as will be seen in Chapter 6.

3

Geometrical foundations of the radiation methods

Thermal radiation is strongly dependent on the geometrical configuration of the physical system. Radiation modelling methods rely on geometry in different ways. A common way of taking the geometry into consideration is the application of ray tracing techniques. The discrete transfer (DT) method, as described in chapter 2, is based directly on ray tracing, while the zone and the imaginary planes (IPM) methods treat the geometry with the concept of interchange areas. The interchange areas can be calculated efficiently by the Monte Carlo technique which can be applied for any geometrical configuration. Monte Carlo method also uses ray tracing. In this chapter, the geometrical concepts of the three methods will be summarized and ray tracing in different systems will be explained.

3.1 Interchange areas

3.1.1 Direct interchange areas

The radiative exchange between two black surfaces elements A_i, A_j or between a gas volume and a black surface element V_i, A_j in the presence of an absorbing medium

can be expressed with the aid of the direct exchange area concept of Hottel et al. (1967)

$$\overline{s_i s_j} = \int_{A_i}\int_{A_j} \frac{dA_i \cos\theta_i \, dA_j \cos\theta_j \, \tau(r)}{\pi r^2}$$
$$\overline{g_i s_j} = \int_{V_i}\int_{A_j} \frac{K_i dV_i \, dA_j \cos\theta_j \, \tau(r)}{\pi r^2} \qquad (3.1)$$

where $\tau(r)$is the transmissivity of the intervening gas.

The IPM method treats radiation as a local phenomenon inside the zones which are linked by the imaginary fluxes. In this method, the geometrical aspects are taken care of by the direct interchange areas and the reception factors. Following the definition of the direct interchange areas (DIA), the wall zones are considered black for the calculation.

For a gas volume bounded by n black surfaces the following relation holds:

$$\sum_{j=1}^{n} \overline{s_i s_j} + \overline{g s_i} = A_i \quad i = 1...n \qquad (3.2)$$

The direct interchange areas can also be expressed in a product form

$$\overline{s_i s_j} = A_i f_{ij}$$
$$\overline{s_i g} = A_i f_{ig} \qquad (3.3)$$
$$\overline{g s_i} = 4KV f_{gi}$$

where the last terms of the right hand side products are the reception factors. Incorporating equation (3.3) in (3.2) and making use of the law of reciprocity ($\overline{g s_i} = \overline{s_i g}$), one obtains:

$$\sum_{j=1}^{n} f_{ij} + f_{ig} = 1 \qquad i = 1...n \qquad (3.4)$$

The physical meaning of the reception factors can be explained as the fraction of the total radiation energy emitted by the *i-th* surface which is intercepted by the *j-th* surface or the gas.

The reception factors for simple geometrical configurations like cubes can be found analytically by evaluating the double integrals of equation (3.1), but for volumes with irregular geometry it is intractable. It is necessary to find a way of calculation which can yield the reception factors independently of the geometrical complexity. The Monte Carlo method can be applied successfully in these cases.

3.1.2 Total interchange areas

The zone method incorporates the geometrical factors through the so-called total interchange areas (TIAs). The total-interchange areas can be considered as a measure of the effect of the size and shape of the system as well as its radiative properties, their dimensions being those of an area. They express numerically the way a zone sees an other zone of the enclosure directly and via reflections.

The TIAs can be obtained using the following expressions

$$\begin{aligned} \overline{S_iS_j} &= A_i\epsilon_i\,\varphi_{ij} \\ \overline{S_iG_j} &= A_i\epsilon_i\,\varphi_{ij} \\ \overline{G_iS_j} &= 4K_iV_i\,\varphi_{ij} \\ \overline{G_iG_j} &= 4K_iV_i\,\varphi_{ij} \end{aligned} \tag{3.5}$$

where φ_{ij} represents the total reception factors between two zones i and j (directly and assisted by reflections at the surface zones). The summation of the TIAs results in:

$$\begin{aligned} \sum_j \overline{S_iS_j} + \sum_j \overline{S_iG_j} &= A_i\epsilon_i \\ \sum_j \overline{G_iS_j} + \sum_j \overline{G_iG_j} &= 4K_iV_i \end{aligned} \tag{3.6}$$

Equations (3.6) can be simplified by dividing by $A_i\epsilon_i$ and $4K_iV_i$ respectively, thus giving

$$\sum_j \varphi_{ij} = 1 \tag{3.7}$$

The Monte Carlo technique can be successfully used for the total reception factor calculation, as it is explained in the following section.

3.2 Interchange area calculation by the Monte Carlo technique

3.2.1 Principles of the Monte Carlo method

The Monte Carlo method, as its name implies, is a statistical numerical method. If the distribution of the values (events) that occur in a physical process is known (e. g. Planck distribution of intensities versus wavelength for a blackbody), the procedure of Monte Carlo is to assign a wavelength to each of a huge number of emitted beams (at least 5000) in such a way that the known physical distribution can be reproduced. Moreover, each of the assignment should be independent of each other to have a good statistical representation. These conditions are fulfilled by forming cumulative distribution functions and then using random numbers (from 0 to 1) to extract the desired variable (the wavelength in the example given above).

The Monte Carlo method can be used successfully for radiation modelling. An excellent discussion is given in Siegel and Howell (1983). In this technique, radiation exchange is modelled by the emission and absorption of discrete amounts of energy which can be called "energy bundles". Local energy flux can then be computed by knowing the number of these bundles arriving per unit area and time at some position. Figure 3.1 illustrates surface dA_1 and surface A_2 which are in radiation interchange with each other. Since dA_1 is emitting in a hemisphere, the direction of emission can be characterized

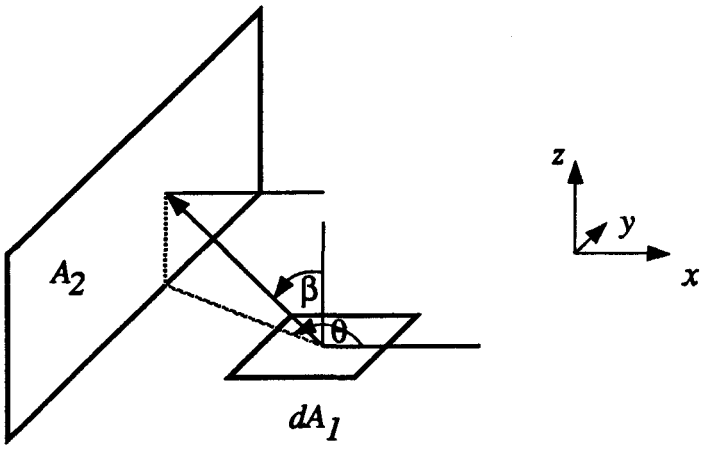

Figure 3.1 Radiation interaction between a differential surface dA_1 and a finite surface A_2

by the circumferential angle θ and the cone angle β. The hemisphere is covered by β varying from 0 to $\pi/2$ and θ from 0 to 2π. Circumferential angle θ can be obtained randomly by:

$$\theta = 2\pi R_1, \tag{3.8}$$

where R_1 is a random number in the open interval of 0 to 1. Hereafter random numbers will be denoted by R. Samples for the cone angle can be obtained directly from the cumulative distribution function of β, which is the probability that the cone angle will be between 0 and β.

$$\beta = \sin^{-1}\left(\sqrt{R_2}\right). \tag{3.9}$$

If the bundles are emitted from a gas zone, the cone angle may vary from 0 to π. The randomly selected values of β are then obtained by:

$$\beta = \cos^{-1}(1 - 2R_2) \tag{3.10}$$

Since the emission takes place in an absorbing and emitting gas, the length of travel of each bundle before absorption should be obtained. A similar procedure leads to:

$$L = \frac{-ln(R_3)}{K} \tag{3.11}$$

The gas permits the bundle to travel the distance L, but in the meantime it can hit a wall. In this case a random number can decide whether the bundle is absorbed or reflected. If the random number is smaller than the surface absorptivity, the bundle is absorbed:

$$\epsilon \geq R_4 \tag{3.12}$$

If it is higher, the bundle is reflected and the process of bundle tracing should be continued.

In the present example energy bundles are emitted from the center of a differential surface dA_1 to A_2. If the interaction between two finite surfaces A_1 and A_2 is examined, it can be seen that the same process could be repeated with dA_1 at randomly selected positions on A_1 and with dA_2 at randomly selected positions on A_2. The position on a plane can be described by two freely selected coordinates, so two more random numbers (R_5, R_6) need to be generated. Having a rectangular surface element with boundary coordinates x_1, y_1, x_2, y_2, the place of emission is given by:

$$\begin{aligned} x_e &= x_1 + (x_2 - x_1)R_5 \\ y_e &= y_1 + (y_2 - y_1)R_6 \end{aligned} \tag{3.13}$$

The emission point from a rectangular gas zone is determined by using (3.14), which incorporates the third coordinate direction of the cartesian space:

$$\begin{aligned} x_e &= x_1 + (x_2 - x_1)R_5 \\ y_e &= y_1 + (y_2 - y_1)R_6 \\ z_e &= z_1 + (z_2 - z_1)R_7 \end{aligned} \tag{3.14}$$

3.2.2 The Monte Carlo method for reception factor calculation

Direct reception factor In the present study, the direct reception factors are used only in the imaginary planes method. Since this method treats each zone separately, the evaluation of the direct reception factors is confined to individual volume zones. Since it is not necessary to assign energy to the bundles for the reception factor calculation, they will be called rays. All the surfaces surrounding a volume zone are assumed to be black. Rays emitted from a surface are intercepted by the other surfaces or by the gas. The *place*, the *direction of emission* and the *length of travel* are obtained by generating random numbers as explained previously. The total number of rays intercepted by a given surface divided by the total number of rays originated from the emitting surface gives the reception factor between the two surfaces. The sum of the reception factors on a given surface should be *1* according to equation (3.4). Since no ray can escape from a closed enclosure, the sum of rays intercepted by the walls and the gas should necessarily give the number of emitted rays from a given surface.

Total reception factors In the case of the total reception factor calculation, all the surface and gas zones in the radiation space have to be considered, since these factors are used in the zone method. No energy is assigned to the emitted rays from the walls. The rays are emitted by a gas or a surface zone according to the rules already mentioned. However the length of travel calculations have to be modified if the absorption coefficients of the gas space is not uniform. According to Cannon (1967) it can be written

$$\sum_i K_i s_i \leq -\ln R \tag{3.15}$$

where K_i is the absorption coefficient of a particular zone and s_i is the distance travelled by the ray along its path in that zone. The rays are absorbed in a gas zone if the sum of the optical thicknesses along its path exceeds the negative of the logarithm of the generated random number. Reflection is accounted for at the walls. The sum of the rays intercepted by zone j divided by the number of rays emitted by zone i gives the total reception factor between zone i and j. The sum of all the total reception factors on a zone should necessary be 1 in a closed enclosure.

3.3 Geometrical details of the discrete transfer method

The hemisphere over a zone surface is divided into small solid angles by N_β cone angle divisions and N_θ circumferential divisions. The rays are emitted from the center of a surface zone (cell) in $N_\beta \times N_\theta$ directions. The rays are followed on their way crossing the zones, storing the distance travelled in each volume zone, the temperature and the absorption coefficient of the zone until a boundary surface is hit. Then a "backtracking" step starts which involves the calculation of intensity $I(\beta, \theta)$ at point O (see Figure 2.3) using the recurrence formula (2.25), starting from the intensity at point W given by equation (2.26).

The total incident flux can be calculated from the discretized form of equation (2.28):

$$q_i = \sum_{\beta,\theta} I(\beta, \theta) \sin\beta \cos\beta \, d\beta \, d\theta \tag{3.16}$$

3.4 Ray tracing in polyhedra

The ray tracing inside a single zone can be identified as the principal event of ray tracing in 3D systems. While the IPM method needs tracking the rays inside a single zone, the zone and the DT methods require ray tracing in a 3D grid of zones. Ray tracing in a grid of zones can be realized with the repeated application of ray tracing in a single zone. Although the zone and DT methods use generally the same approach, in the zone method a ray can be absorbed in the gas space along its path, while the rays have to be followed until they hit a boundary in the case of DT method.

A ray tracing method will be described for zones with planar walls. The only geometrical constraint imposed is that the enclosure should be convex, i.e. the angle between the neighboring planar walls should be less than 180°. This will enable the use of irregular zone sizing (i.e. other than rectangular or cylindrical ...) and of curvilinear coordinate system for solving radiation problems with the zone, IPM and DT methods.

The irregular geometry should be divided into finite volume zones having planar surfaces. It can be done with the help of a curvilinear grid generation technique. In the present discussion the number of planar surfaces surrounding the zones is restricted to six, i.e. the method will be performed with *hexahedra.*

Figure 3.2 explains the logical structure of the ray tracing. The branch drawn with thick line is used in the case of a multiple zone arrangement. When using the discrete transfer method, the gas absorption block should be omitted. The *direction of emission* and *place of emission* steps are realized differently by the Monte Carlo and the discrete transfer methods, as will be explained later.

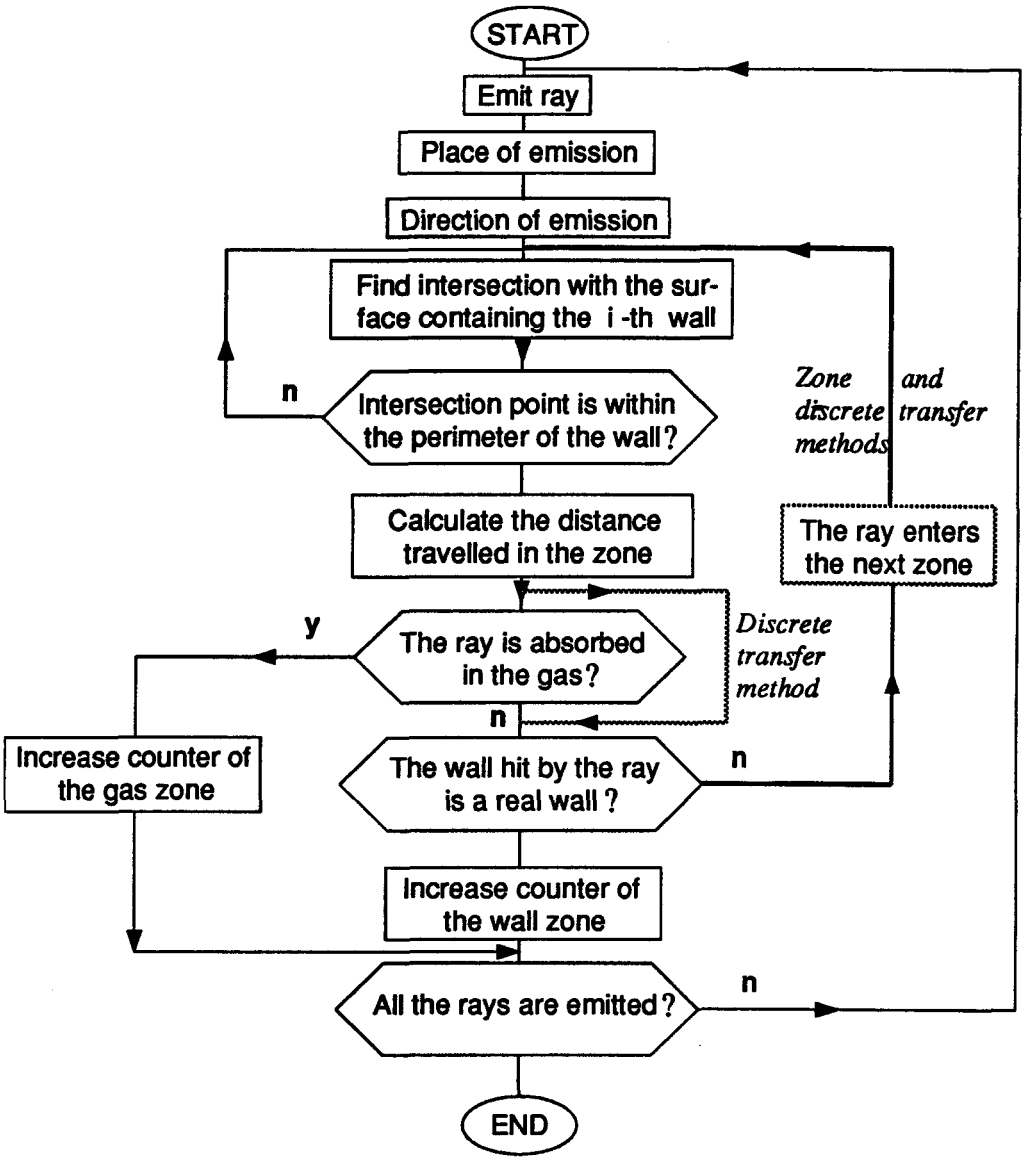

Figure 3.2 The flowchart of the ray tracing algorithm

The main elements of the ray tracing algorithm will now be discussed in detail. All the calculations and discussions are related to 3D cartesian space. Points in the 3D space are noted by P and a subscript. Vector analisys is extensively used in the presentation. Vectors from the origin to the different points are always referred to by $\mathbf{r}$ with a subscript.

In an enclosure surrounded by six planar surfaces, the surfaces are considered to have four corners numbered counterclockwise according to Figure 3.3.

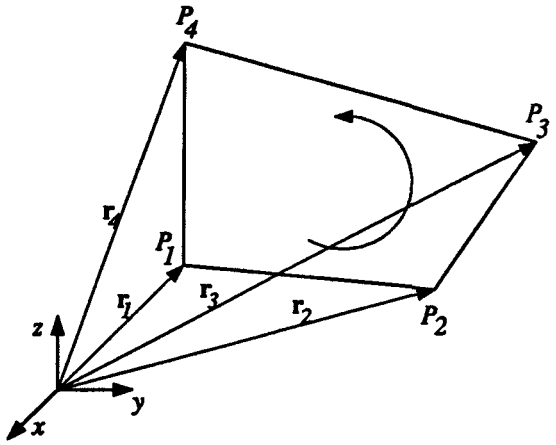

Figure 3.3 Identification of the wall corners

Although the first step in ray tracing is to decide on the coordinates of the emission point, for convenience of explanation this part will be discussed later on in section 3.4.4.

3.4.1 Direction of emission

The emission from a given point of a planar surface occurs in a hemisphere over the surface point. The Monte Carlo method determines the direction of emission by two randomly determined angles if a coordinate axis is parallel to the surface normal: the circumferential angle θ and the cone angle β.

In the discrete transfer method, the circumferential angle θ and the cone angle β are obtained from the division of the hemisphere into small solid angles.

For calculation purposes, it is convenient to assign a *directional vector* to the direction of emission. If the surface normal is parallel to a coordinate axis, for example parallel with the z axis, the direction of emission over the x,y plane can be decided with

the unity vector

$$\mathbf{d}^* = \begin{bmatrix} \cos\theta \sin\beta \\ \sin\theta \sin\beta \\ \cos\beta \end{bmatrix} \tag{3.17}$$

For an arbitrarily positioned plane, the surface normal vector is **n**. This vector can be rotated by using two consecutive rotations to bring it into the z coordinate direction as shown in Figure 3.4. The two consecutive rotations are:

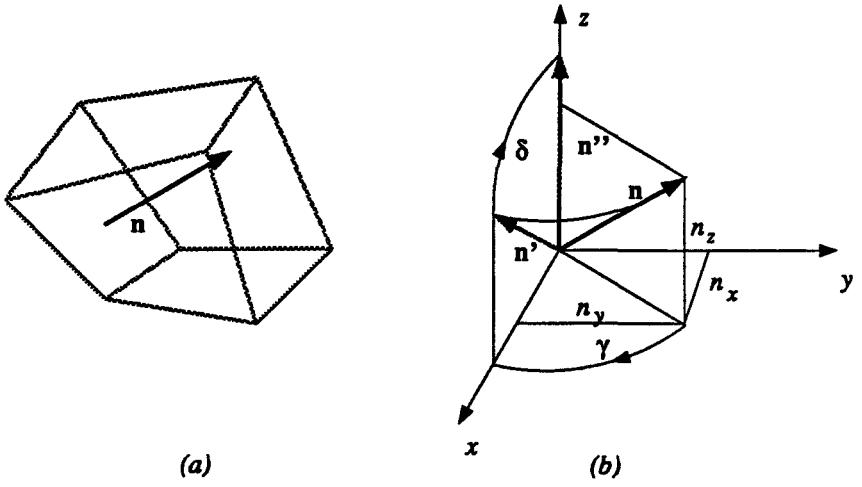

Figure 3.4 (a) Surface normal on an arbitrarily positioned plane (b) Bringing the normal parallel to the z axis by using two consecutive rotations

1. clockwise rotation with angle γ around the z axis resulting in **n'**
2. clockwise rotation with angle δ around the y axis resulting in **n''** (Figure 3.4)

The angles of rotation can be calculated from the x, y, z directional components of the

surface normal vector **n**.

$$\mathbf{n}^{\mathrm{T}} = [n_x, n_y, n_z]$$

$$\gamma = \begin{cases} \arctan(n_y/n_x) & n_x > 0,\ n_y > 0 \\ 2\pi - \arctan(|n_y/n_x|) & n_x > 0,\ n_y < 0 \\ \pi - \arctan(|n_y/n_x|) & n_x < 0,\ n_y > 0 \\ \pi + \arctan(|n_y/n_x|) & n_x < 0,\ n_y < 0 \\ \pi/2 & n_x = 0,\ n_y > 0 \\ \pi & n_x < 0,\ n_y = 0 \\ 3\pi/2 & n_x = 0,\ n_y < 0 \\ 0 & n_x > 0,\ n_y = 0 \\ \textit{direct. surf. normal} & n_x = 0,\ n_y = 0 \end{cases} \qquad (3.18)$$

$$\delta = \begin{cases} \arccos\left(\frac{n_z}{\sqrt{n_x^2+n_y^2+n_z^2}}\right) & n_z \geq 0 \\ \pi - \arccos\left(\frac{-n_z}{\sqrt{n_x^2+n_y^2+n_z^2}}\right) & n_z < 0 \end{cases}$$

The direction of emission over the *x, y* coordinate plane determined by equation (3.17) can be transformed to give the direction of emission over the arbitrarily positioned plane. This is done by performing the two rotations already described on Figure 3.4 in reverse direction starting with δ and then γ. The transformation can be expressed in a matrix form, resulting in the directional vector of emission **d** from the arbitrarily positioned plane:

$$\mathbf{d} = \mathbf{M}_\gamma \mathbf{M}_\delta \mathbf{d}^*$$

$$\begin{bmatrix} d_x \\ d_y \\ d_z \end{bmatrix} = \begin{bmatrix} \cos\gamma & -\sin\gamma & 0 \\ \sin\gamma & \cos\gamma & 0 \\ 0 & 0 & 1 \end{bmatrix} \begin{bmatrix} \cos\delta & 0 & \sin\delta \\ 0 & 1 & 0 \\ -\sin\delta & 0 & \cos\delta \end{bmatrix} \begin{bmatrix} d_x^* \\ d_y^* \\ d_z^* \end{bmatrix} \qquad (3.19)$$

The process is illustrated by Figure 3.5. To summarize, the procedure to obtain the direction of emission **d** from a plane of surface normal **n** is as follows:

1. Determine the position of **n** relative to the direction *(0,0,1)*[1] by computing γ and δ from equation (3.18)

[1] other coordinate directions are also permitted

2. Generate the cone angle β and circumferential angle θ of emission, and form the directional vector $\mathbf{d}^*$ (equation 3.17)
3. Rotate $\mathbf{d}^*$ with the transformation given by equation (3.19) to obtain the direction of emission $\mathbf{d}$

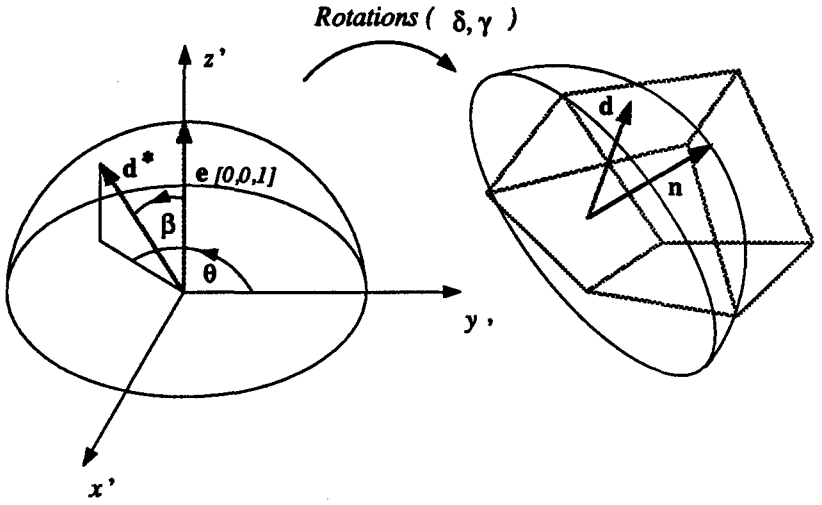

Figure 3.5 Obtaining the direction of emission on the arbitrarily positioned plane

The emission takes place in a hemisphere from diffuse surfaces. The above procedure takes advantage of the axisymmetrical nature of emission in determining the direction of emission. Only two rotations are applied to move $\mathbf{d}^*$ into $\mathbf{d}$, whereas, in general, to rotate an object from a given angular position to another (specified), three rotations have to be employed around the x, y and z axes of the coordinate system. The basic 3D theory of objects is discussed in detail by Watt (1989).

3.4.2 Intersection point with the plane passing through a wall

The path of a ray can be described by a line equation using the emission point P_e, the direction of emission $\mathbf{d}$ and $\mathbf{r}$ pointing to any location on the line depending on the

value of the parameter t (Figure 3.6a):

$$\mathbf{r} = \mathbf{r_e} + t\,\mathbf{d} \tag{3.20}$$

with coordinates:

$$x = x_e + td_x$$

$$y = y_e + td_y$$

$$z = z_e + td_z$$

The path of the ray starts at the emission point and continues on the line in the direction of emission, thus, negative values for the parameter t are not permitted.

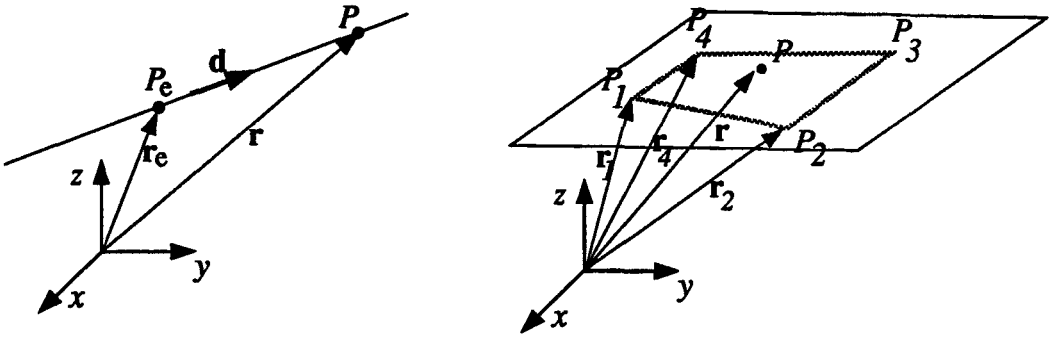

(a) (b)

Figure 3.6 Vectorized description of *(a)* a line *(b)* a plane

On the other hand, the general equation of a plane in a three dimensional cartesian space can be written as:

$$Ax + By + Cz + D = 0 \tag{3.21}$$

In the present situation, four points of every plane are given, these points being the corner points of a wall (Figure 3.6b). Three points are enough to define a plane. If $\mathbf{r}$ is a general vector describing the plane, then, with the help of the vectors $\mathbf{r_1}$, $\mathbf{r_2}$, $\mathbf{r_4}$ pointing at the corner points P_1, P_2, P_4, the plane equation can be given by the mixed product:

$$(\mathbf{r} - \mathbf{r_1}) \cdot (\mathbf{r_2} - \mathbf{r_1}) \times (\mathbf{r_4} - \mathbf{r_1}) = 0 \tag{3.22}$$

or:

$$\begin{vmatrix} x - x_1 & y - y_1 & z - z_1 \\ x_2 - x_1 & y_2 - y_1 & z_2 - z_1 \\ x_4 - x_1 & y_4 - y_1 & z_4 - z_1 \end{vmatrix} = 0$$

From the determinant the coefficients A, B, C, and D of the equation of the plane can be easily found.

The intersection point of the plane and the line can be obtained by solving the set of equations (3.20) and (3.21) for the parameter t:

$$t = \frac{-(Ax_e + By_e + Cz_e + D)}{Ad_x + Bd_y + Cd_z} \tag{3.23}$$

With the help of the parameter, the intersection point P_i can be obtained from equation (3.20). If the parameter t has a positive value, then P_i is taken as the intersection point of the path of the ray and the plane passing through that wall.

3.4.3 Determination of the place of the intersection point

If a ray hits a plane passing through a wall, it has to be decided whether the intersection point P_i is within the boundaries of that wall. The 3D problem can be reduced to 2D simply by projecting the wall on a coordinate plane as illustrated by Figure 3.7. The projection on a coordinate plane is equal to ignoring the coordinate along which

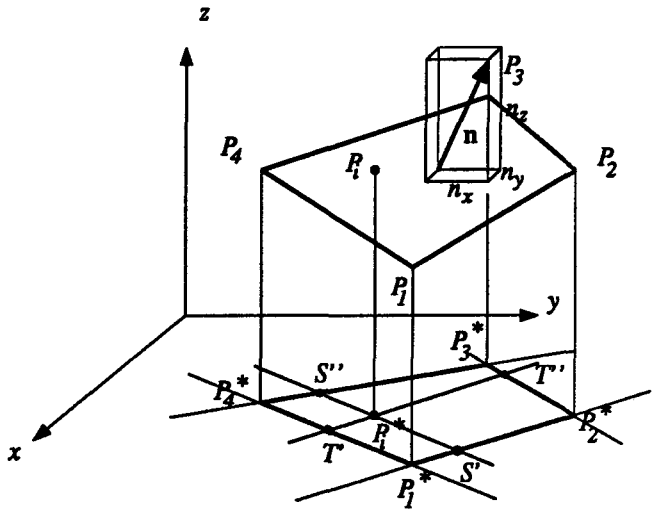

Figure 3.7 Projection of a wall on a coordinate plane (x, y in this case)

the projection is made from every point. Before initiating the projection, it is necessary to decide which coordinate plane would give the most advantageous projected picture. This can be defined as the picture which gives a projected area closest to the area of the wall. The direction of projection can be decided on by finding the maximum of the absolute values of the normal vector components for the wall. The coordinate, which the maximum vector component belongs to, is the direction of projection.

$$\max\{|n_x|, |n_y|, |n_z|\} \rightarrowtail \textit{gives the component to be omitted from the wall coordinates} \tag{3.24}$$

Now the problem is reduced to finding out whether the point P^*_i is inside the polygon $P^*_1P^*_2P^*_3P^*_4$. The method to solve this problem is explained using Figure 3.7. First a side of the polygon for example $P^*_1P^*_4$ is selected. A straight line is drawn parallel to $P^*_1P^*_4$ through P^*_i. This line should cross the two neighboring sides $P^*_1P^*_2$ and $P^*_3P^*_4$, resulting in intersection points S' and S'' (since the line is parallel to the

side $P^*_1P^*_4$, the intersection points exist). The same process is then repeated selecting the side $P^*_1P^*_2$, and similarly intersection points T' and T'' are obtained.

If point P^*_i is located between the intersection points S' and S'' on the first parallel line and between T' and T'' on the second parallel line, point P^*_i is inside the polygon $P^*_1P^*_2P^*_3P^*_4$, and this means that the bundle did hit the wall defined by $P^*_1P^*_2P^*_3P^*_4$. Otherwise P^*_i is outside of $P^*_1P^*_2P^*_3P^*_4$ meaning that the ray hit another wall.

An efficient formula to compute line intersections is suggested by Harrington (1987). If line 1 is defined by two points $A\ (x_1,y_1)$ and $B\ (x_2,y_2)$, the equation can be written

$$(y_2 - y_1)x - (x_2 - x_1)y + x_2y_1 - x_1y_2 = 0 \tag{3.25}$$

or

$$r_1x + s_1y + t_1 = 0$$

where:

$$r_1 = y_2 - y_1$$

$$s_1 = -(x_2 - x_1)$$

$$t_1 = x_2y_1 - x_1y_2$$

If the same is done for line 2, then r_2, s_2, t_2 are introduced. The intersection point of lines 1 and 2 is then given by:

$$\left(\frac{s_1t_2 - s_2t_1}{s_2r_1 - s_1r_2}\right),\ \left(\frac{t_1r_2 - t_2r_1}{s_2r_1 - s_1r_2}\right) \tag{3.26}$$

The use of the above formula for line intersection computation is very advantageous because it eliminates the possible effect of round off errors introduced in the calculation

if a line is almost parallel with a coordinate axis. In such a case, problems could be encountered if the following well known formula is used:

$$y = mx + b \tag{3.27}$$

where

$$m = \frac{y_2 - y_1}{x_2 - x_1},$$

for line equations and for intersection point computation.

Having determined the intersection point P_i and the emission point P_e, or two successive intersection points P_i, P'_i, the distance s_i a ray travelled in a zone can now be calculated from :

$$s_i = \sqrt{(x_i - x_e)^2 + (y_i - y_e)^2 + (z_i - z_e)^2} \tag{3.28}$$

or from:

$$s_i = \sqrt{(x'_i - x_i)^2 + (y'_i - y_i)^2 + (z'_i - z_i)^2} \tag{3.29}$$

These distances are necessary for calculating the gas absorption with the Monte Carlo technique and for the backtracing procedure of the DT method.

3.4.4 Place of emission

According to the Monte Carlo technique the emission points have to be uniformly distributed over the emitting surface element, or inside the emitting gas element. If the cartesian coordinate axes are parallel to the surface or the volume boundaries (rectangles and parallelepipeds) the emission points can be determined by linear interpolation with equations (3.13) and (3.14). The emission point from surface or volume zones of arbitrary shape cannot be computed directly by linear interpolation in the coordinate directions.

However, a surface element with an arbitrary shape can be enclosed in a rectangle with sides parallel to the cartesian coordinate system, and, similarly, a volume with an arbitrary shape can be surrounded by a parallelepiped with edges in the cartesian coordinate directions. In the enclosing rectangle or parallelepiped the emission point is calculated by linear interpolation, and the point is accepted as an emission point (P_e) if it is located inside the arbitrary-shaped zone, otherwise it is discarded.

Figure 3.8 illustrates the process for a surface zone. The zone should be projected

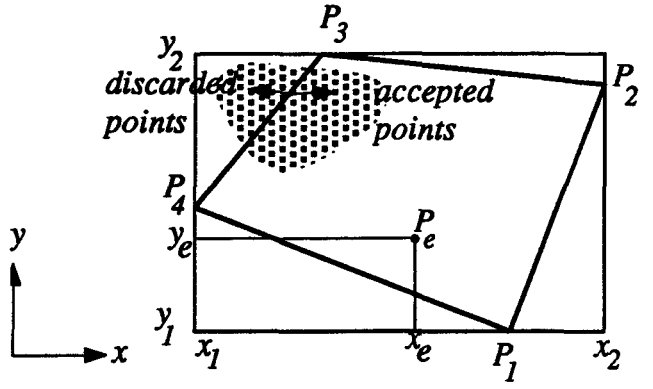

Figure 3.8 Point of emission from a wall zone

on a coordinate plane as explained in 3.4.3. The coordinates x_1, x_2 and y_1, y_2 of the bounding rectangle can be computed as:

$$\begin{aligned} x_1 &= \min(x_{P_1}, x_{P_2}, x_{P_3}, x_{P_4}) \\ x_2 &= \max(x_{P_1}, x_{P_2}, x_{P_3}, x_{P_4}) \\ y_1 &= \min(y_{P_1}, y_{P_2}, y_{P_3}, y_{P_4}) \\ y_2 &= \max(y_{P_1}, y_{P_2}, y_{P_3}, y_{P_4}) \end{aligned} \tag{3.30}$$

The emission point is generated inside the bounding rectangle with two random numbers according to (3.13). To decide whether an emission point P_e is inside the boundaries of P_1, P_2, P_3, P_4, the same process should be followed as for the intersection point calculation in 3.4.3.

For a volume zone a bounding parallelepiped of coordinates x_1, x_2, y_1, y_2 and z_1, z_2 is generated with coordinates computed from the minimum and maximum coordinate values of the eight corner points. The emission points in the bounding parallelepiped are given by linear interpolation according to (3.14) using three random numbers. To decide if the emission point P_e is inside the arbitrary-shaped zone, three lines a, b and c are drawn through P_e such that they are parallel to the three contour lines of the zone at a given corner (see Figure 3.9). The lines a, b and c must cross the planes of the opposing

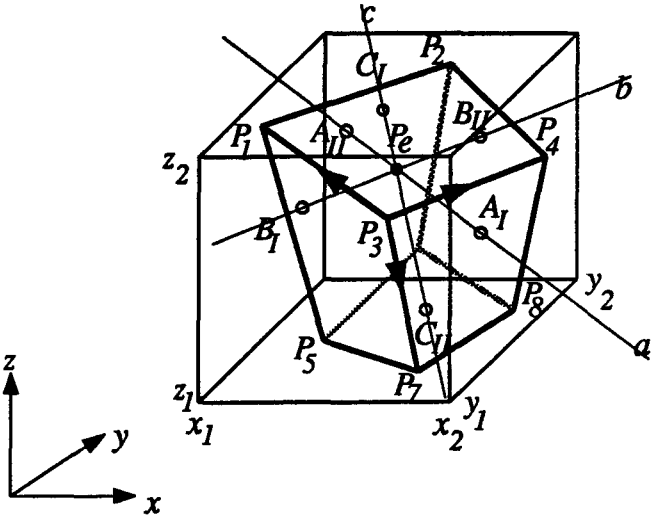

Figure 3.9 Place of emission from a gas volume

walls, since each contour line of a chosen corner crosses the planes of two opposing walls. If P_e is located between points A_I and A_{II} on line a, between points B_I and B_{II} on line b and between points C_I and C_{II} on line c, then the emission point is inside the hexahedron. It is enough to check only one coordinate for each line in the above process. This coordinate should be the one to which the maximum absolute value of the line directional vector components belong. This has to be done to avoid problems which could arise if the line drawn through the emission point is parallel to a coordinate plane.

The generation of emission points should be continued until a given number of emission points is found inside the surface or volume zone. The distribution of the emission points inside the zone will be uniform since the points are part of a larger uniformly distributed array of points.

3.4.5 Simplified emission point calculation

An arbitrary-shaped surface zone or gas zone can be regarded as a deformed rectangle or parallelepiped. To every emission point in the regular zone, a corresponding emission point is existing in the irregular zone. The emission point $P_e(x_e', y_e')$ on a rectangular surface element (Figure 3.10a) can be determined by using random numbers R_3 and R_4:

$$\begin{aligned} x_e' &= x_1' + (x_2' - x_1')R_3 \\ y_e' &= y_1' + (y_2' - y_1')R_4 \end{aligned} \tag{3.31}$$

The emission point on an arbitrary-shaped surface element (Figure 3.10b) can also be given by the use of the same interpolation principle. However, the emission points chosen in this manner will not be uniformly distributed over the area.

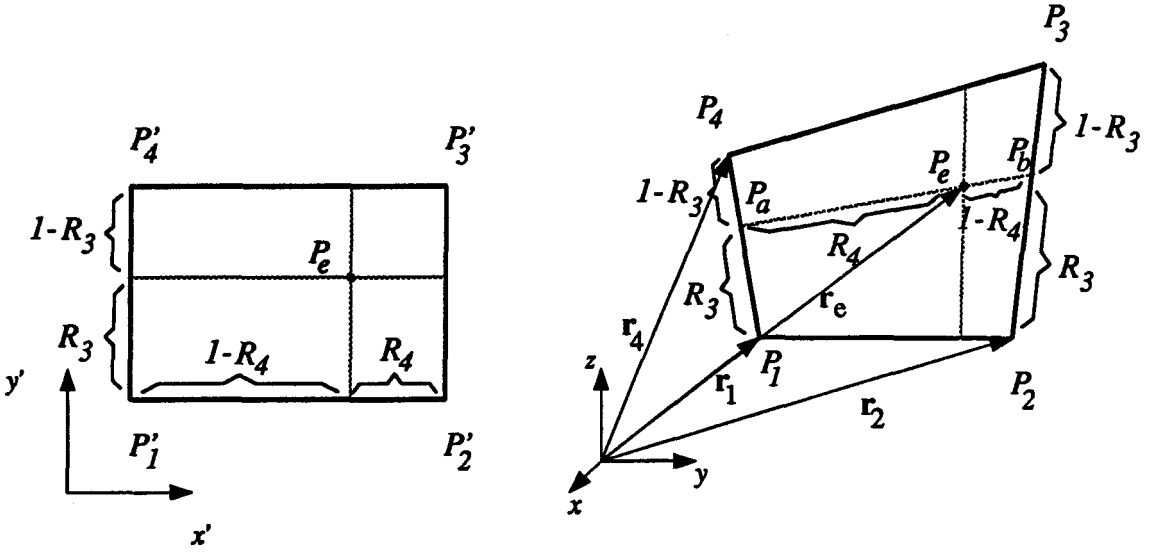

Figure 3.10 (a) Place of emission in a rectangle (b) Place of emission on an arbitrarily formed surface element

The sides P_1P_4 and P_2P_3 can be divided in two portions $(1–R_3)$ and R_3, thus introducing points P_a and P_b or in a vector notation $\mathbf{r_a}$ and $\mathbf{r_b}$. The point of emission P_e ($\mathbf{r_e}$) can be found on the line segment P_aP_b by dividing it in portions $(1–R_4)$ and R_4. It can be written in a vector notation:

$$\begin{aligned} \mathbf{r_a} &= \mathbf{r_1} + (\mathbf{r_4} - \mathbf{r_1})R_3 \\ \mathbf{r_b} &= \mathbf{r_2} + (\mathbf{r_3} - \mathbf{r_2})R_3 \\ \mathbf{r_e} &= \mathbf{r_a} + (\mathbf{r_b} - \mathbf{r_a})R_4 \end{aligned} \tag{3.32}$$

And by substituting $\mathbf{r_a}$ and $\mathbf{r_b}$ in the $\mathbf{r_e}$ relation, one obtains:

$$\begin{aligned} \mathbf{r_e} = \mathbf{r_1}(1 - R_3)(1 - R_4) + \mathbf{r_2}(1 - R_3)(R_4) + \\ \mathbf{r_3}(R_3)(R_4) + \mathbf{r_4}(R_3)(1 - R_4) \end{aligned} \tag{3.33}$$

In the zone method, emission points have to be calculated also from the volume zones. In a volume zone there is one more degree of freedom and therefore one more random number is necessary. With the help of two random numbers one point can be determined

as described above on each of two opposing walls . The line connecting the two points is then divided in a ratio given by the third random number, thus yielding the point of emission.

The error in the interchange area calculation, when using the simplified emission point calculation, is reasonable if the form of the arbitrary zone does not differ too much from that of a regular zone, i.e. from a rectangle or a parallelepiped. An example is given in appendix C which compares the accuracy of the two techniques of emission.

Point of emission for the discrete transfer method In the discrete transfer method, the rays are emitted from the center of the surface zones. For irregularly shaped polygons the middle point is not defined. However, if in equation (3.33) the random numbers are replaced by 0.5, the resulting point P_e is taken as the approximate middle point.

3.4.6 Area and volume calculation for hexahedra

Area The volume zones were defined as bounded by planar walls. Given the coordinates of the corners, the area of an arbitrary-shaped four corner polygon can be calculated by dividing the polygon into two triangles (Figure 3.11).

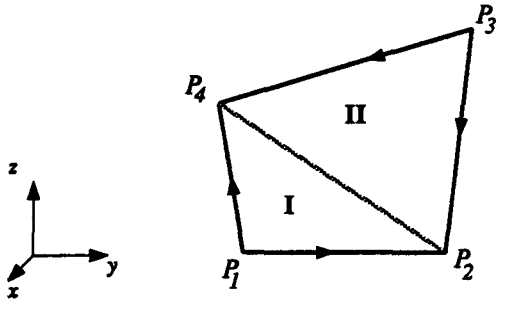

Figure 3.11 Division of a zone into two triangles for surface calculation

The area of the individual triangles can be obtained through the cross products as follows:

$$A_I = \frac{1}{2}\left|\overrightarrow{P_1P_2} \times \overrightarrow{P_1P_4}\right|$$
$$A_{II} = \frac{1}{2}\left|\overrightarrow{P_3P_4} \times \overrightarrow{P_3P_2}\right| \tag{3.34}$$

And the total area is readily obtained by

$$A = A_I + A_{II} \tag{3.35}$$

Volume A hexahedron can be divided into 5 tetrahedra as Figure 3.12 shows.

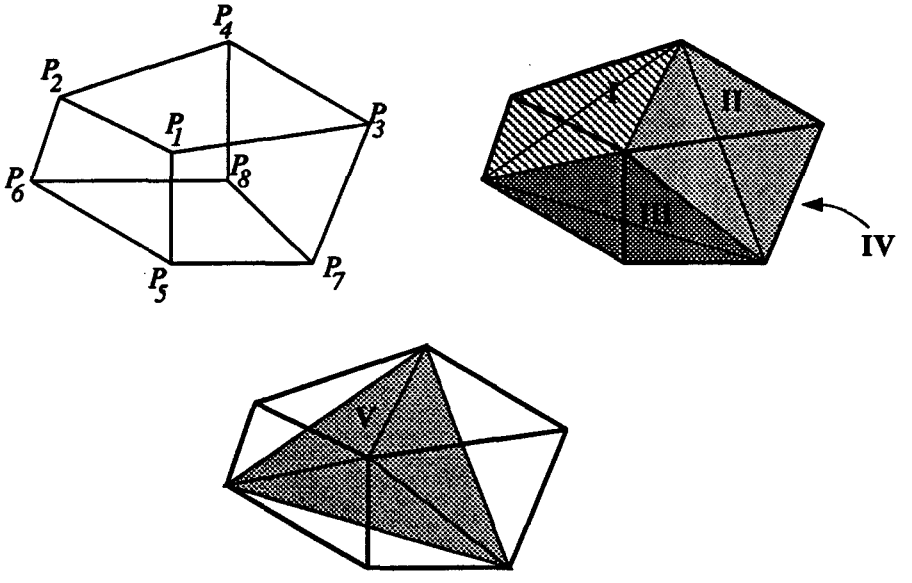

Figure 3.12 Division of a zone into tetrahedra for volume calculation

The volume of a hexahedron is given by the sum of the volumes of the tetrahedra

$$V = V_I + V_{II} + V_{III} + V_{IV} + V_V \tag{3.36}$$

where the volumes V_I, V_{II}, V_{III}, V_{IV}, V_V can be obtained by the mixed product of their three side vectors starting from the same corner. The calculation is presented for tetrahedron I.

$$V_I = \frac{1}{6}\left|\left(\overrightarrow{P_2P_1}\right)\cdot\left(\overrightarrow{P_2P_4}\times\overrightarrow{P_2P_6}\right)\right| \tag{3.37}$$

An assessment of the Monte Carlo technique applied to the computation of direct interchange areas for irregular shapes and making use of the techniques described in sections 3.2 and 3.3, is given in Appendix C.

3.5 Ray tracing in cylindrical sections

The flowchart of ray tracing in polyhedra of irregular systems apply in the case of cylindrical systems as well. The main elements of the ray tracing process will be explained for cylindrical systems. Both the cylindrical and the cartesian coordinate systems are used throughout the ray tracing process. The two coordinate systems are positioned with common z coordinate axis and with ϕ coordinate starting from the x axis and running in counterclockwise direction. The conversion between the x, y, z coordinates and the r, ϕ, z coordinates of any point in the 3D space is a simple transformation process. A cylindrical sector bounded by the coordinate surfaces of the cylindrical coordinate system belonging to r_1, r_2, ϕ_1, ϕ_2 and z_1, z_2 coordinates is drawn on Figure 3.13. The boundary walls of the cylindrical sector are numbered in the lower right corner to have a simple and clear reference in the discussion.

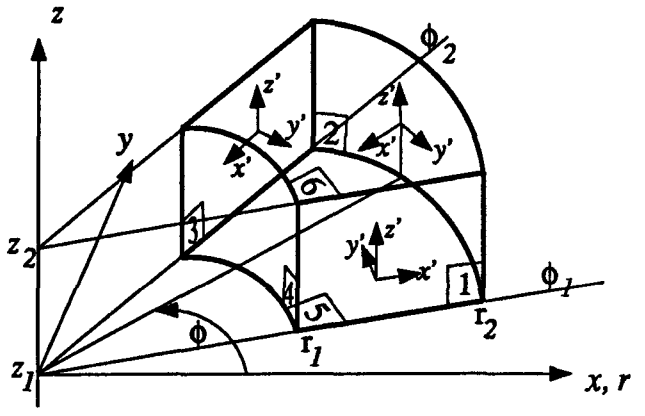

Figure 3.13 Cylindrical sector

3.5.1 Place of emission

The place of emission (P_e) can be determined by the linear interpolation technique between the coordinate boundaries using two random numbers. However, if coordinates r and ϕ are used to determine the emission place from walls *5* and *6*, the emission coordinates according to the Monte Carlo principle are given by:

$$\begin{aligned} r_e &= \sqrt{r_1^2 + (r_2^2 - r_1^2)R_3} \\ \phi_e &= \phi_1 + (\phi_2 - \phi_1)R_4 \\ z_e &= z_1 \veebar z_2 \end{aligned} \tag{3.38}$$

3.5.2 Direction of emission

The directional vector (**d**) of emission from a plane is given by the cone angle β and by the circumferential angle θ. The normal to surfaces *5* and *6* is parallel to the z axis. The direction of emission from surface *5* is given by:

$$\begin{aligned} d_x &= \sin\beta \ \cos\theta \\ d_y &= \sin\beta \ \sin\theta \\ d_z &= \cos\beta \end{aligned} \tag{3.39}$$

The emission from surface *6* takes place always in the negative z direction towards the interior of the enclosure, thus the sign of d_z is changed:

$$\begin{aligned} d_x &= \sin\beta \ \cos\theta \\ d_y &= \sin\beta \ \sin\theta \\ d_z &= -\cos\beta \end{aligned} \tag{3.40}$$

In the case of walls *1*, *2*, *3* and *4* a cartesian basis x',y',z' is placed on the wall with a coordinate axis parallel to the surface normal and pointing towards the interior of the enclosure, as being the result of a counterclockwise rotation of the x, y, z coordinate system around z (see Figure 3.13). The direction of the emission is first calculated relative to the x',y',z' basis resulting in vector $\mathbf{d}^*$, then these coordinates are expressed in terms of the x, y, z system giving the coordinates of $\mathbf{d}$. For wall *1* the coordinate basis is rotated by ϕ_1, for wall *3* by $\phi_2+\pi$, for wall *2* by ϕ, for wall *4* by $\phi+\pi$ in counterclockwise direction. The x, y and z components of directional vectors $\mathbf{d}$ and $\mathbf{d}^*$ are for wall 1:

$$\begin{aligned} d_x^* &= \sin\beta \ \cos\theta \\ d_y^* &= \cos\beta \\ d_z^* &= \sin\beta \ \sin\theta \\ d_x &= d_x^* \cos\phi_1 - d_y^* \sin\phi_1 \\ d_y &= d_x^* \sin\phi_1 + d_y^* \cos\phi_1 \\ d_z &= d_z^*, \end{aligned} \tag{3.41}$$

for wall *3*:

$$\begin{aligned} d_x^* &= \sin\beta\ \cos\theta \\ d_y^* &= \cos\beta \\ d_z^* &= \sin\beta\ \sin\theta \\ d_x &= d_x^* \cos(\phi_2+\pi) - d_y^* \sin(\phi_2+\pi) \\ d_y &= d_x^* \sin(\phi_2+\pi) + d_y^* \cos(\phi_2+\pi) \\ d_z &= d_z, \end{aligned} \tag{3.42}$$

for wall *2*:

$$\begin{aligned} d_x^* &= \cos\beta \\ d_y^* &= \sin\beta\ \cos\theta \\ d_z^* &= \sin\beta\ \sin\theta \\ d_x &= d_x^* \cos\phi - d_y^* \sin\phi \\ d_y &= d_x^* \sin\phi + d_y^* \cos\phi \\ d_z &= d_z^*, \end{aligned} \tag{3.43}$$

for wall *4*:

$$\begin{aligned} d_x^* &= \cos\beta \\ d_y^* &= \sin\beta\ \cos\theta \\ d_z^* &= \sin\beta\ \sin\theta \\ d_x &= d_x^* \cos(\phi+\pi) - d_y^* \sin(\phi+\pi) \\ d_y &= d_x^* \sin(\phi+\pi) + d_y^* \cos(\phi+\pi) \\ d_z &= d_z. \end{aligned} \tag{3.44}$$

3.5.3 Intersection calculation

The path of a ray is described by the equation of a line (3.20). The intersection point calculation of a line crossing planar walls is described in 3.4.2, and this applies for walls *1, 3, 5* and *6.*

The cylindrical surfaces *(2, 4)* are described by the equation of a cylinder whose axis is at the origin of the coordinate system:

$$x^2 + y^2 = r^2 \tag{3.45}$$

The coordinates of intersection point (P_i) are given by the solution of the set of equations consisting of (3.20) and (3.45). If the line crosses a cylindrical coordinate surface resulting in two intersection points, in ray tracing the intersection point is taken to be the one which is located at the shortest distance from the emission point.

3.5.4 Place of intersection

The walls in the cylindrical system are identified by surfaces defined by the cylindrical coordinate system. In order to decide whether the intersection point is inside the boundaries of a wall, the coordinates of the intersection point have to be converted to cylindrical coordinates, and compared to those of the boundary.

Since the cylindrical sector is a concave enclosure due to wall *4*, the procedure of identifying the wall on which the intersection point is located should always be started with wall *4*, which has a shading effect on the other walls from certain positions in the enclosure.

When emitting from planar walls, the emitting wall is not checked for intersection but in the case of wall *2* it has to be done due to its convex nature.

An assessment of the direct interchange area calculation obtained for cylindrical cases is given in Appendix B.

4

Application of the methods in different coordinate systems

The first step in a simulation using the zone, the imaginary planes (IPM) or the discrete transfer (DT) method, is to discretize the 3D radiation space into finite volumes and surfaces, which is called zoning. The zoning of the radiation space cannot be done arbitrarily, it requires some organization to enable the identification of the individual zones during the solution procedure. Furthermore, the discretization or zoning should conform to the geometrical boundaries of the radiation field.

The zoning arrangement is provided by a coordinate system. With the help of a cartesian, cylindrical or curvilinear coordinate system, a 3D grid can be generated to divide the radiation space into zones. The curves of a constant coordinate value are the grid lines, the intersection of which define the grid vertices. The grid vertices surround the individual zones which are separated by surfaces delimited by the vertices. In the grid the coordinates help the identification process necessary for the calculations.

In the following it will be explained how different coordinate systems can be applied to the radiation models to enable the treatment of complex geometrical configurations.

4.1 Cartesian coordinate system

Figure 4.1 shows the division of the enclosure into zones using the coordinate planes of the cartesian coordinate system. The surface zones are rectangles and the volume zones are rectangular parallelepipeds. The zones can be identified according to x, y and z directions with i, j and k positions.

The application of the cartesian coordinate system is restricted to rectangular parallelepiped-shaped enclosures, however by using "blocking" it can be extended to irregular shapes.

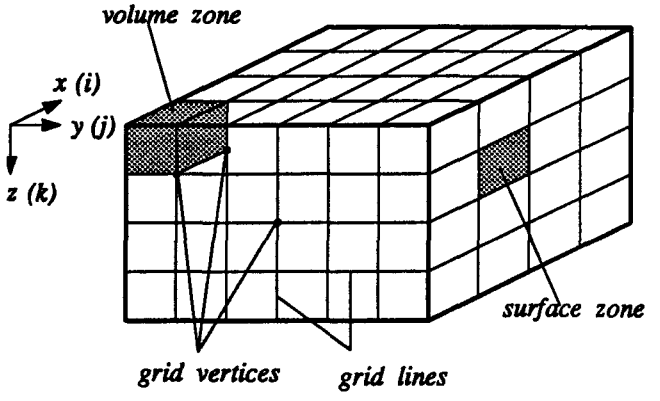

Figure 4.1 The use of the cartesian coordinate system for zoning

4.1.1 The use of blocking

The irregularly shaped enclosures can be placed in a cartesian grid. The zones lying outside of the enclosure boundary should be "blocked", i.e. they should be discarded from the calculation. Figure 4.2 illustrates the blocking approach for an irregularly shaped enclosure. The higher the number of divisions is, the more realistic the approach is in

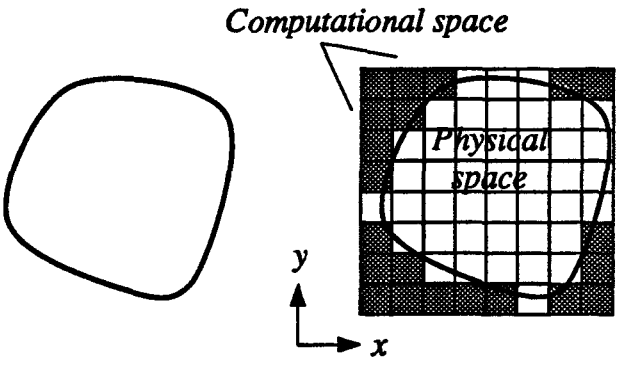

Figure 4.2 Example of blocking for a 2D enclosure

representing the real boundaries. However, the computer memory is used inefficiently when the blocking techniques are called for. The size of the variable arrays used for the computation is defined by the cartesian system enclosing the radiation space. The arrays also include the blocked regions although the computation has to be done only for the zones of the physical space.

The incorporation of blocking into the zone and DT methods concerns directly the ray tracing process. The zone and DT methods follow the rays across the zones. Every time a ray hits a wall surrounding a volume zone it is checked whether the wall is part of a real boundary. By using blocking, the walls of the blocked regions have to be declared as real walls and suitable radiative properties have to be assigned to them.

The IPM method can also incorporate the blocking technique. This method uses ray tracing locally in the individual zones, and the radiation space is interconnected with imaginary fluxes. The ray tracing for the direct interchange areas is not affected by the use of blocking but the equation containing the imaginary fluxes (equation 2.21) have to be modified. Equation (2.21) can be repeated in a more detailed form as:

$$\begin{bmatrix} \\ \mathbf{BM} \\ \\ \end{bmatrix} \begin{bmatrix} \mathbf{Q}_x \\ \mathbf{Q}_y \\ \mathbf{Q}_z \end{bmatrix} = [\mathbf{CM}] \tag{4.1}$$

The vector **Q** contains the x, y and z directional imaginary fluxes in the given order. By the use of blocking, the imaginary planes of the computational space can become real walls or part of the blocked region. The imaginary fluxes crossing these walls have to be removed from the **Q** vector; similarly the corresponding lines and columns should be removed from vector **CM** and matrix **BM** respectively. The set of equations can then be solved for the unknown imaginary fluxes (**Q**).

4.2 Cylindrical coordinate system

For cylindrical shapes the zoning can be carried out according to the cylindrical coordinate system (Figure 4.3). The zones are surrounded by planes of constant z coordinate perpendicular to the axis of rotation, planes of constant θ parallel to the z axis and concentric cylindrical surfaces. The ray tracing procedure of the zone and the DT methods has been developed for cylinders placed centrally in a polar coordinate system. The identification of the zones and the corresponding variable arrays are also arranged according to the cylindrical coordinates. In the case of IPM, the imaginary flux

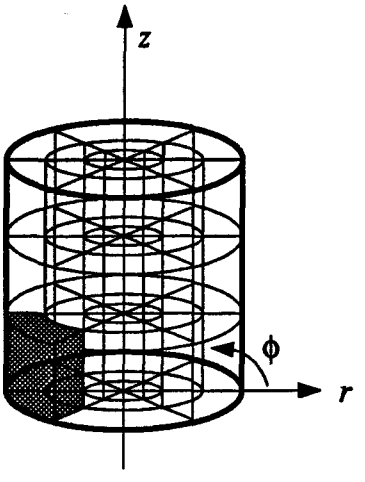

Figure 4.3 Zoning according to the cylindrical coordinate system

calculation algorithm developed for the cartesian coordinate system has been modified

for cylindrical case. A rectangular parallelepiped can be bent around the x axis until the left and right faces meet each other resulting in a cylinder as illustrated in Figure 4.4. After the bending process the surface zones on the left and right hand walls lose their real surface nature and become imaginary planes. At the axis of the cylinder the zones have only 5 surfaces instead of six as in the original cartesian coordinate system. In such cases the summation in equation (2.16) has to be done from $j=1$ to $j=5$

Zones can be blocked in the cylindrical grid system in the same way as it was done in the cartesian coordinate system.

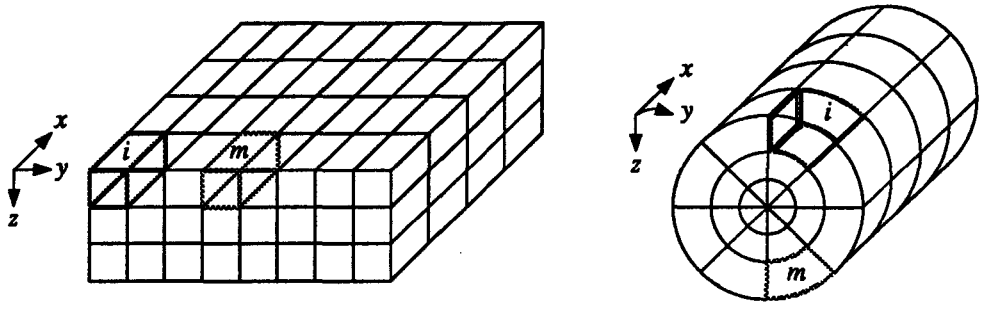

Figure 4.4 Application of the cartesian system to the cylindrical version of the IPM method

4.3 Curvilinear coordinate system

The use of curvilinear coordinate system for the grid generation enables the application of the zone, IPM and DT methods to a wide variety of complex 3D problems. None of the methods is restricted to orthogonal coordinate systems in their present form, so non-orthogonal coordinates can also be freely used.

The curvilinear grid is best imagined by supposing a regular cartesian grid placed in a jelly-like medium, which is then stretched, bent and twisted. All the zones which were originally in contact with one another remain so, but their shapes may have been changed considerably.

Curvilinear grid is frequently employed for the solution of fluid flow problems. In these cases, the physical field is divided by a curvilinear grid in the cartesian coordinate system but the partial differential equations describing the motion of the fluid are transformed and solved for a computational field which is always a regular rectangular grid in the curvilinear coordinate system.

In the case of radiation modelling, the physical space is divided into zones by the curvilinear grid. The ray tracing is performed in the curvilinear grid in the physical space. Once the geometry dependent part of the radiation models are solved, the rest of the calculation can be done in the same way as for the cartesian grid, since the arrangement and the identification functions of the curvilinear grid are the same way as those of the cartesian grid.

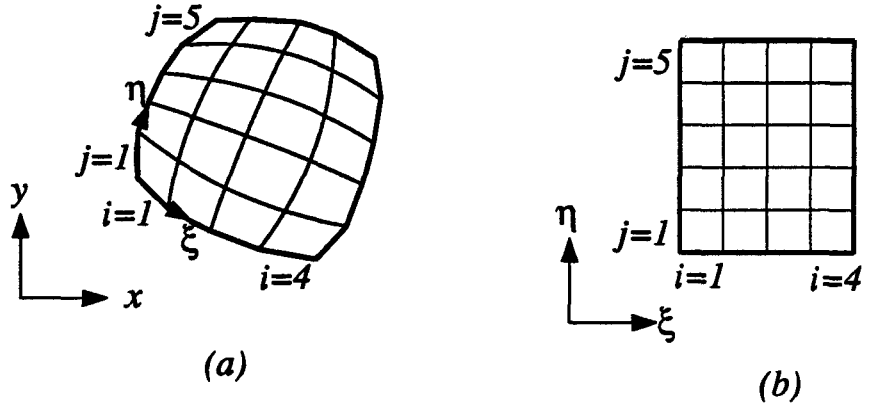

Figure 4.5 Application of the curvilinear grid to a 2D system and the corresponding cartesian grid

In the physical space the irregularly-shaped enclosure of Figure 4.2 is divided into zones using a curvilinear grid (ξ, η) in such a way that, on each boundary segment, a curvilinear coordinate of constant value is specified (see Figure 4.5a). In the curvilinear coordinate system (ξ, η) the boundary segments become a rectangle, and the grid becomes a rectangular grid (Figure 4.5b) similar to those used for the rectangular parallelepipeds.

The indexes (i, j, k) are used to identify the zones in the curvilinear coordinate system in a similar way as in the cartesian coordinate system.

The ray tracing techniques are described in the previous chapter for arbitrary hexahedral zones having planar surfaces. Unfortunately the eight corner points of a zone in a 3D curvilinear coordinate system define generally a volume element without planar surfaces. Therefore, the methods cannot work in real 3D curvilinear grids.

The above restriction can be overcome by the use of "pseudo curvilinear" grids. A 3D grid can be generated by the extension of a 2D curvilinear grid with a geometrical transformation. Such a transformation can be the translation of the 2D grid with small increments in the third coordinate direction (section 6.4) or the rotation of the grid around an axis (section 6.2) resulting in a third dimension for the grid points. In these cases, the requirement for hexahedral zones is fulfilled.

The radiation methods studied allow also the use of connected regions. Figure 4.6a illustrates a 2D connected region, which is opened up along the joint boundaries in the cartesian space on Figure 4.6b, and the corresponding rectangular grid in the curvilinear coordinate system is shown on Figure 4.6c. For the ray tracing algorithm of the zone and the DT methods, the zones on the connected boundary have to be identified as neighbors for the rays crossing the connected surface. The imaginary flux calculation of the IPM method permits also the use of connected regions. The imaginary fluxes will cross the connected surfaces and attention has to be paid to the identification of the neighboring zones.

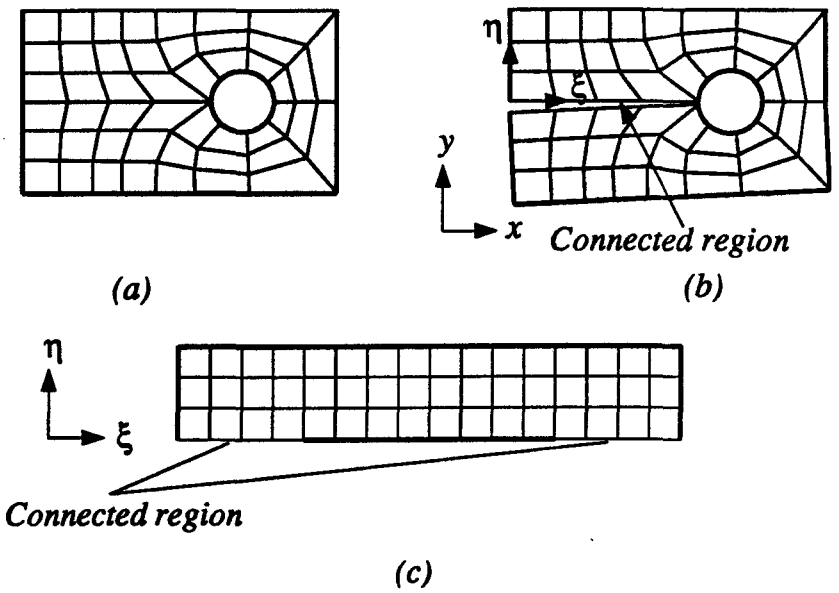

Figure 4.6 (a) Curvilinear grid with a connected region; (b) The curvilinear grid opened up at the connected region; (c) The corresponding rectangular grid.

Furthermore, obstacles placed in the radiation field can also be modelled as embedded regions. Figure 4.7a illustrates two circles as embedded regions in the 2D curvilinear grid of a rectangular enclosure in cartesian space. Figure 4.7b shows the enclosure in the curvilinear coordinate system, where the embedded regions appear as coordinate segments which have real boundaries. The surfaces of the embedded regions have to be treated as real surfaces.

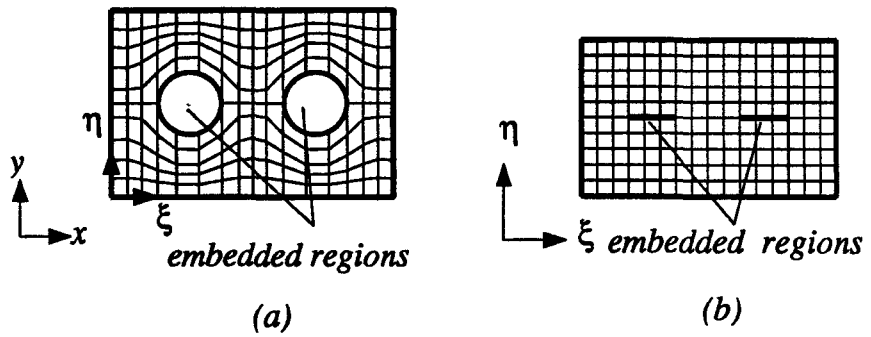

Figure 4.7 Curvilinear grid with embedded regions and the corresponding cartesian grid

The use of connected or embedded regions allows solving problems with obstructions in the radiation space as an alternative to the application of the blocking principle. At the same time, the use of blocking is also permitted while using curvilinear coordinates if required. The curvilinear grid generation technique is explained in detail by Thompson et al. (1985). For this work the curvilinear grid generating system of Wu (1990) has been used.

It should be noted that the cylindrical coordinate system can be regarded as a special case of the curvilinear system. By dividing a cylinder into a large number of divisions, the circumferential planes can be replaced by flat surfaces and the case can be taken as a connected curvilinear region.

5
Comparison of the methods

Mathematical models are generally defined as a set of algebraic or differential equations which may be used to represent or predict a certain phenomenon. The term *model* opposed to *law* implies that the relationships applied may not be quite exact and the final result may only be approximate. The zone, the imaginary planes (IPM) and the discrete transfer (DT) methods model thermal radiation phenomena differently as explained in chapter 2, but their solutions are assumed to approximate to some (unknown) extent the real solution of the physical problem.

The intention here is to use the radiation models in 3D enclosures, where analytical solutions or exact solution for radiation problems do not exist. On the other hand the literature on radiation modelling recognizes the zone method as one of the most accurate numerical methods available. It is frequently used as reference when testing new models. In this chapter, solutions to 3D test problems with IPM and the DT methods will be compared with the solution given by the zone method.

5.1 Accuracy of the zone method

When solving a radiation problem by the zone method, the resulting heat flux distribution will be strongly influenced by the discretization of the continuous domain into finite volumes and surfaces.

The total-interchange areas are calculated by the Monte Carlo technique, since it can be applied to enclosures with irregular as well as regular geometries. The use of Monte Carlo technique introduces a statistical error into the calculation. The effect of this type of error can be estimated by using different random sequences. The fluctuation of the resulting fluxes around a mean value ranges from 1 to 5%. This fluctuating error can be responsible for local maximum discrepancies, but is cancelled when average values are computed over the whole field.

5.2 The bases of comparison

The IPM and DT methods were compared with the zone method on the basis of heat flux and volumetric source term distributions and the computation (CPU) time. The variable parameters of the comparison were the radiative properties and the number of divisions in the enclosure. The tests were conducted in rectangular and cylindrical 3D enclosures. In gray systems the radiative properties to be specified are the emissivity of the surfaces and the absorption coefficient of the gas.

5.3 Comparison in a rectangular parallelepiped

The rectangular parallelepiped has been selected in such a way that the radiation process would not prevail in any direction and the radiation heat transfer would be three dimensional. The dimensions and the surface identification of the chosen parallelepiped are shown in Figure 5.1.

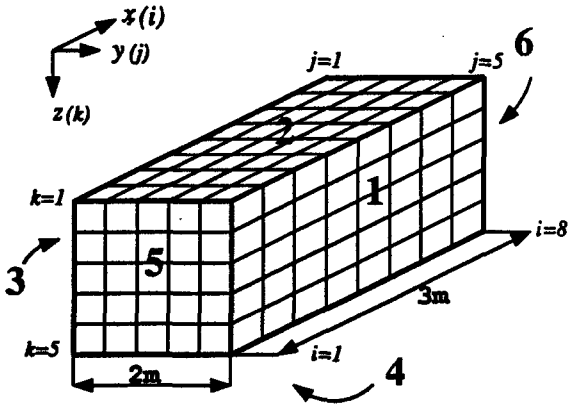

Figure 5.1 Rectangular parallelepiped test enclosure

5.3.1 *Effect of radiative property variation*

The comparison is carried out with constant number of divisions and with variable surface emissivity and gas absorption coefficient. The input data are given in Table 5.1.

Table 5.1 Input data for the test in cartesian coordinates

Dimensions x, y, z	3m x 2m x 2m
Divisions	8 x 5 x 5
Temperatures	
faces 1, 3	300 °C
faces 2, 4	500 °C
faces 5, 6	400 °C
gas	1300 °C
Emissivities	
uniform on every surface	0.2, 0.5, 0.8, 1.0 (variable)
Absorption coefficient	
uniform	0.01, 0.05, 0.1, 0.25, 0.5, 1.0, 2.0 1/m (variable)

The chosen values of the emissivity are representative of a highly reflective surface, the surface of a metal bath, a strongly absorbing wall and a black body, respectively. The gas absorption coefficient varies within a very large range from transparent to strongly absorbing gas, including three values that are frequently used (0.05, 0.1, 0.25). Taking into account the size of the zones and the values of the gas absorption coefficient, the optical thickness varies roughly between 0.005 and 1.0.

The size of the rectangular parallelepiped was selected to conform to 3D enclosures found in industry. The given geometrical configuration has 200 volume zones and 210 surface zones. Including all the variations for the radiation parameters 27 different cases are treated with three different methods.

The total-interchange areas (TIA) of the zone method were calculated by the Monte Carlo technique by emitting 6000 rays from each volume and surface zone. It has been noticed from experience that, in case of simple geometrical configuration (parallelepiped with uniform zoning), the TIA values are fluctuating around a mean value if more than 5000 rays are used.

The direct interchange areas (DIA) of the IPM method were calculated with 10000 emitted rays. The application of 6000 rays would have been sufficient here too, but, since the computation was done for only one set of DIAs within a single zone, the use of a high number of rays was affordable.

The accuracy of the discrete transfer method is dependent on the number of divisions of the hemisphere over the emitting and absorbing surfaces. The comparison was done for 36, 100, 400, and 900 divisions, so that accuracy could be estimated according to the solid angle divisions as well. The discrete transfer method used with different solid angle divisions will often be referred to by DT36, DT100, DT400, DT900.

In this particular problem uniform gas temperatures and absorption coefficient have been used. The DT and the zone methods could treat this problem with only one zone for the entire gas volume keeping the surface divisions. However, the calculation was made with the given zone sizing, in order to use the method in the same way as in case of more difficult problems.

Because of the extensive number of results, the values obtained with the three methods are not reported at every location. Profiles are given at specific locations. Average relative differences (ARD, VRD) are computed for the whole field and maximum relative differences (MRD) allow the identification of the most erroneous results.

Average relative differences The heat fluxes obtained with the IPM and DT methods are compared to the heat fluxes predicted by the zone method for every surface zone. The absolute value of the relative difference between the surface flux obtained with IPM or DT and that obtained with the zone method is formed for every surface zone. Then, the relative differences are summed over all the surfaces and are divided by the number of the surface zones (*ns*) to give an average relative difference

$$average\ relative\ difference = \frac{1}{ns}\sum_{i=1}^{ns}\left|\frac{DT/IPM\ flux_i - ZONE\ flux_i}{ZONE\ flux_i}\right| \quad (5.1)$$

(ARD)

The average relative difference value is used to characterize the accuracy of the method for a given wall emissivity and gas optical thickness. The formulation of the average relative difference does not permit zero flux values for the zone method. The possibility of zero flux for any method is very small but attention has to be paid to the near zero flux values. For example, if the zone method gives a heat flux of 0.1 kW/m^2 at a specific location, while the IPM result is 1.0 kW/m^2, the resulting relative difference in the flux values is 900%. In fact this difference in the flux values does not affect the overall performance of the method, since in radiation heat transfer generally high flux values are considered. For the accuracy evaluation, the fluxes close to zero should therefore be excluded. In Figures 5.2, 5.3, 5.4, 5.5 the heat flux distributions obtained with IPM and DT methods (100 solid angle divisions) are compared with those provided by the zone

method. For *K=0.01*, the radiative fluxes are very close to zero, therefore this case was excluded completely during the evaluation of the methods for accuracy.

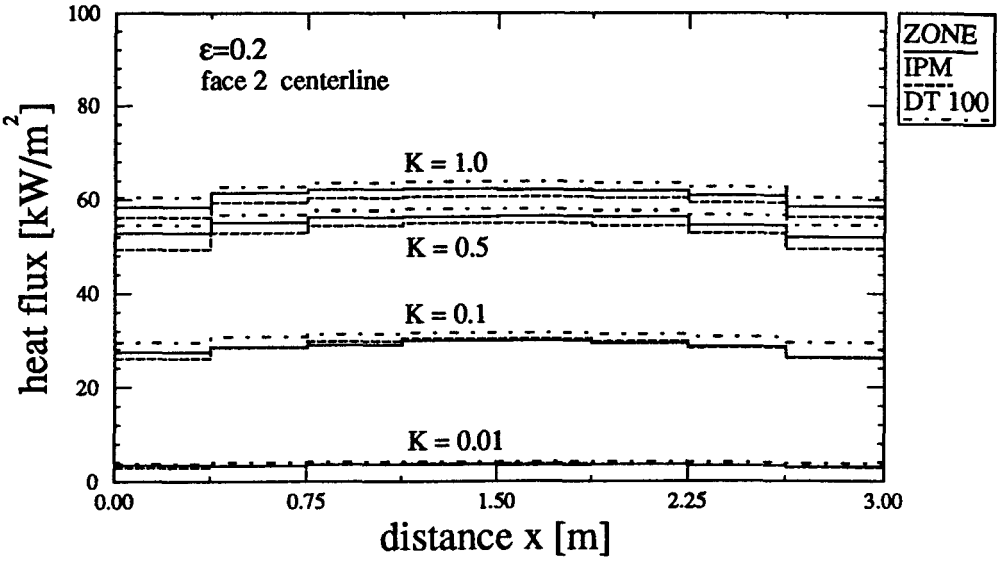

Figure 5.2 Heat flux distribution on the x direction centerline on face 2, ϵ=0.2

The heat flux distribution on face 2 along the x direction centerline is shown on Figure 5.2 for a low surface emissivity case (ϵ=*0.2*). The heat flux distribution along the same line but with ϵ=*0.8* is given on Figure 5.3. In both cases the heat fluxes for *K=0.01* are very close to zero.

Figures 5.4 and 5.5 show the heat flux distribution along the lower portion of face 1 with surface emissivities 0.2 and 0.8 respectively. In this region, it is seen that the discrepancies between the distributions predicted by the three methods are somewhat higher than along the centerline. In the case of zone method, the effect of the statistical

errors on the heat flux distribution —due to the Monte Carlo technique— is well detectable and the error is somewhat higher than that along the centerline.

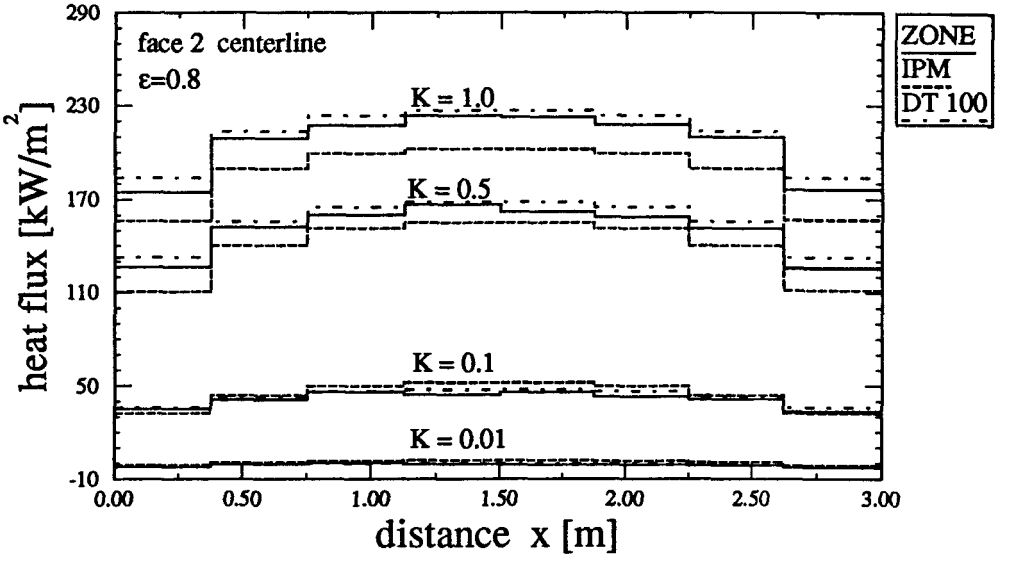

Figure 5.3 Heat flux distribution on the x direction centerline on face 2, ϵ=0.8

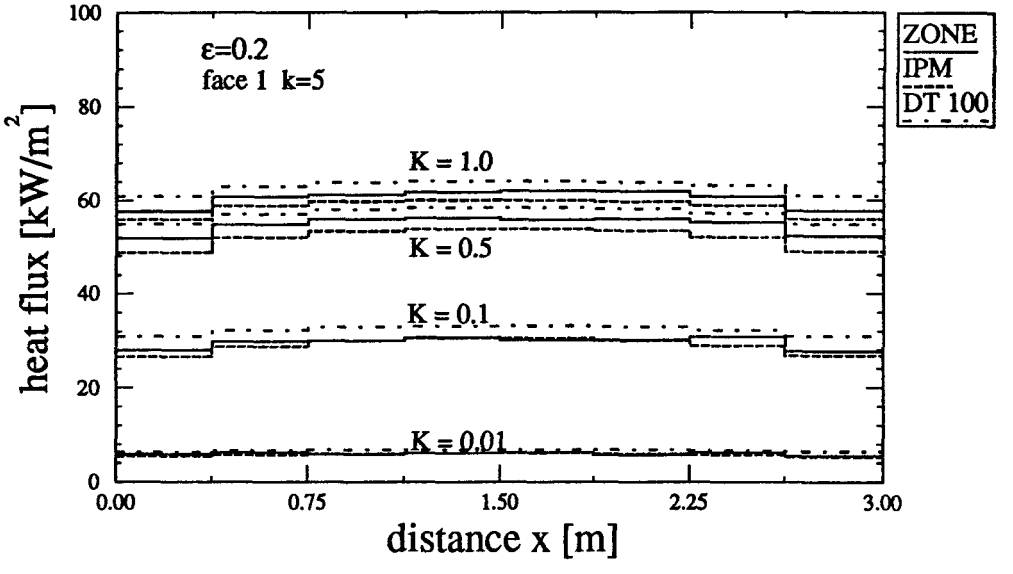

Figure 5.4 Heat flux distribution at k=5 on face 1 ϵ=0.2

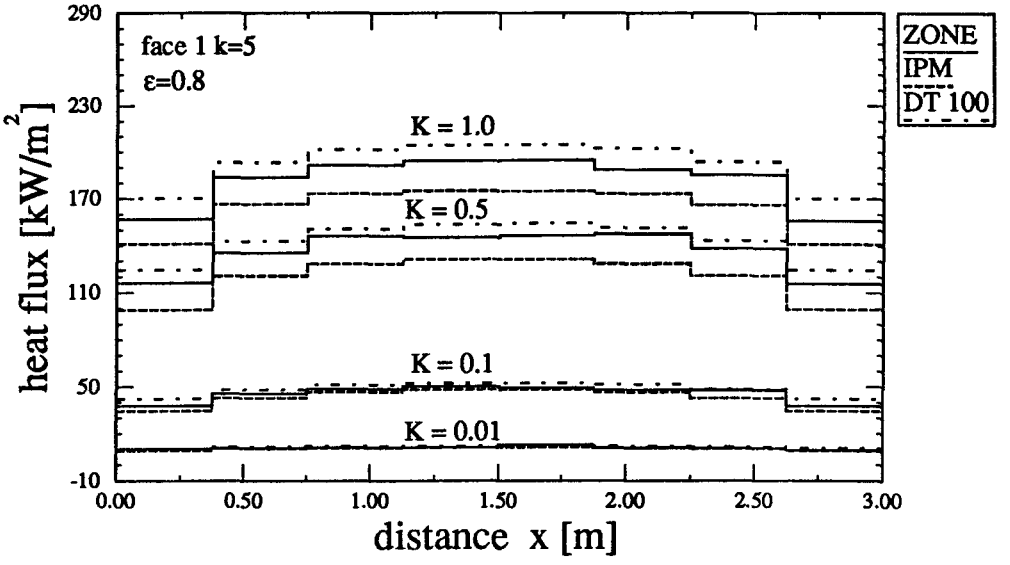

Figure 5.5 Heat flux distribution at k=5 on face 1 ϵ=0.8

The average relative differences (ARD) between the IPM or DT and the zone method solution are given in a bar graph format on Figures 5.6 to 5.9, the ARD calculated here over all the surface zones. The accuracy of the IPM method (Figure 5.6) seems to depend strongly on the wall emissivity. In the case of black walls the relative difference can be 2–3 times higher than for a 0.2 emissivity. The ARD is maximum in the gas absorptivity range 0.5 — 1.0. It varies from 3% to 10% when the black wall case is discarded from the examination.

The accuracy of the discrete transfer solutions increases rapidly with the number of divisions of the hemisphere. For the high emissivity cases (0.8, 1) the application of 36 divisions yields ARD values lower than 10% over the whole gas absorption coefficient range. If 100 solid angle divisions are used, ARD is between 5 and 10% for K=0.05 and 0.1, and around 5% for higher values of K depending slightly on the wall emissivity.

With increasing number of solid angle divisions ARD decreases to less than 5% (Figure 5.9). For this simple radiation problem the accuracy is practically unchanged for more than 400 solid angle divisions.

It is necessary to emphasize that for complex geometrical configurations, with non-uniform zone sizes, more solid angle divisions may be necessary to obtain the same accuracy. Examples of such geometrical configurations will be presented in the following chapter.

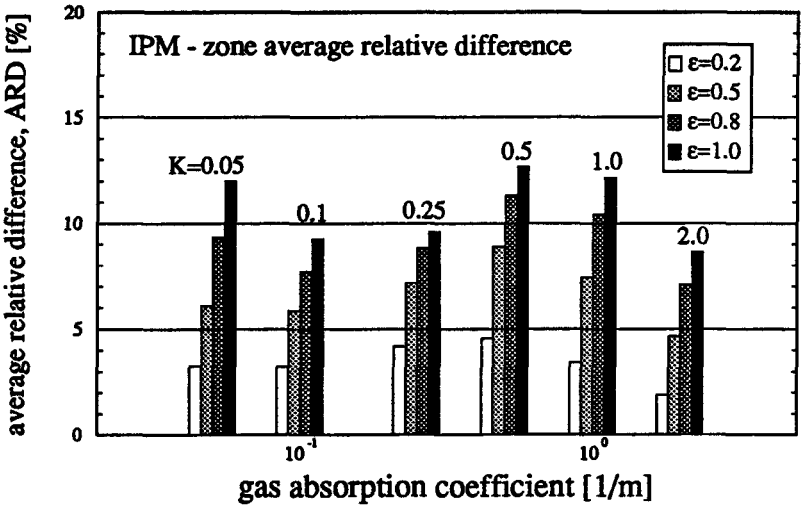

Figure 5.6 Average relative difference of surface heat flux between IPM and zone method with respect to surface emissivity and gas absorption coefficient

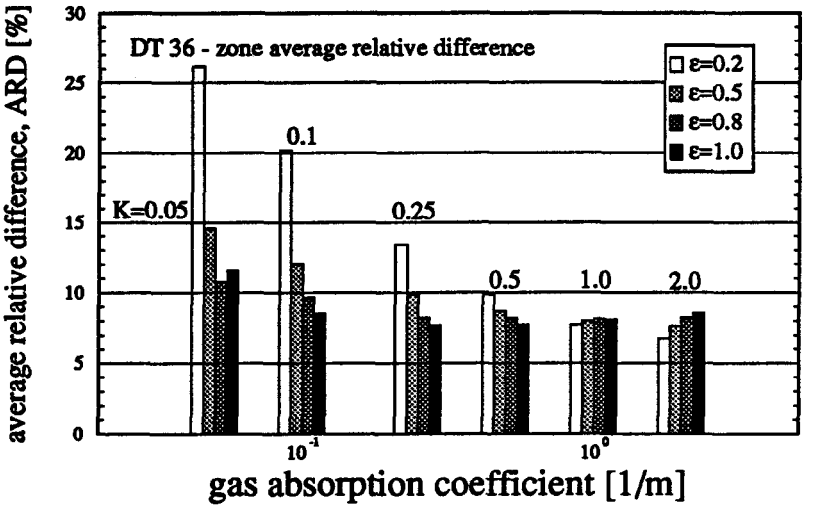

Figure 5.7 Average relative difference of surface heat flux between DT (36 solid angle divisions) and zone method with respect to surface emissivity and gas absorption coefficient

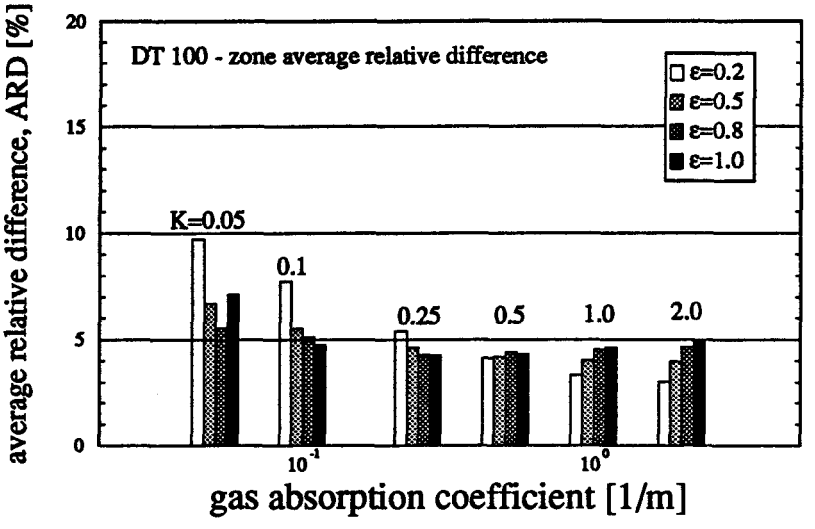

Figure 5.8 Average relative difference of surface heat flux between DT (100 solid angle divisions) and zone method with respect to surface emissivity and gas absorption coefficient

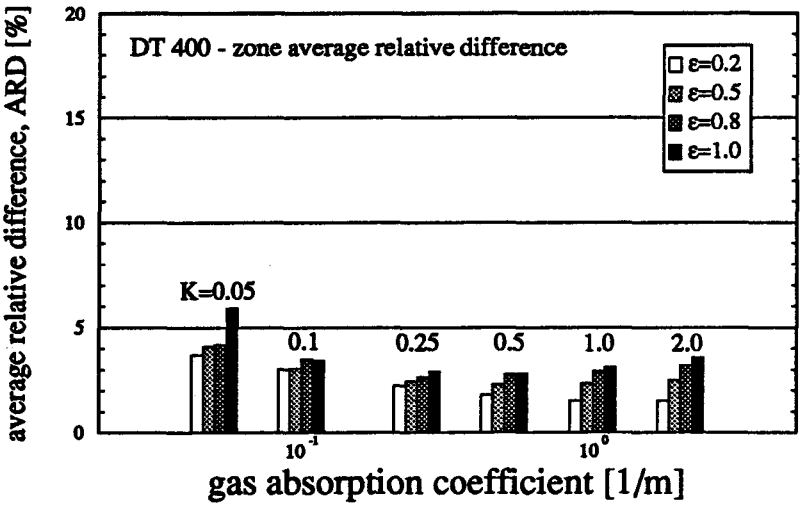

Figure 5.9 Average relative difference of surface heat flux between DT (400 solid angle divisions) and zone method with respect to surface emissivity and gas absorption coefficient

Maximum relative differences The use of average relative differences gives a good indication of the overall accuracy, but it is also necessary to examine to what extent the individual heat fluxes differ from those of the zone method. For this purpose, the maximum relative differences have been formed:

$$maximum\ relative\ difference = \max \left| \frac{DT/IPM\ flux_i - ZONE\ flux_i}{ZONE\ flux_i} \right| \quad (5.2)$$

(MRD)

Attention has to be paid here to the stochastic nature of total interchange area calculation. In the case of ARD, the random fluctuations of the zone flux values are smoothed by the average formulation, but in MRD attention is focused on the most inaccurate flux value. Figure 5.10 displays the maximum relative differences for the IPM method. For *K=0.05* and black walls, the maximum relative difference values can reach 40 — 50%. This location is on surface *4* at *i=4, j=2*. Figure 5.11 shows the *y* direction

heat flux distribution for $i=4$ on surface 4 and the maximum error location marked by arrows. Obviously a large stochastic error is added to the existing relative difference value. In Figure 5.12 the lower curve shows the x direction flux distribution for $j=2$ on the same surface, while the upper curve shows the heat flux distribution on face 2 at $j=5$ for $K=0.1$, $\epsilon=1.0$ through the maximum relative difference location. In the latter case the maximum error is strictly due to the IPM inaccuracy.

The maximum relative differences of the DT method using 100 solid angle divisions is shown on Figure 5.13. The stochastic nature of the zone method can be expected to have the same influence on the results here, as for the IPM method. The maximum difference is increasing with increasing surface emissivity, and decreasing with increasing absorption coefficient. In case $K=0.05$, the maximum differences are between 20–30%, while for higher absorption coefficients they decrease to 8–15%.

For 400 solid angle divisions, the distribution of the maximum differences has a similar trend, but the values are 3–5% lower than those obtained by 100 solid angle divisions. If the number of solid angle divisions is increased to 900, the MRD stay practically at the 400 division range (5–20%).

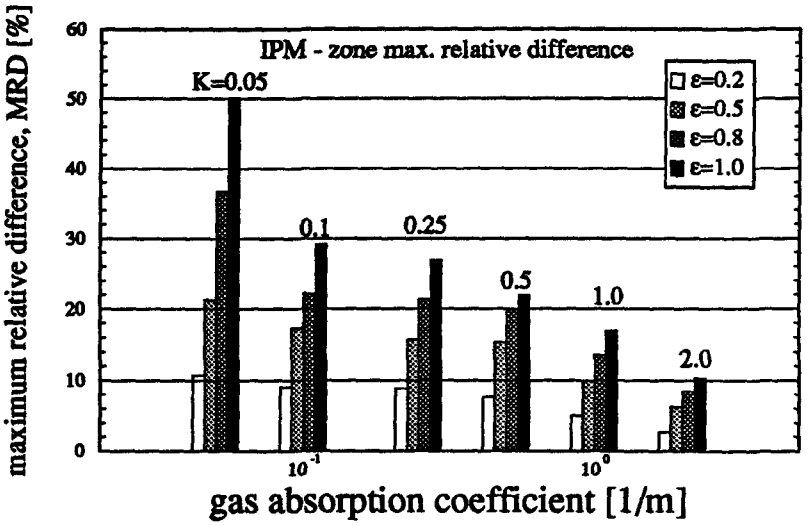

Figure 5.10 Maximum relative difference of surface heat flux between IPM and zone method with respect to surface emissivity and gas absorption coefficient

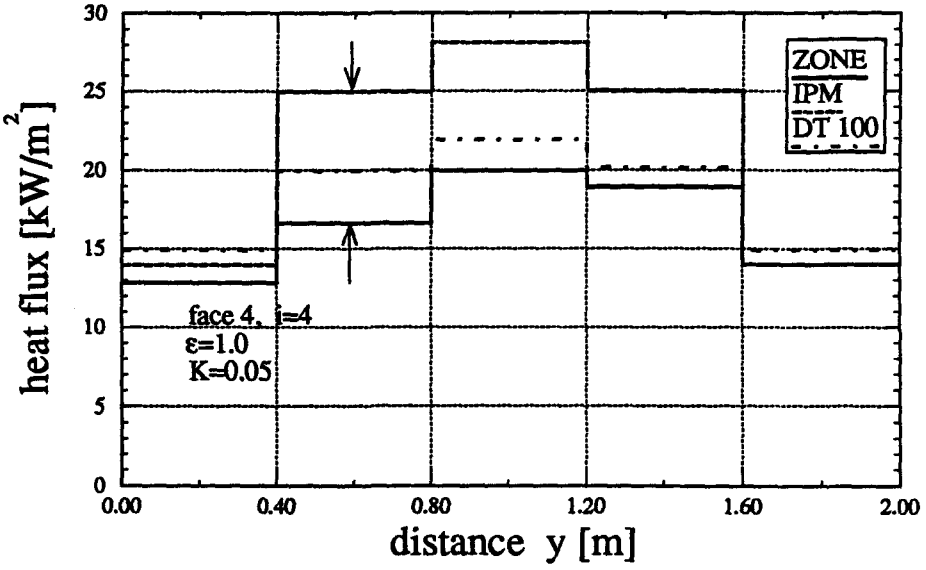

Figure 5.11 Heat flux distribution at i=4 on face 4 ϵ=1.0 (Maximum error location marked by arrows)

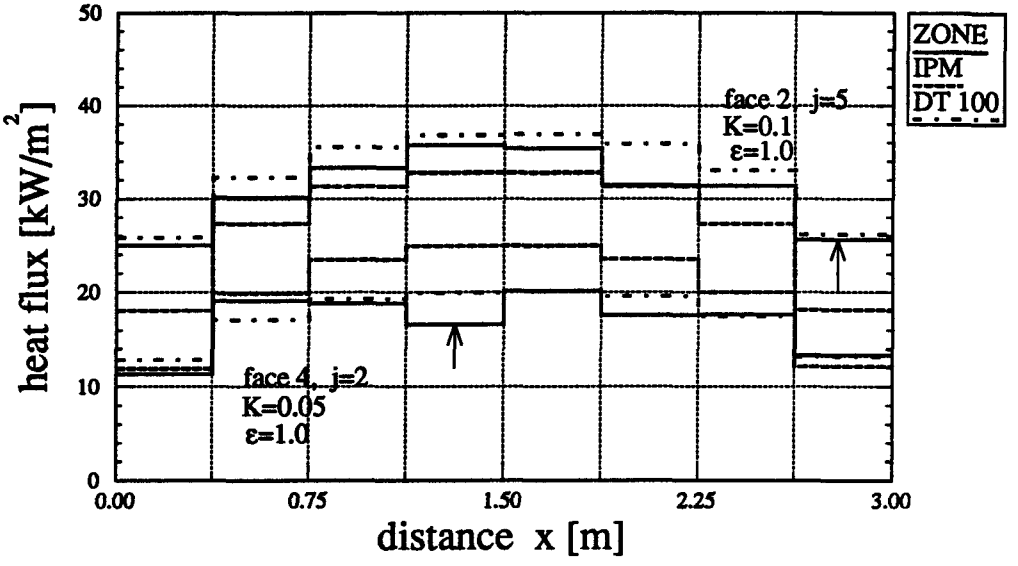

Figure 5.12 Heat flux distribution at j=2 on face 4 ϵ=1.0 (Maximum error location marked by arrows)

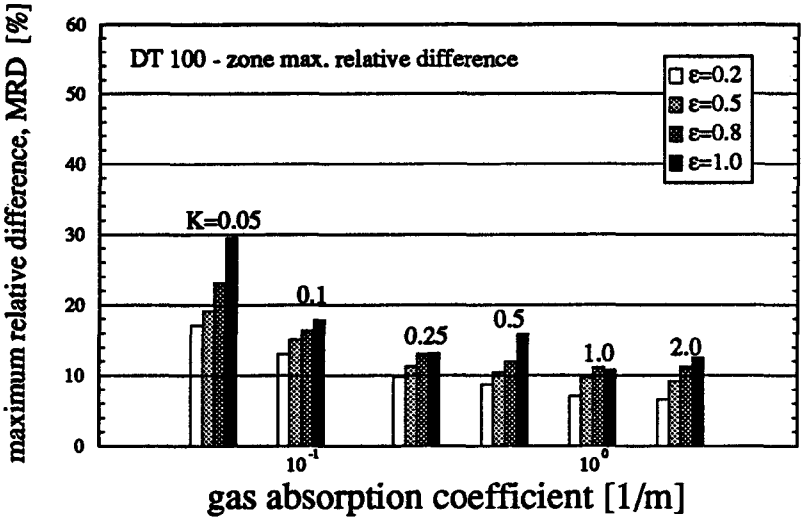

Figure 5.13 Maximum relative difference of surface heat flux between DT (100 solid angle divisions) and zone method with respect to surface emissivity and gas absorption coefficient

Volumetric radiative source terms The volumetric radiative source terms of the IPM and discrete transfer methods can be compared to those of the zone method in a manner

similar to the formulation of the ARD values in (5.1). The volumetric source terms are given by equation (2.6) for the zone method, by equation (2.23) for the IPM and by equation (2.29) for the DT method. Note that equation (2.29) gives only the contribution of a single ray crossing the given zone and that the complete source term is obtained by summing the contributions of all the rays crossing the zone. The absolute value of the relative difference between the volumetric source terms obtained with IPM and DT method and that obtained with the zone method is determined for every volume zone. Then, the relative differences are summed over all the volumes and are divided by the number of volume zones (nv) to find the average relative difference for the volumetric sources (VRD):

$$\begin{matrix} \textit{average relative difference} \\ \textit{of the volumetric radiative} \\ \textit{source } (VRD) \end{matrix} = \frac{1}{nv} \sum_{i=1}^{nv} \left| \frac{DT/IPM \ vol.source_i - ZONE \ vol.source_i}{ZONE \ vol.source_i} \right| \qquad (5.3)$$

The VRD values of the IPM and of the DT method with 100 solid angle divisions are given on Figures 5.14 and 5.15 respectively. In the case of the IPM the VRD values are under 5% for the absorption coefficients 0.01, 0.05 and 0.1. For higher absorption coefficients (0.5, 1.0, 2.0) the VRDs are over 10 % but they never exceed 15%.

The DT method is evaluated only for 100 solid angle divisions. The VRD values stay under 5% for all the absorption coefficients except for the highest one (K=2.0), where it is 6–7%.

The volumetric source terms are in good agreement with the values of the zone method for both simplified methods, but it has to be kept in mind that the temperature and the absorption coefficient within the gas volume were taken to be uniform.

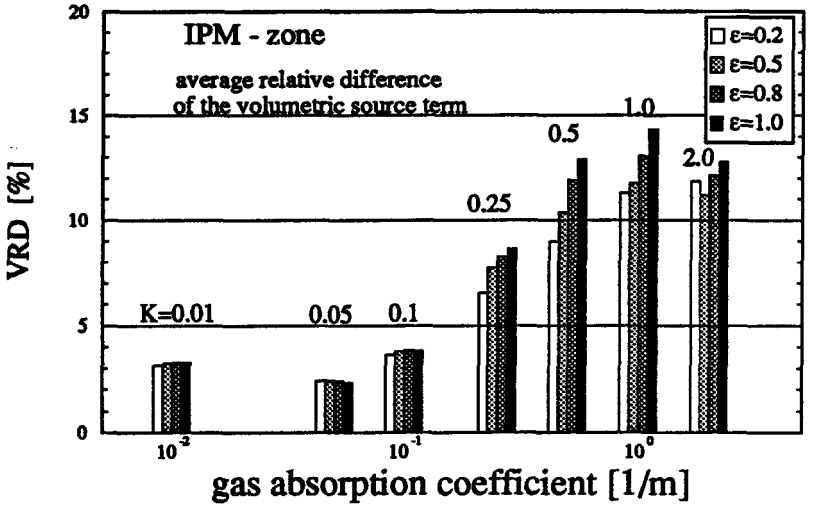

Figure 5.14 Average relative difference of volumetric radiative source term between IPM and zone method with respect to surface emissivity and gas absorption coefficient

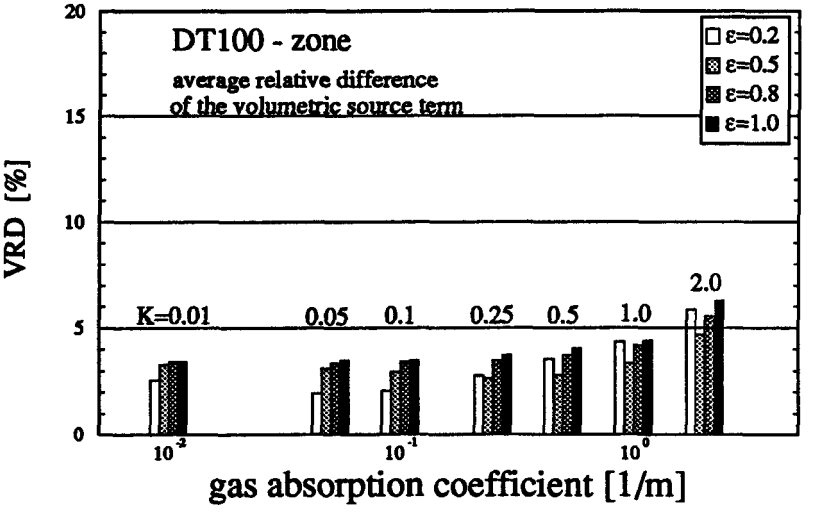

Figure 5.15 Average relative difference of volumetric radiative source term between DT (100 solid angle divisions) and zone method with respect to surface emissivity and gas absorption coefficient

Computation time The total interchange area computation of the Monte Carlo technique takes 95 % of the computation time of the zone method. The calculation time

increases with decreasing surface emissivity, but it is most influenced by the gas absorption coefficient. The lower the surface emissivity or the gas absorption coefficient is, the lower the possibility is for a ray to be absorbed by the wall or by the gas. Consequently the ray has to be followed for a longer period.

If the boundary surfaces are not black, the discrete transfer method calculates iteratively. The calculation time depends mostly on the number of iteration steps necessary for the solution.

The IPM method computing time is independent of the radiative properties. The direct interchange areas have to be calculated only once, provided that the zoning and the properties are uniform. Table 5.2 displays the CPU times of the different methods with respect to K for $\epsilon=0.2$. In Table 5.3 the CPU times are given with respect to ϵ for $K=0.25$.

In the previous section the DT method proved to be very accurate in the case of high (400, 900) number of solid angle divisions. Table 5.2 and 5.3 show that the increase in accuracy of the DT method is very costly in terms of computation time.

Table 5.2 CPU times of zone, IPM and DT methods at ϵ=0.2 with respect to K (Computer: SGI 4D/340)

		CPU time [s]					
ϵ	K	zone	DT 36	DT 100	DT 400	DT 900	IPM
0.2	0.01	11780	187	565	1756	3725	40
	0.05	9415	165	513	1584	3535	
	0.1	7497	135	436	1336	2977	
	0.25	4835	98	308	996	2233	
	0.5	3234	67	214	747	1673	
	1.0	2110	52	148	582	1301	
	2.0	1327	37	124	415	929	

The speed of calculation for the DT method is comparable with that of the IPM only for the 36 solid angle division case, for both of which the accuracies are similar. In the case of higher solid angle divisions the calculation time of the DT method becomes one or

two orders of magnitude higher than that of the IPM. With 900 solid angle divisions the calculation time of DT method is already comparable (in the same order of magnitude) to the calculation time of the zone method.

Table 5.3 CPU times of zone, IPM and DT methods at K=0.25 with respect to ϵ (Computer: SGI 4D/340)

		CPU time [s]					
ϵ	K	zone	DT 36	DT 100	DT 400	DT 900	IPM
0.2	0.25	4835	98	308	996	2233	40
0.5		3315	60	205	665	1301	
0.8		2432	38	128	416	929	
1.0		2060	15	51	167	372	

The ordinate axis of Figures 5.16 and 5.17 is the ratio of the CPU time of the zone method over the CPU times of the IPM or DT method, the latter with different number of solid angle divisions. These values are plotted against wall emissivity and gas absorption coefficient on Figures 5.16 and 5.17, respectively. In other words Figures 5.16 and 5.17 show how many times faster the IPM or the DT method solves the test problem compared to the zone method, with wall emissivity and gas absorption coefficient being varied.

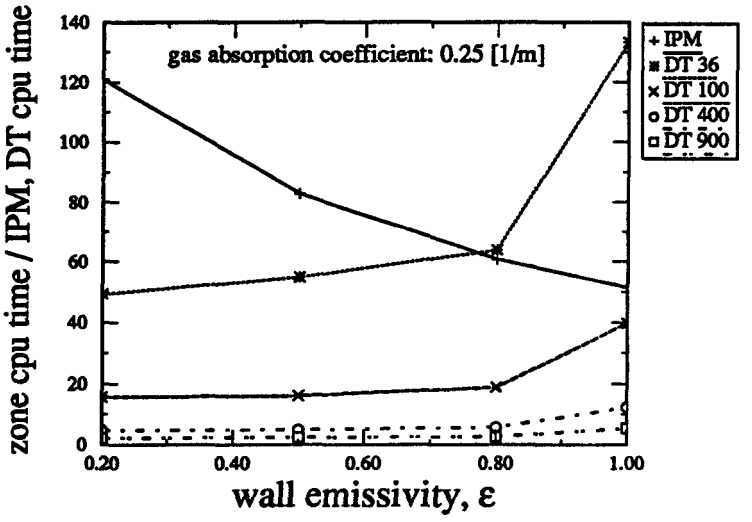

Figure 5.16 Relative speed of the IPM and DT methods compared to the zone method with respect to ϵ, at K=0.25

The IPM method, depending on the radiative properties, was found to be 50–120 times faster than the zone method. If DT method with 100 solid angle divisions is used in which case the ARD is near 5 %, DT method is about 20 times faster than the zone method.

With increasing gas absorption coefficient the calculation time of the zone method is rapidly decreasing, which is illustrated by the strong negative slopes on Figure 5.17. The computations were done on a 33 Mhz CPU of a Silicon Graphics 4D/340 workstation.

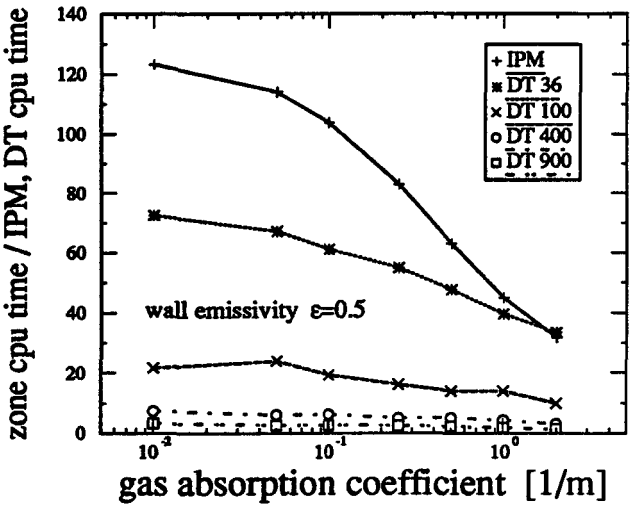

Figure 5.17 Relative speed of the IPM and DT methods compared to the zone method with respect to K, at ϵ=0.5

5.3.2 *Effect of increasing the number of divisions*

So far in the given enclosure the influence of radiative properties on accuracy and computation time have been analyzed for constant temperatures and zone sizes. Now the radiative properties will be fixed, and the effect of increasing the number of divisions will be examined. The gas absorption coefficient K and the surface emissivity ϵ are set to 0.5 [1/m] and 0.8, respectively. Similarly to the previous section, the relative differences are formed in order to compare the IPM and DT methods with the zone method. This time the minimum relative differences are also introduced, which prove to be useful to evaluate the behavior of the IPM. These are also defined by equation (5.2). They were not used before because they are not influenced much by variations of radiative properties.

For this comparison, the number of solid angle divisions of the DT method were kept at 100. Table 5.4 contains all the statistical data obtained by comparing the IPM

and the DT methods with the zone method. Figure 5.18 illustrates more clearly the first column of this table.

Table 5.4 Summary of the comparison of IPM and DT methods (100 solid angle divisions) to the zone method as a function of increasing number of spatial divisions

Divisions	Average relative diff [%]		Maximum relative diff [%]		Minimum relative diff [%]		Cpu time [s]		# of surf. zones
	IPM	DT	IPM	DT	IPM	DT	IPM	DT	
5 x 3 x 3	5.7	7.0	10.0	12.5	1.6	2.4	30	30	78
8 x 5 x 5	11.3	4.4	19.9	11.9	1.8	0.2	35	128	210
12 x 7 x 7	15.5	3.4	29.2	11.9	6.4	0.06	40	326	434
16 x 10 x 10	20.2	3.0	38.0	13.6	10.0	0.02	45	1024	840

The IPM method is a simplification of the zone method. If the enclosure is divided into one zone, the IPM method is equivalent to the zone method, and the ARD is zero. By using more and more divisions the IPM method loses accuracy as it is clearly indicated by the average relative differences. The computation time increases only very slightly with the increasing number of zones, which is due to the iterative solution technique of the linear equations containing the imaginary fluxes. The minimum and maximum relative differences increase in the same proportion as the average relative difference, meaning that the IPM flux distribution is uniformly moving away from the zone flux distribution and that the increase in discrepancy is not due to local effects. Hence the IPM method is not suggested to be used in case of high number of zonal divisions. Despite this weakness, the IPM method is useful in many practical systems, as described in section 5.5.

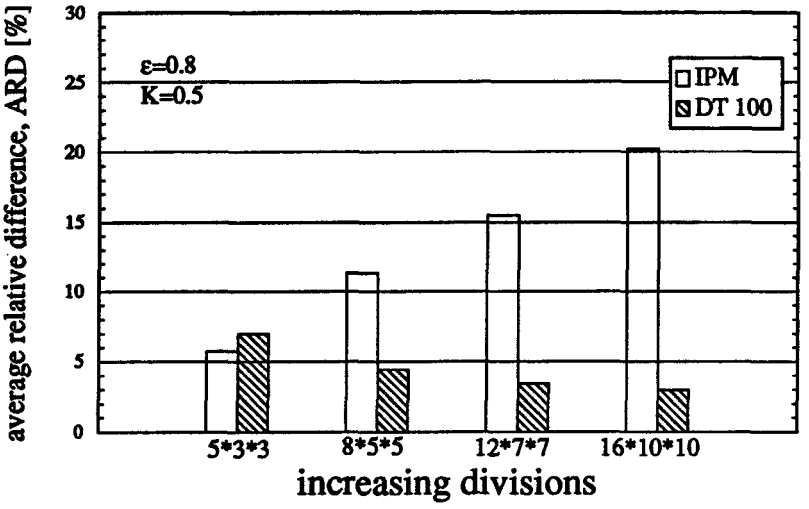

Figure 5.18 Variation of the ARD with increasing number of spatial divisions (first column of Table 5.4)

The DT method behaves oppositely to the IPM method. By increasing the number of divisions, the ARD decreases. However the MRD stays constant, and this can be explained by the fact that the number of solid angle divisions were kept unchanged. The computation time of the DT method is strongly dependent on the number of divisions used. If the divisions in x, y and z directions are multiplied by a factor r_x, r_y and r_z, respectively, the calculation time can be multiplied by the product of $r_x \cdot r_y \cdot r_z$ keeping all the other conditions constant. This approximate relation is also valid for the zone method, but it is also influenced by the gas absorption coefficient slightly since the rays can be absorbed along their path, while in case of the DT method the rays have to be followed until hitting a boundary. The DT solution is getting very close to the zone method solution in case of large number of divisions, but the computing time is still rather high.

5.4 Comparison in a cylindrical enclosure

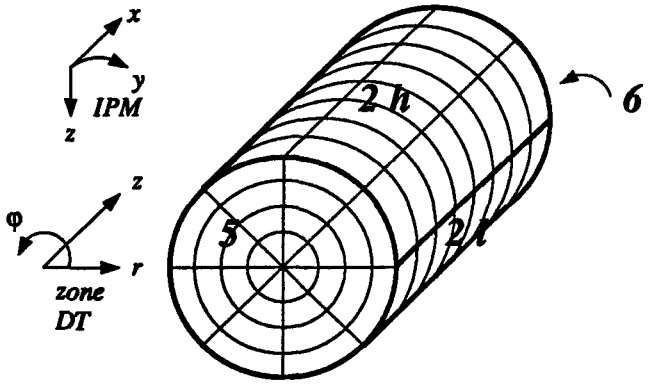

Figure 5.19 Cylindrical test enclosure

Table 5.5 Input data for the test in cylindrical coordinates

Dimensions	dia: 2 m, length: 3 m
Divisions	8 x 8 x 4 (x,y,z - z, ϕ,r)
Temperatures	
face 2 l	400 °C
face 2 h	600 °C
face 5	300 °C
face 6	500 °C
gas	1300 °C
Emissivities	
uniform on every face	0.2, 0.5, 0.8, 1.0 (variable)
Absorption coefficient	
uniform	0.01, 0.05, 0.1, 0.25, 0.5, 1.0, 2.0 1/m (variable)

In this case, unlike the tests in the rectangular enclosure, the results show flux values close to zero not only at K=0.01 but also at K=0.05. In the rectangular case, due to these small values, the relative difference values at K=0.01 were not presented. Here the flux values lying in the interval [−5, 5] kW/m^2 are excluded from the statistics. The overall number of real surfaces is 128. However at ϵ=0.2 and K=0.01 only 69 flux values are included in the statistics, and only 83 at ϵ=0.5, K=0.01.

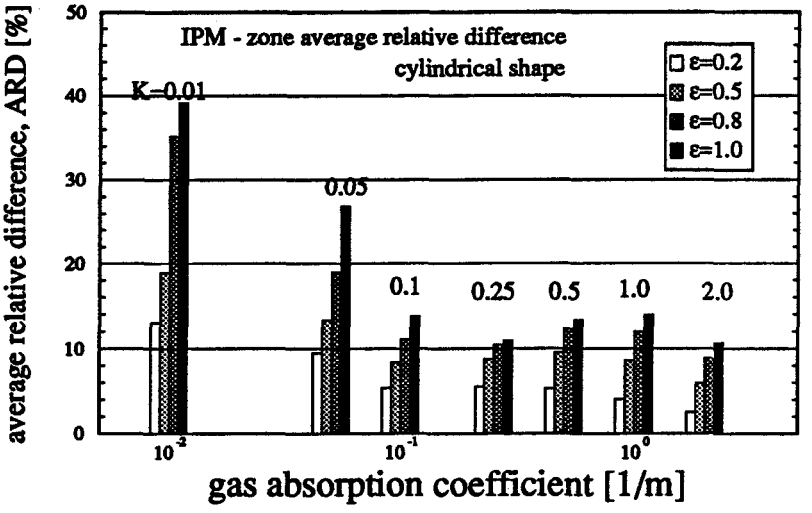

Figure 5.20 Average relative difference of surface heat flux between IPM and zone method with respect to surface emissivity and gas absorption coefficient for the cylindrical case. Heat fluxes lying in the interval [−5, 5] kW/m^2 are excluded from the statistics.

Figures 5.20, 5.21 and 5.22 show the ARD values as a function of the gas absorption coefficients and the surface emissivities for the IPM and DT methods in the given cylindrical system. For the IPM method, even though the enclosure dimensions, the number of spatial divisions and the input temperatures for the rectangular system are very close to those of the present cylindrical case, the ARD values of the cylindrical case are 2–4% higher. This is due to the fact that in the cylindrical system the ratio of the number of imaginary planes to the number of real surfaces is 6.5, while in the rectangular case it is only 2.5. As seen in section 5.3.2, an increase in the number of imaginary planes increases the ARD, and consequently the accuracy deteriorates.

The accuracy of the DT method is similar for the cylindrical and for the rectangular cases as indicated by the ARD values.

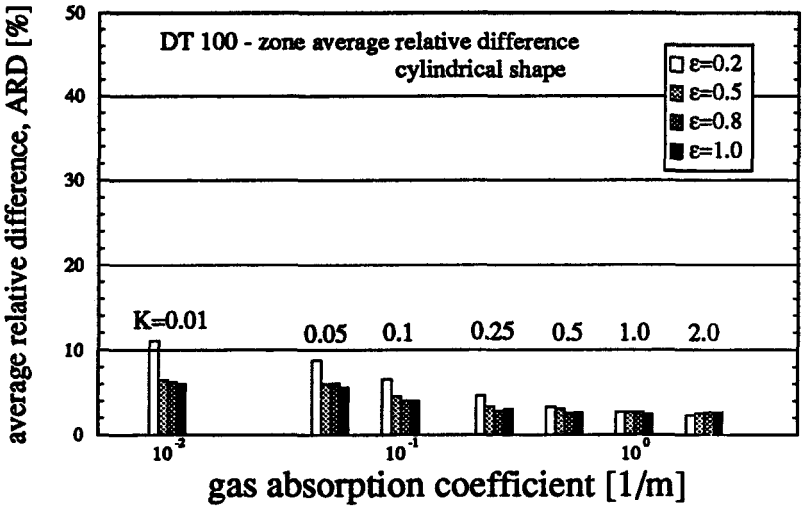

Figure 5.21 Average relative difference of surface heat flux between DT (100 solid angle divisions) and zone method with respect to surface emissivity and gas absorption coefficient for the cylindrical case. Heat fluxes lying in the interval [−5, 5] kW/m^2 are excluded from the statistics.

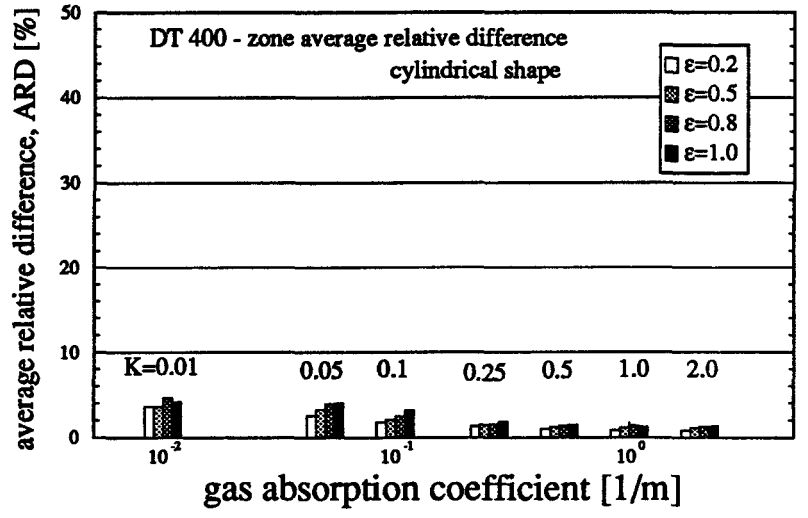

Figure 5.22 Average relative difference of surface heat flux between DT (400 solid angle divisions) and zone method with respect to surface emissivity and gas absorption coefficient for the cylindrical case. Heat fluxes lying in the interval [−5, 5] kW/m^2 are excluded from the statistics.

5.5 Additional remarks

At this point, it is worthwhile to emphasize some additional advantages of the IPM.

— The IPM is fitted with a restricted ray tracing algorithm since the rays are to be followed only in the individual zones. On the contrary, the DT and zone methods need a more sophisticated ray tracing technique, since the rays are tracked through the whole field. In this sense, in the absence of a good ray tracing technique, the IPM can be more easily adapted to complex problems (e.g. non-uniform gas absorption medium or irregular surface geometry) than the zone and the DT methods.

— In the case where some of the surface temperatures are not known (this was not the case in the preceding examples), the DT method needs two levels of iteration: one which is due to the intrinsic principle of the method (already explained in Section 2.3), the other which is related to the iterative solution of the heat balances at the walls for temperature calculation. This drawback of the DT method leads to a more complex procedure than that of the IPM where only one level of iteration is used for such problems.

It should be added that the zone sizing restrictions of the IPM do not impose too strong limitations in many practical cases. Provided the zoning is done correctly, this method can yield very good results for complex problems, as can be seen in examples 1 and 4 of the next chapter.

6

Examples of complex three dimensional cases

In this chapter the three radiation models are applied to stringent cases in order to prove the versatility and robustness of the methods. The problems are solved by the zone method for all cases in order to have a reference and with either the discrete transfer (DT) or the imaginary planes (IPM) method. The results are presented in three dimensions and graphical heat flux distributions are drawn at some selected places. For the 3D grids, in many cases the 2D curvilinear grid generating system of Wu (1990) was used, and the three dimensional representation of the results is due to the graphical interface of Brisson (1991). These tools were essential for the successful completion of the following examples.

6.1 Example 1: cylindrical remelting furnace

This example models a cylindrical aluminum remelting furnace. Figure 6.1 gives the schematic description of the furnace. The conic shape of the charge at the bottom of the furnace is approximated by a stepwise cylindrical pyramid, which is treated by the

blocking technique. A limited number of zones are used in the example, thus blocking provides only a rough approach to the conic shape.

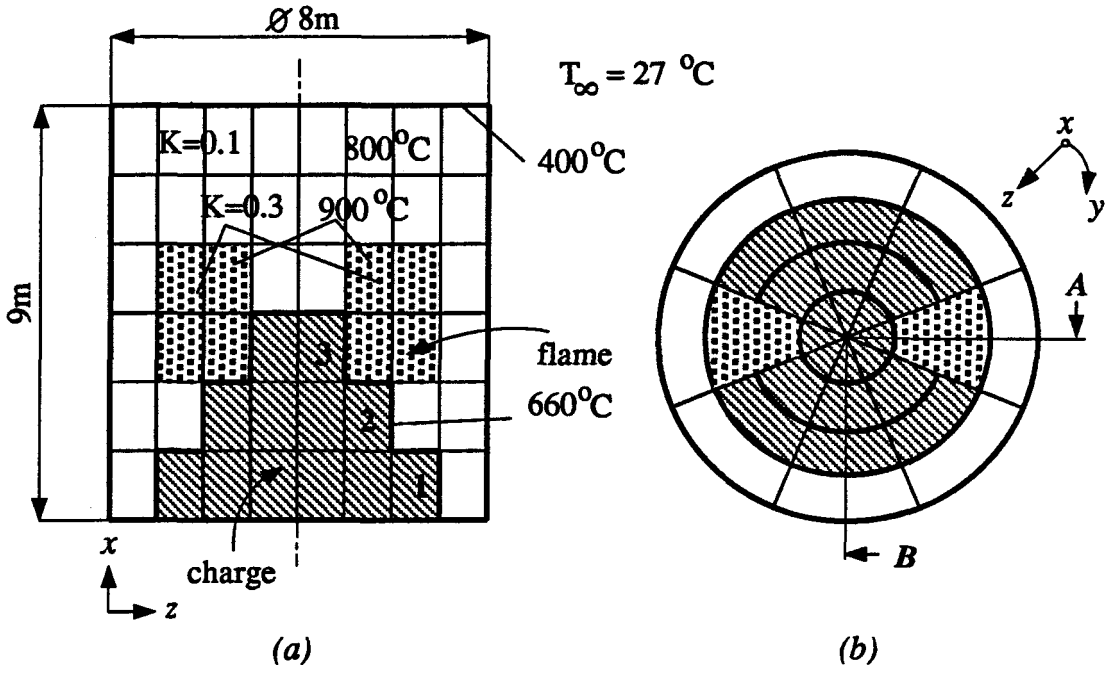

Figure 6.1 Description of the remelting furnace; (a) cross section, (b) top view

The radiative properties of the system are shown on Figure 6.1 and gathered in Table 6.1. The bulk gas temperature is set at 800 °C and two combustion zones are simulated by prescribing higher temperature and absorption coefficient at two locations. The charge is kept at the melting temperature of aluminium (933 K). All the temperatures are prescribed except that of the cylindrical wall of the enclosure which is calculated by the models used. Gas flow pattern is not needed since the gas temperatures are specified.

Table 6.1 Input data for example 1

Number of divisions		
x, y, z	6, 8, 4	
Temperatures		
circumferential surfaces	unknown	
top surface	673	K
bottom surface ,charge	933	K
gas	1073	K
flame	1173	K
ambiant	300	K
Wall emissivities		
top, circumferential surfaces	0.8	
bottom, charge	0.6	
Gas absorption coefficient		
gas	0.1	1/m
flame zone	0.3	1/m
Overall heat transfer coefficient		
top, bottom, circumferential surfaces	1.0	W/m^2K

The example has been solved by the IPM and by the zone methods. Due to the uniform cylindrical grid and only two different gas absorption coefficients, six different direct interchange areas are calculated for the IPM. Newton method is used in the iteration for the unknown temperatures of the circumferential surfaces in both the zone and the imaginary planes methods with analytically formulated Jacobian matrix.

Selected results are shown in Table 6.2, where the heat fluxes and the temperatures are presented for the horizontal and vertical faces of the pyramid steps in two radial sections *A* and *B*. The influence of the combustion regions appears clearly in the table: increased heat fluxes on the charge and increased temperatures at the wall in the vicinity of these regions.

Table 6.2 Results obtained with the IPM and zone method for the remelting furnace (h and v refer to horizontal and vertical zone respectively)

Zone	Temperatures on the cylindrical wall [°C]			
	sector A		sector B	
	IPM	zone	IPM	zone
top	721	703	718	701
.	752	744	747	735
.	780	778	766	752
.	779	780	766	752
.	747	748	742	741
bottom	687	718	685	716

Zone	Heat fluxes on the charge [kW/m^2]			
	sector A		sector B	
	IPM	zone	IPM	zone
3h	15.5	10.9	14.2	8.8
3v	19.6	20.1	12.7	11.6
2h	19.7	19.2	12.9	10.8
2v	12.6	13.1	11.0	10.9
1h	12.9	12.5	11.2	10.6
1v	8.8	8.7	8.5	8.8

Table 6.2 gives also a comparison between the zone method and the IPM. It is seen that the IPM is very accurate in this case, except for the heat flux at the top part of the charge (zone 3h). However, owing to the small area of this zone, the drawback of the discrepancy is minor.

6.2 Example 2: cylindrical remelting furnace with hemispherical dome

The configuration of the remelting furnace is now changed: the flat top becomes a hemispherical dome and the charge dumped on the base is modelled as a cone (which will become an octagonal regular pyramid in the curvilinear grid). The geometric arrangement and dimensions are shown on Figure 6.2. The data is somewhat artificial, however the main feature of the example is the combination of various geometrical elements (a cylinder, a cone and a hemisphere) within the same enclosure which illustrates clearly the flexibility of the technique developed in this thesis

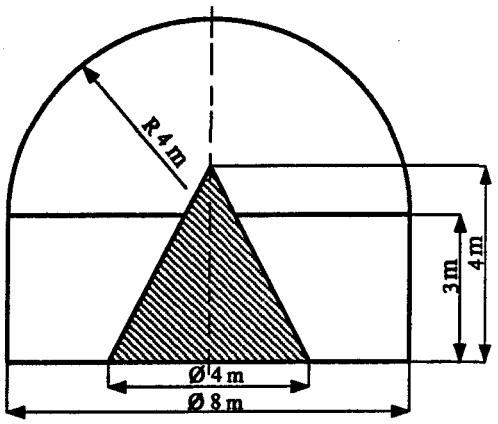

Figure 6.2 Cylindrical furnace with hemispheric dome and conic charge: geometrical arrangement

A curvilinear grid was inserted into one half of the cross-section of the radiation space. It was then rotated around the axis of the cylinder to scan the three dimensional volume, thus building the 3D grid. The 2D grid is shown on Figure 6.3. This grid would give a regular rectangular region in the curvilinear coordinate space. Index j is running horizontally from *1* to *5* and index k is running from *1* to *10*. The third index i is running around the perimeter from *1* to *8*.

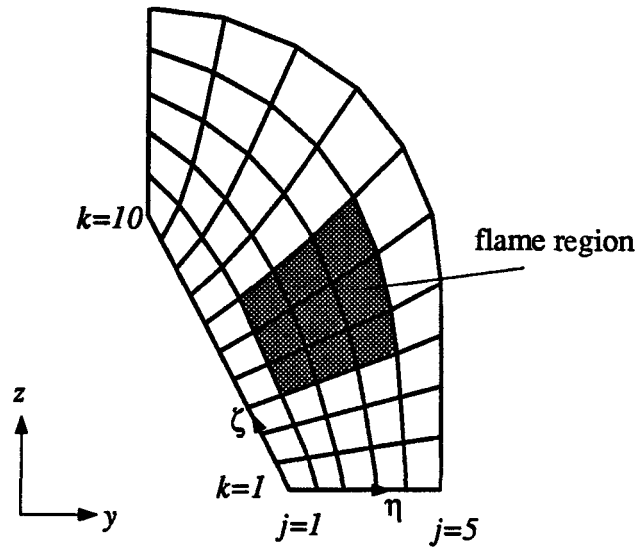

Figure 6.3 Two dimensional curvilinear grid used to generate the 3D grid

The physical conditions are listed in Table 6.3. The gas temperature is set to 1300 K, but four higher gas temperature regions are also created to represent the flames of four burners at *j=2–4, k=4–6* and at *i=1, 3, 5, 7* around the circumference.

Table 6.3 Input data for example 2

Number of divisions		
η, ζ, ξ	5 x 10 x 8	
Temperatures		
bottom, cone	500	K
cylinder, hemisphere	900	K
gas	1300	K
flame zone	1800	K
Wall emissivities		
bottom, cone	0.6	
cylinder, hemisphere	0.8	
Gas absorption coefficient		
gas	0.1	1/m
flame zone	0.5	1/m

The radiation heat fluxes were calculated by the zone and DT methods. The discrete transfer method used 400 solid angle divisions. The 3D representations of the heat fluxes on the surfaces obtained by the zone and DT methods are given on Figures 6.4 and 6.5. The 27 color shades of the color bar correspond to the heat fluxes on the surfaces. The pictures can be rotated around the coordinate axes and magnified for details. Moreover, the results of the two different methods can be displayed at the same time in two separate windows on the screen, which enables the comparison of the flux distributions. The red regions on the outside walls and the yellow regions on the conic charge represent the effect of the flame region.

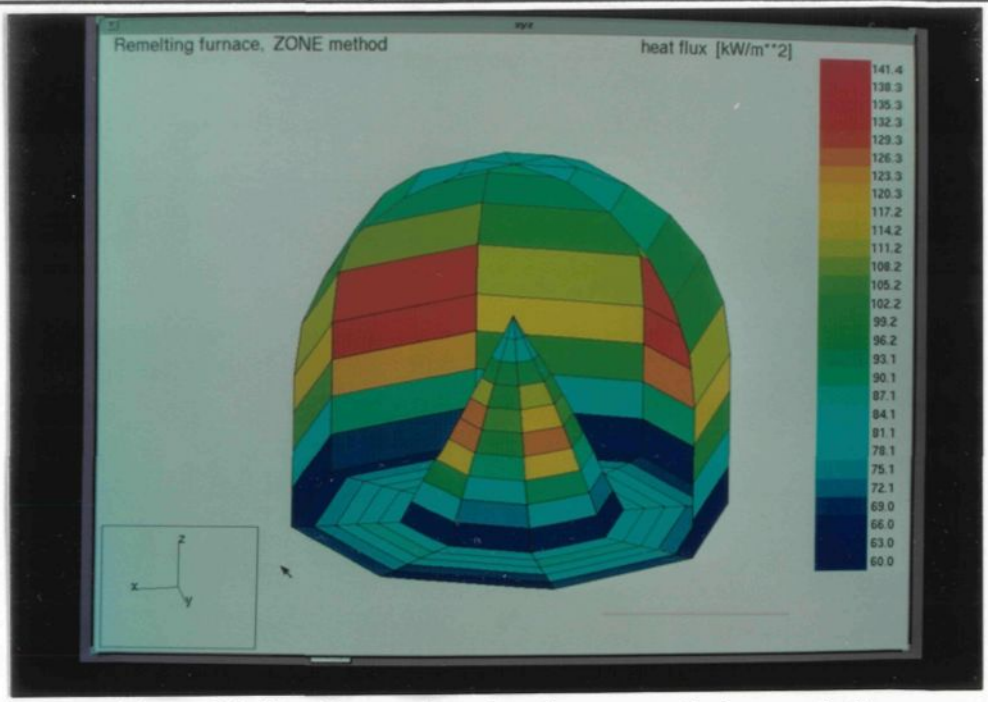

Figure 6.4 Heat flux results using the zone method, example 2

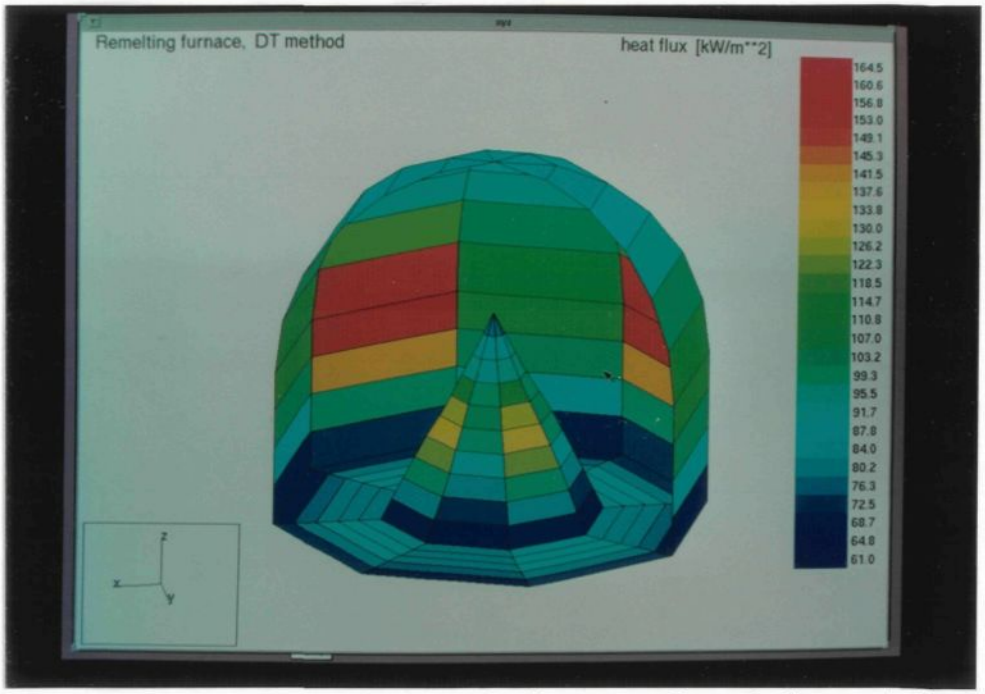

Figure 6.5 Heat flux results using the discrete transfer method, example 2

The resulting fluxes and volumetric radiative source terms of the DT method are compared to those of the zone method by forming the average and the maximum relative

differences as given by equations (5.1), (5.2) and (5.3). The results of the comparison and the CPU times are shown in Table 6.4.

Table 6.4 Comparison of the heat fluxes and the computation time, example 2

Average relative difference	divisions η, ζ, ξ 5x10x8	10x10x16	
fluxes on the surface zones (ARD)	3.3	1.9	%
volumetric sources in the gas zones (VRD)	37.9	15.2	%
Maximum relative difference (MRD)			
fluxes on the surface zones	18.8	9.9	%
volumetric sources in the gas zones	205.7	165.45	%
CPU time (SGI IRIS 4D/440)			
Zone method	3902	21700	s
DT method (400 div)	1305	2780	s

The discrete transfer method predicts the surface fluxes with a very good accuracy but the volumetric radiative source calculation is very inaccurate. The same example with prescribed uniform gas temperature field (i.e. omitting the high flame temperature regions) resulted in a VRD of 16% and a MRD of 80 % for the volumetric sources, which can still be considered to be rather inaccurate. The example was repeated with doubled circumferential and radial (η direction) divisions under the same physical conditions. The evaluation of the results is given in the rightmost column of Table 6.4. The results still show a considerable MRD for the radiative sources while the VRD decreased significantly. The volume source calculation needs improvement to avoid inaccuracies of this magnitude. It appears at first hand that Shah's approximation (discussed in Chapter 2) should be reconsidered when curvilinear coordinates are used with a relatively coarse grid.

The heat flux curves along the side of the cone are shown on Figure 6.6. The higher heat flux curve at $j=1$, $i=1$ refers to a position facing a hot gas (flame) region

while the lower flux curve at *j=1, i=2* corresponds to the section next to the previous curve location between two hot regions.

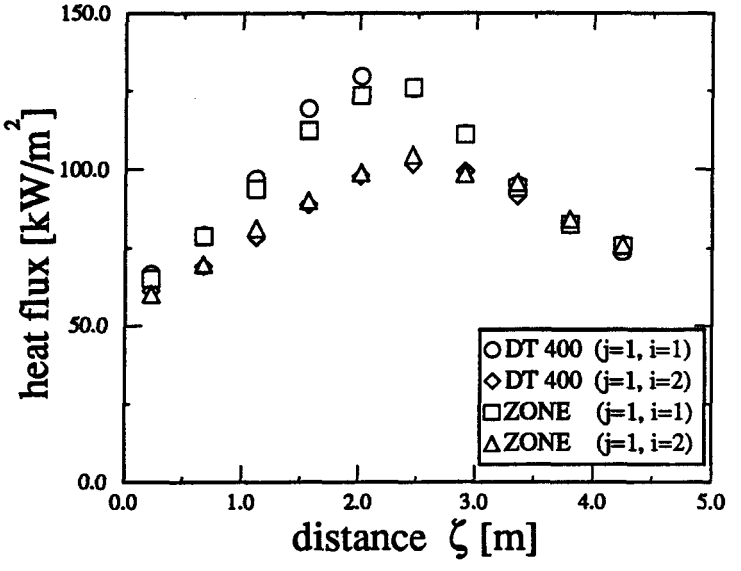

Figure 6.6 Heat flux curves along the side of the cone

6.3 Example 3: cylinders in a rectangular parallelepiped

Two cylinders are placed on the symmetry axis of a rectangular parallelepiped. The positions and dimensions of this configuration are shown on Figure 6.7. The difficulty of this example lies in the combination of a rectangular and a cylindrical shape.

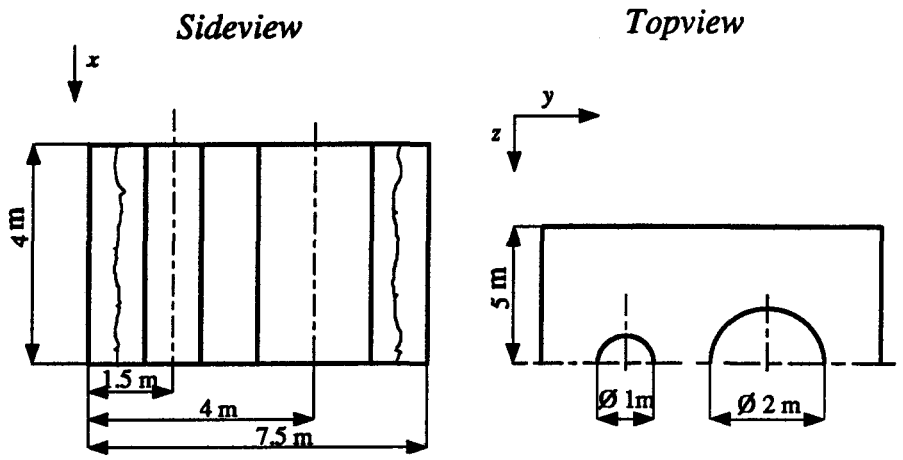

Figure 6.7 Two cylinders in a rectangular parallelepiped: geometrical configuration

A 2D curvilinear grid (Figure 6.8) was generated in the y, z plane, and then moved with equal increments in the x coordinate direction to generate the 3D grid.

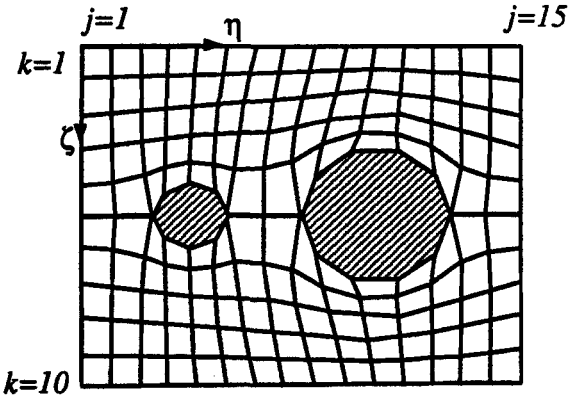

Figure 6.8 The 2D curvilinear grid of example 3

The temperatures, radiative properties as well as the divisions are specified in Table 6.5.

The problem was solved by the zone and by the discrete transfer methods. Only 100 solid angle divisions were used with the DT method but it is sufficient due to the homogeneous distribution of the zones.

Table 6.5 Input data for example 2

Number of divisions		
ξ, η, ζ direction	8 x 15 x 10	
Temperatures		
paralellepiped	573	K
cylinders	773	K
gas	1273	K
Wall emissivities		
paralellepiped	0.5	
cylinders	0.8	
Gas absorption coefficient		
gas	0.1	1/m

The 3D post-processing of the results are displayed on Figures 6.9 and 6.10. The effect of the cylinders is well detectable on the side and on the bottom of the parallelepiped in the case of both methods.

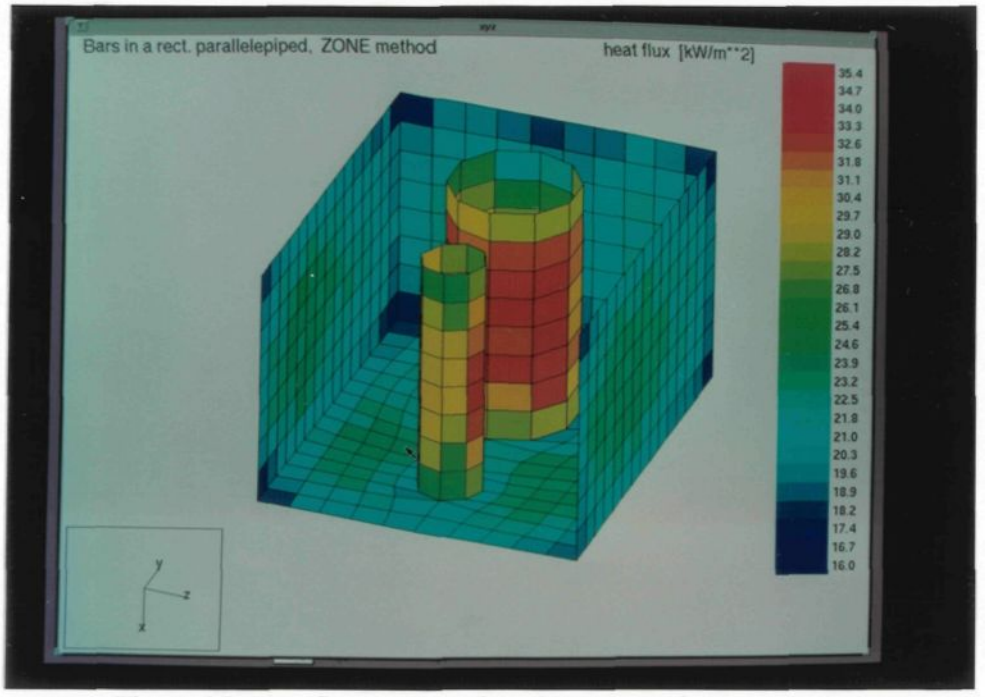

Figure 6.9 Heat flux results using the zone method. Example 3

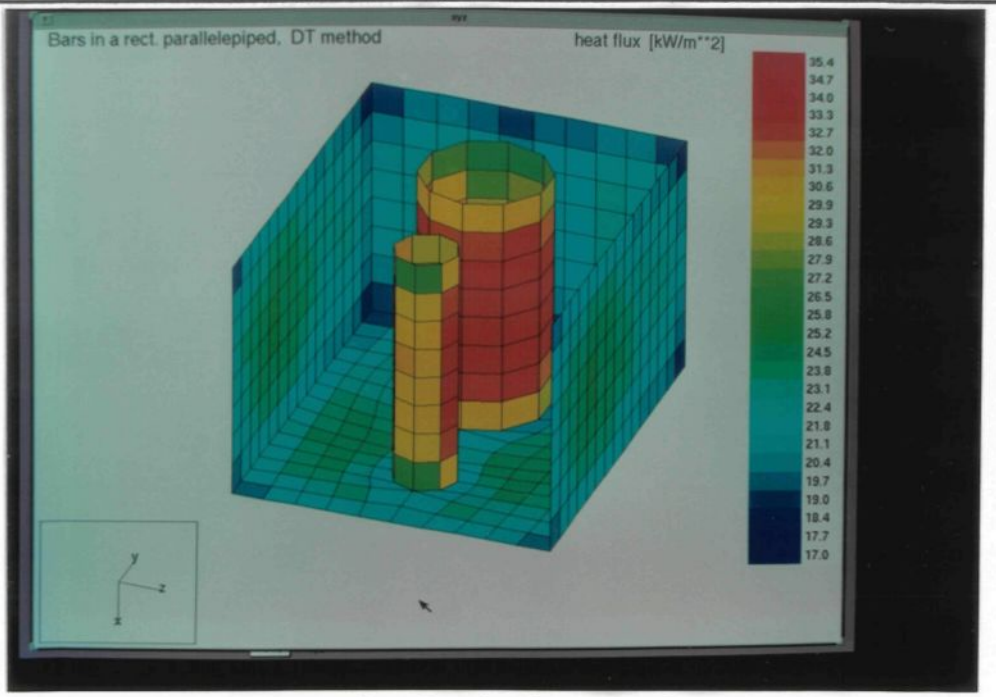

Figure 6.10 Heat flux results using the discrete transfer method. Example 3

The statistical comparison of the zone and the DT results is tabulated in Table 6.6. Equations (5.1), (5.2) and (5.3) were used to form the relative differences.

Table 6.6 Comparison of the heat fluxes and the computation time, example 3

Average relative difference		
fluxes on the surface zones (ARD)	4.4	%
volumetric sources in the gas zones (VRD)	3.2	%
Maximum relative difference (MRD)		
fluxes on the surface zones	15.5	%
volumetric sources in the gas zones	15.6	%
CPU time (IRIS 4D/440)		
Zone method	30969	s
DT method (100 div)	1270	s

The relative difference values are very low for both the fluxes and the volumetric sources although less solid angle divisions have been used than in example 2, where the gas source calculation with the DT method was very inaccurate. In this example, the temperature and radiative property distribution of the gas field were uniform and the grid

was finer, which resulted in accurate volume source computation. Similar experience with the DT method is reported by Guilbert (1989).

The heat flux curves along the symmetry line next to the cylinders on the bottom surface at $k=5$ and halfway between the symmetry line and the wall at $k=3$ are presented on Figure 6.11.

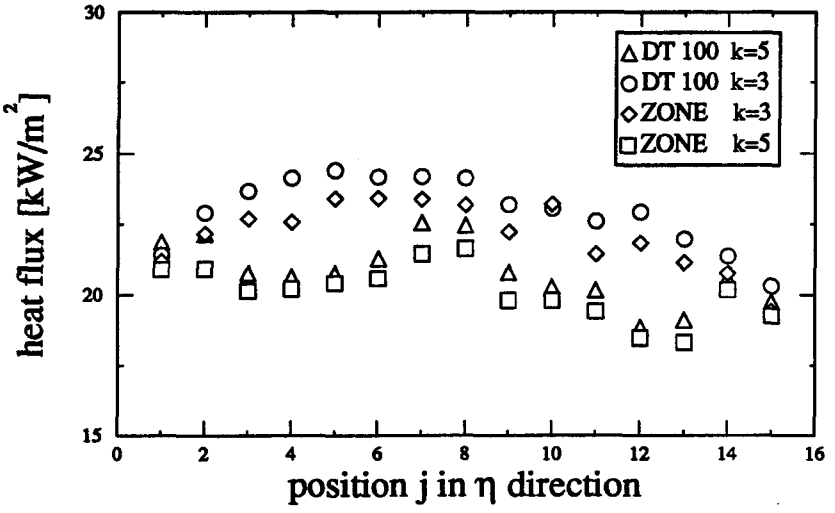

Figure 6.11 Heat fluxes on the bottom plate of the parallelepiped

6.4 Example 4: rotary kiln

This example represents a geometrical configuration which can be encountered in rotary kilns used in many industries. The difficulty of the example lies in the combination of the cylindrical circumferential wall and the planar bottom surface. The geometry could be well approached by using a cylindrical coordinate system and blocking the zones lying underneath the bottom surface. In this case, for a realistic geometrical approximation, high number of radial and circumferential divisions would have to be used which would practically exclude the use of the zone method. Instead, a curvilinear 2D grid (Figure

6.13) has been applied which was moved with equal increments along the length of the enclosure to generate the 3D grid.

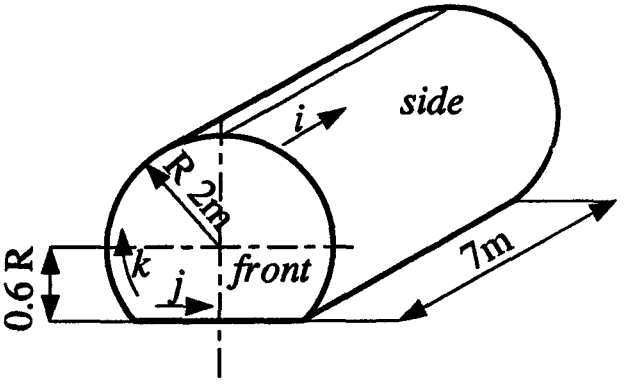

Figure 6.12 Geometrical configuration of a kiln shape enclosure

The temperatures of the front, end and circumferential surfaces are unknown and, beside radiation, conduction in the walls is also considered. The bottom and the gas temperatures are prescribed. In the gas, a flame zone is specified in a region defined by *j=3, 4, k=3...5* and *i=1....6*. The direction and the origin of the coordinates are shown on Figure 6.12. The example is solved by the IPM and the zone methods.

Table 6.7 Input data for example 4

Number of divisions		
ξ, η, ζ direction	6 x 6 x 8	
Temperatures		
front, end, circumferential surfaces	unknown	
bottom surface	873	K
gas	1273	K
flame zone	1473	K
ambiant	300	K
Wall emissivities		
front, end, side	0.8	
bottom	0.5	
Gas absorption coefficient		
gas	0.2	1/m
flame zone	0.5	1/m
Overall heat transfer coefficient		
front, end, circumferential surfaces	5.0	W/m^2K

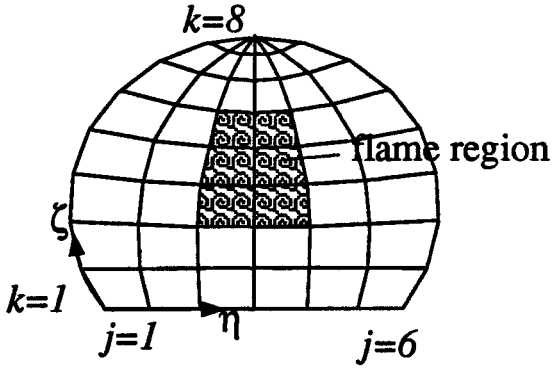

Figure 6.13 Two dimensional curvilinear grid used to generate the 3D mesh for example 4

The temperature distributions on the surfaces obtained by the zone method and by the IPM are shown on Figures 6.14 and 6.15 respectively. The statistical effect caused by computing the exchange areas with the Monte Carlo technique is clearly seen on Figure 6.14.

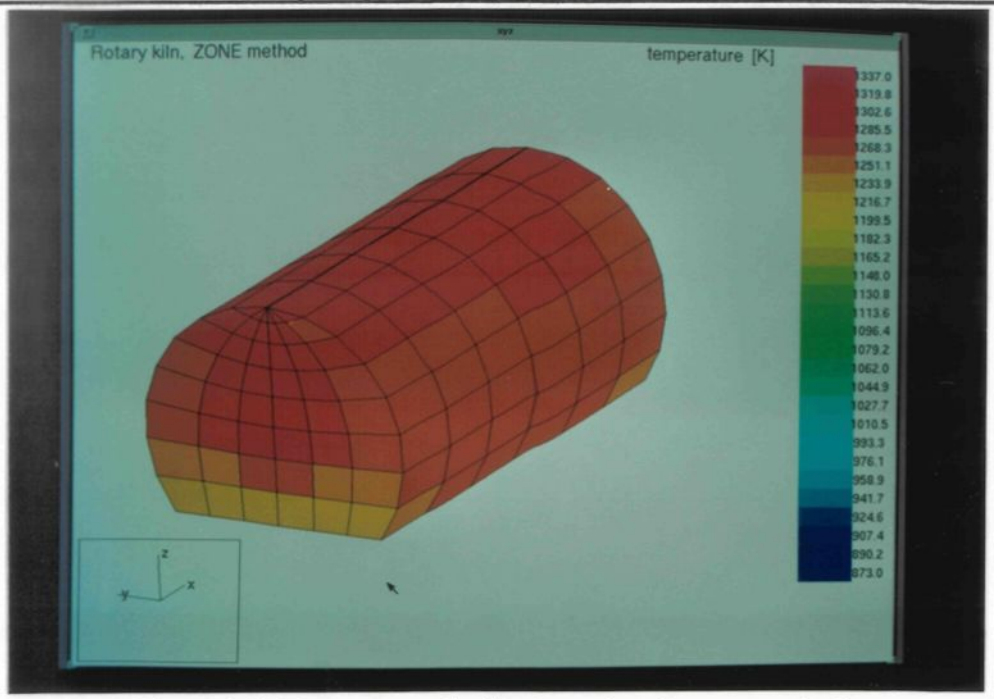

Figure 6.14 Temperature distribution using the zone method

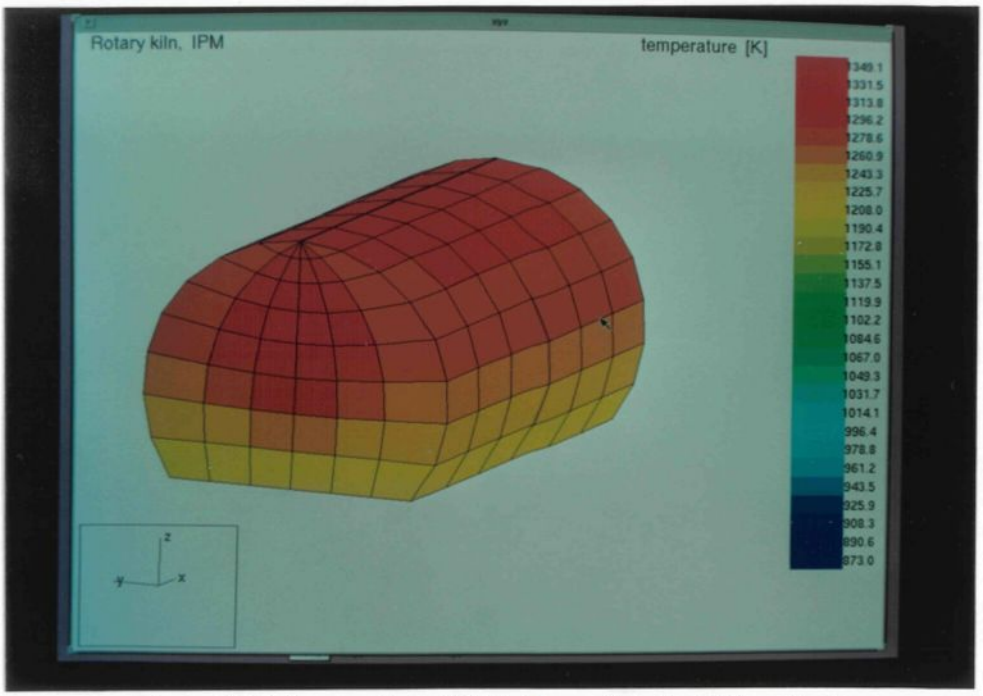

Figure 6.15 Temperature distribution using the IPM method

The temperature distribution on the surfaces of the kiln are plotted at two selected sections. One section is located on the side of the cylinder at $i=2$ spanning from the bottom up to the symmetry line along the ζ curvilinear coordinate from $k=1$ to 8 (Figure

6.16), the other is located on the front (or rear because of symmetry) face at *k=3* in the η curvilinear coordinate direction (Figure 6.17).

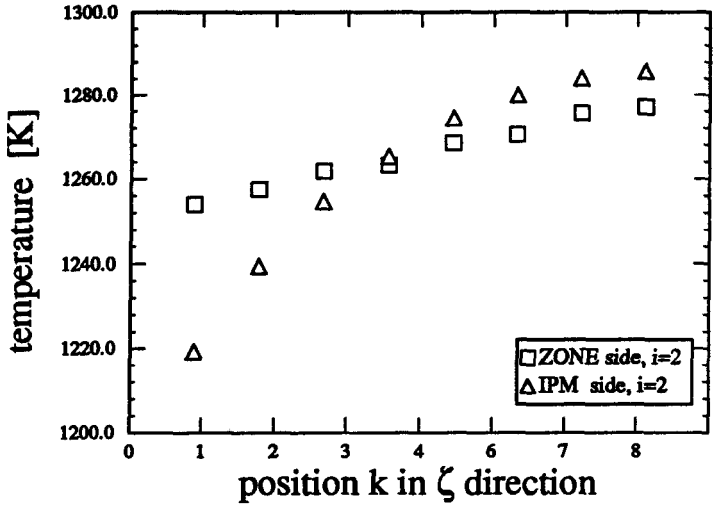

Figure 6.16 Temperature distribution on the circumferential side of the kiln, at i=2

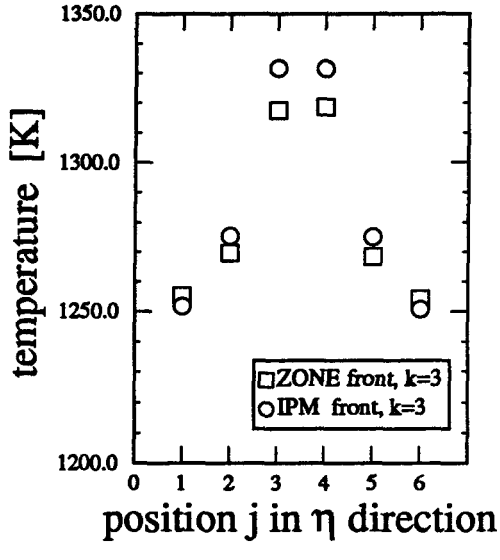

Figure 6.17 Temperature distribution on the front of the kiln, at k=3

The results are compared based on the average and maximum differences (ARD, VRD, MRD) for the surface heat fluxes, the volumetric sources in the gas zones and also the calculated temperatures. The surface heat fluxes and temperatures show small difference values, but in the case of the volumetric sources, the MRD and VRD values are very high.

Table 6.8 Accuracy and speed of calculation of the zone and the IPM methods for the kiln example

Average relative difference [%]	
fluxes on the surface zones (ARD)	1.2
temperatures on the surface zones (ARD)	0.9
volumetric sources in the gas zones* (VRD)	61.9
Maximum relative difference MRD [%]	
fluxes on the surface zones	5.3
temperatures on the surface zones	3.2
volumetric sources in the gas zones*	164.9
CPU time (IRIS 4D/440)	
Zone method	3346 [s]
IPM	900 [s]

*The heat fluxes of absolute value smaller than 5 kW/m^2 were not included in the statistics

The IPM was less efficient in the kiln example computation, than it was for the computation of the rectangular and cylindrical test cases. The zones do not have a uniform shape because of the application of curvilinear coordinates. The direct interchange areas had to be calculated for 48 zones due to differences is shapes. The iteration for the unknown temperatures was carried out by the Newton method for both the zone and the imaginary planes method. The Jacobian matrix necessary for the Newton method was formulated analytically for both methods.

7

Conclusion

This work is basically divided into two parts: the assessment of the imaginary planes and discrete transfer methods in rectangular and cylindrical coordinates, and the application and comparison of the three methods (the imaginary planes, the discrete transfer and the zone methods) in the case of selected complex enclosures.

As for the first part, the imaginary planes and the discrete transfer methods have been compared with the zone method in a rectangular parallelepiped and a cylinder for accuracy and computational performance. Comparisons were made for surface heat flux and volumetric radiative source terms. Surface emissivity and gas absorption coefficient were varied. The gas medium was considered as gray. The IPM proved to be sensitive to surface emissivity and a loss of accuracy in the case of higher spatial divisions was observed; however, the computational time requirements were very low. The discrete transfer method was not very sensitive to radiant property variation, and the solutions were very close to those of the zone method when 100 solid angle divisions were used; however, computational time requirements were 3 to 6 times higher than that of the IPM, especially in low-wall-emissivity cases due to its iterative procedure. This part of the work stressed the inherent weaknesses and the limitations of the IPM and the DT methods,

but, at the same time, fields for reliable application of these methods were shown to exist. This assessment study was made possible by the simultaneous development of a general purpose ray tracing technique which became an indispensable tool.

In the second part of the study, the three aforementioned methods were applied to more complex cases, and extension was made to curvilinear coordinates. The corner-stone of this part was still the fact that the ray tracing technique could be adapted to these more difficult problems. A major contribution of this work is that, above the fact that simplified methods proved to be adequate in many cases, the applicability of the zone method has been extended to cases that could not have been handled before. "Rigorous" results can now be obtained for a wide range of complex examples.

An immediate extension of the current work would be the incorporation of real gases. The assessment of the simplified methods relative to the zone method could be done for the same examples. More work should also be done to explain the large discrepancies obtained for the volumetric radiative source terms in examples 2 and 4 of chapter 6.

It would also be interesting to extend this work to semi-transparent media. The zone method for instance, with the Monte Carlo technique for calculating interchange areas, could be easily adapted to 3D radiation calculations in materials like glasses or systems such as packed beds, piles or fluidized beds. In a second step, simplified methods could then be tested by comparison to the reference solutions. Complex cases of mixed conduction/radiation or conduction/convection/radiation could eventually be studied.

Appendix A
Mathematical procedure related to the imaginary planes method

In the imaginary planes method a set of linear equations is solved to obtain the imaginary fluxes. The condensed form of these equations is reproduced from Chapter 2:

$$[BM]\{\mathbf{Q}\} = \{\mathbf{CM}\} \tag{A.1}$$

The dimension of the system is given by the number of imaginary fluxes crossing the imaginary planes. In a rectangular enclosure, having *nx, ny, nz* spatial divisions in the three coordinate directions, the dimension of the system is:

$$dim = 3 * nx * ny * nz + nx * ny + nx * nz + ny * nz \tag{A.2}$$

In a rectangular enclosure divided by 10 spatial divisions in every coordinate direction, the dimension of the set of equations is 3300, and the matrix **BM** has 10,890,000 elements, thus requiring a very large memory storage. As a consequence of the way the equations are formulated, the maximum number of non-zero elements in **BM** is 11 in each line. In the case of the above example, that means a maximum of 36300 non-zero elements. In general, the maximum number of non-zero elements can be given by: $11 * dim$.

With direct methods (for example the Gaussian elimination), the set of equations cannot be solved economically in the case of high spatial divisions, or the solution is hampered by excessive storage requirement.

The structure of **BM** is drawn on Figure A.1. The matrix is composed of 9 submatrices. The submatrices on both the upper and the lower side of the diagonal have

a 3 band storage pattern, resulting in a sparse matrix structure. The maximum width of the band in the main diagonal is 3, the other bands having a maximum of 2 elements.

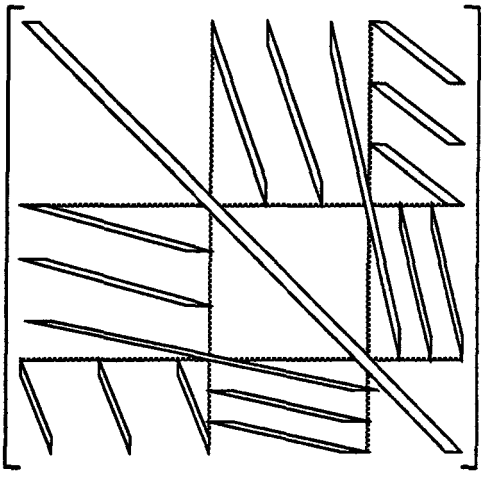

Figure A.1 The storage pattern of matrix BM

A data structure is described by Dahlquist et al. (1974) for the storage of large sparse systems. If A is a large sparse matrix, it can be stored by the means of three vectors AN, JA, IA. AN contains the non-zero elements row by row. The column number in A of the element AN(k) is given in JA(k), while IA(k) gives the position in vector AN of the first element of the ith row of A. The last element in IA is equal to the total number of elements in AN plus one. For example:

$$\mathbf{A} = \begin{bmatrix} 2 & 0 & 0 & 1 & 0 \\ 0 & 4 & 0 & 0 & 5 \\ 6 & 0 & 1 & 0 & 0 \\ 0 & 0 & 0 & 9 & 9 \\ 0 & 1 & 0 & 0 & 7 \end{bmatrix}$$

$$AN = (2,\ 1,\ 4,\ 5,\ 6,\ 1,\ 9,\ 9,\ 1,\ 7) \tag{A.3}$$

$$JA = (1,\ 4,\ 2,\ 5,\ 1,\ 3,\ 4,\ 5,\ 2,\ 5)$$

$$IA = (1,\ 3,\ 5,\ 7,\ 9,\ 11)$$

The number of memory storage places necessary to store the **BM** matrix using the above storage principle becomes:

$$11 * dim + 11 * dim + dim = 23 * dim \qquad \text{(A.4)}$$

The set of equations, with only the non-zero elements, can be solved using an iterative method. The Gauss-Seidel method works well in this case, but faster results can be obtained by the successive overrelaxation (SOR) method. The iterative solution is performing so well that it is worth to use it in the case of lower spatial distributions, where the direct methods are still applicable.

If the IPM is used with iteration on temperatures, a set of nonlinear equations is solved iteratively using the Newton method. Larouche (1989) explains how the Jacobian matrix of the Newton method can be constructed analytically to increase the speed of iteration. For the analytical formulation of the Jacobian matrix, $\mathbf{BM}^{-1}$ has to be supplied. The most important feature of the iterative solution is that **BM** matrix is not formulated, therefore the Jacobian matrix for the temperature iteration have to be computed numerically.

Appendix B
Assessment of the direct interchange areas obtained for cylindrical cases

Hottel (1967) gives the direct interchange areas (DIA) for a cylinder filled with gray gas, which has been subdivided with a cylindrical grid without using circumferential divisions (keeping full annular zones around the axis). The DIAs between the gas zones (g_i), the lateral wall zones (w_i) and the end wall zones (e_i) are computed with numerical integration and tabulated in terms of the optical thickness KB of the zone and of the relative spatial position between the zones.

The author has used these results to test his Monte Carlo calculations of the total interchange areas (TIA) in cylindrical systems. The emissivity was set to 1 in order to compare with Hottel's DIAs. The computation was done with 8 circumferential divisions and the DIAs so obtained were then summed to enable the comparison.

The geometrical configuration of the cylinder and the position of the zones for which the DIAs are provided are shown on Figure B.1. For the Monte Carlo simulation, B was taken as *1 m* and 10,000 rays were emitted from every zone. Table B.1 contains the DIA values for the configuration of Figure B.1.

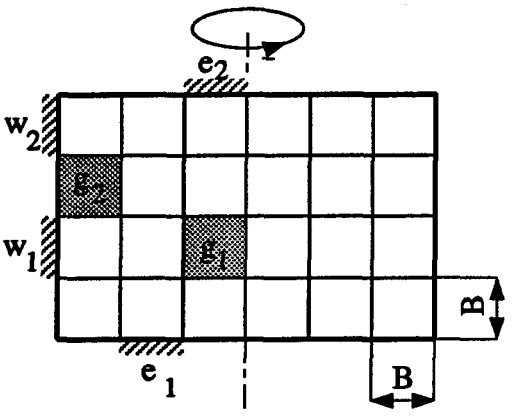

Figure B.1 Geometrical configuration of the cylindrical test case

Table B.1 Verification of Monte Carlo method for direct interchange area calculations (B=1m, 8 circumferential divisions, 10,000 rays emitted from every zone)

	KB			
	0.1	0.25	1.0	
$\overline{e_1 g_1}$	1.211E-1	2.246E-1	2.145E-1	Hottel
	1.238E-1	*2.362E-1*	*2.363E-1*	*Monte Carlo*
$\overline{e_1 e_2}$	2.786E-1	1.459E-1	5.831E-3	Hottel
	2.840E-1	*1.509E-1*	*6.26E-3*	*Monte Carlo*
$\overline{e_1 w_1}$	1.660E 0	1.102E 0	1.723E-1	Hottel
	1.644E 0	*1.091E 0*	*1.709E-1*	*Monte Carlo*
$\overline{w_1 g_1}$	1.588E-1	2.585E-1	1.304E-1	Hottel
	1.571E-1	*2.603E-1*	*1.237E-1*	*Monte Carlo*
$\overline{w_1 w_2}$	1.029E 0	4.913E-1	2.115E-2	Hottel
	1.018E 0	*4.931E-1*	*2.073E-2*	*Monte Carlo*
$\overline{w_1 e_1}$	1.660E 0	1.102E 0	1.723E-1	Hottel
	1.673E 0	*1.095E 0*	*1.746E-1*	*Monte Carlo*
$\overline{g_1 g_2}$	1.763E-2	7.556E-2	2.033E-1	Hottel
	1.800E-2	*7.175E-2*	*1.941E-1*	*Monte Carlo*
$\overline{g_1 w_1}$	1.588E-1	2.585E-1	1.304E-1	Hottel
	1.585E-1	*2.483E-1*	*1.184E-1*	*Monte Carlo*
$\overline{g_1 e_1}$	1.211E-1	2.246E-1	2.145E-1	Hottel
	1.119E-1	*2.195E-1*	*1.935E-1*	*Monte Carlo*

Appendix C
Assessment of the direct interchange areas for irregular shape

Let rectangles **A, B** and **C** be black surfaces positioned in the geometrical configuration given on Figure C.1. The rigorous values of the DIAs between rectangle **A** and **B** and between **A** and **C** can be obtained analytically with the formulas given by Siegel and Howell (1983); these will serve as references for comparison with the Monte Carlo calculation.

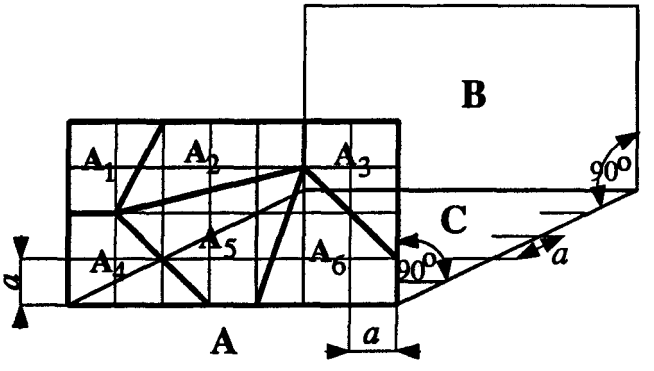

Figure C.1 Geometrical arrangement for DIA calculation test for irregular shapes

Surface **A** is then subdivided into six irregular surface elements, as shown, and the Monte Carlo technique for irregular shape is then applied (see section 3.4.4, uniformly distributed emission points). For reference a regular grid is superimposed on surface **A** and its spacing is set to 1 m. The DIAs are calculated between each tetragon and surfaces

B and C, and then summed to give the desired values:

$$\overline{s_A s_B} = \sum_{i=1}^{6} \overline{s_{A_i} s_B}$$
$$\overline{s_A s_C} = \sum_{i=1}^{6} \overline{s_{A_i} s_C} \qquad \text{(C.1)}$$

The results are given in the following table:

Table C.1 Comparison of DIAs between A, B and A, C obtained analytically and by the Monte Carlo technique for tetragonal shapes

	Analytically (Siegel & Howell)	Numerically Monte Carlo
$\overline{s_A s_C}$	7.08256	7.08549
$\overline{s_A s_B}$	5.82336	5.78720

It is seen that the values are very close to each other. On the other hand, in section 3.4.5 a simplified method for emission point determination is proposed for the Monte Carlo technique in irregular zones. Due to the simplification, the uniform distribution of the emission points is not fulfilled, the effect of which is studied in Table C.2:

Table C.2 Comparison of DIAs obtained for the irregular surfaces A_i using uniform and non-uniform emission point distribution

	Emission point distribution	
	Uniform	Non-uniform
$\overline{s_{A_1} s_B}$	*0.5529*	0.5485
$\overline{s_{A_2} s_B}$	*1.1189*	1.0833
$\overline{s_{A_3} s_B}$	*0.7192*	0.7480
$\overline{s_{A_4} s_B}$	*0.7299*	0.7586
$\overline{s_{A_5} s_B}$	*1.5435*	1.5199
$\overline{s_{A_6} s_B}$	*1.1227*	1.0697

	Emission point distribution	
	Uniform	Non-uniform
$\overline{s_{A_1} s_C}$	*0.9603*	0.9260
$\overline{s_{A_2} s_C}$	*1.9538*	2.0166
$\overline{s_{A_3} s_C}$	*1.2191*	1.3207
$\overline{s_{A_4} s_C}$	*0.5646*	0.5827
$\overline{s_{A_5} s_C}$	*1.4243*	1.3617
$\overline{s_{A_6} s_C}$	*0.9632*	0.8607

The errors introduced by the simplified emission point calculation are in the range of *2–9 %*. Considering that the Monte Carlo introduces a statistical error, it is recommended to use the uniform emission point generation for highly irregular shapes (i.e. for shapes far from rectangles) to avoid the accumulation of errors. The ratio of calculation time with the uniform emission point generation compared to the non-uniform is *1.2* to *1.4*.

Bibliography

Bhattacharjee, S., and Grosshandler, W. A simplified model for radiative source term in combustion flows. *Int. J. Heat Mass Transfer 33*, 3 (1990), 507–516.

Brisson, S. Construction of an user interface for the Riedhammer furnace model. Tech. Rep. 21, Groupe de Recherche en Ingénierie des Procédés et Systèmes, UQAC, 1990.

Cannon, P. The calculation of radiative heat flux in furnace enclosures using the Monte Carlo method. Master's thesis, The University of New Brunswick, Chemical Engineering Department, 1967.

Charette, A., Larouche, A., and Kocaefe, Y. Application of the imaginary planes method to three-dimensional systems. *Int. J. Heat Mass Transfer 33*, 12 (1990), 2671–2681.

Dahlquist, G., and Björck, A. *Numerical methods*. Prentice-Hall, 1974.

De Marco, A., and Lockwood, F. A new flux method for the calculation of radiation in furnaces. *La Rivista dei Combustibili 29* (1975), 184–196.

Erchiqui, F. Modélisation mathématique d'une chambre de combustion par la méthode des plans imaginaires. Master's thesis, Dépt. des Sciences Appliquées, Université du Québec à Chicoutimi, 1987.

Fiveland, W. Three-dimensional radiative heat transfer solutions by the discrete ordinate method. In *Proc. 24–th National Heat Transfer Conference and Exhibition, Pittsburgh* (1987).

Guilbert, P. Comparaison of Monte Carlo and discrete transfer methods for modelling thermal radiation. In *9–th Members Conference of the International Flame Research Foundation at Noordwijkerhout, The Netherlands* (1989).

Harrington, S. *Computer Graphics, A programming approach*, second ed. McGraw-Hill Book Company, 1987.

Hottel, H. C., and Sarofim, A. F. *Radiative transfer*. McGraw-Hill Book Company, 1967.

Kobiyama, M. Reduction of computing time and improvement of convergence stability of the Monte Carlo method applied to radiative heat transfer with variable properties. *Transactions of the ASME, J. of Heat Transfer 111* (1989), 135–140.

Kumar, S., Majumdar, A., and Tien, C. The differential-discrete ordinate method for the solutions of the equations of radiative transfer. *Transactions of the ASME, J. of Heat Transfer 112* (1990), 424–429.

Larouche, A. Couplage de la méthode des plans imaginaires en trois dimensions et du logiciel PHOENICS pour la modélisation de la chambre de combustion de fours industriels. Master's thesis, Dépt. des Sciences Appliquées, Université du Québec à Chicoutimi, 1988.

Raithby, G., and Chui, E. A finite volume method for predicting a radiant heat transfer with participating media. *Transactions of the ASME, J. of Heat Transfer 112* (1989), 415–423.

Shah, N. *The computation of radiation heat transfer*. PhD thesis, Dept. of Mech. Eng., Imperial College of Science and Technology, London, 1979.

Siegel, R., and Howell, J. *Thermal radiation heat transfer*, second ed. Mc-Graw Hill, 1983.

Ström, B. A simple heat transfer model for furnaces based on the zoning method. *Wärme und Stoffübertragung 13* (1980), 47–52.

Strommer, G. *Geometria.* Tankönyvkiadó, Budapest, 1988.

Thompson, J., Warsi, Z. U. A., and Mastin, C. W. *Numerical grid generation, Foundations and applications.* North-Holland, 1985.

Watt, A. *Fundamentals of three-dimensional computer graphics.* Addison-Wesley, 1989.

Wu, Y. *Numerical studies of melting process in a cylindrical enclosure.* PhD thesis, Dépt. de Génie Méchanique, École Polytechnique de Montréal, 1990.